Title:

Blasting Effects on Coal Refuse Impoundment Structures

OSM Cooperative Agreement Number:

S12AC20021

Type of Report:

FINAL REPORT

Reporting Period Start Date:

09/01/2012

Reporting Period End Date:

12/31/2016

Principal Authors:

Dr. Jhon Silva
Paul Sainato
Dr. Braden Lusk
Kenneth Eltschlager

Date Report Issued:

July 2017

Address:

University of Kentucky
Mining and Minerals Resources Building, Lexington, KY
859-257-1105 (office)
859-323-1962 (fax)

Disclaimer

Table of Contents

Figures

Tables

Abstract

Mining water impacts are a concern of the public, government regulators, and the coal mining industry. After the Buffalo Creek disaster in 1972, government regulators began promulgating guidance on coal slurry impoundment design by the Mine Safety and Health Administration (MSHA), updated in 2009 to include dynamic seismic stability analysis due to concerns of potential failures induced by earthquakes. However, dynamic analysis and stability guidance regarding blasting operations near an impoundment were not considered. There is little information on the effect of blasting on embankments, particularly coal slurry impoundment embankments. In recent years research in blasting effects on embankments have been studied but have been limited to the study of sand. Only recently, the interest has turned to defining the dynamic properties of fine coal mine tailings material but, as yet, the impact of blasting vibration on this material has not been conclusively studied.

Detailed study of the impact of blasting vibrations on coal slurry impoundments must be performed regarding the effect of the blasting vibration waveform on areas susceptible, if at all, to failure triggered by vibrations produced by blasting. Analysis of the difference between the energy and frequency characteristics of a blast versus an earthquake through the calculations and modeling in this research will give a novel evaluation of the cyclic stress ratio and duration of cycles produced by a blast and its effect on impoundment material. Access to the study site was initially restricted due to a bankruptcy and later due to some miscommunications between the new owners of the site and the University of Kentucky. Access was allowed for three days but the data collected was inconclusive. Consequently, the analysis offered here not allow determination of limits on blasting near impoundments. Although the following conclusions and recommendations are suggested:

- Continue to use the 2.0 inches per second limit published by the Bureau of Reclamation until further research is accomplished.
- Monitoring efforts should be located on the side of the impoundment in original ground nearest to the proposed blasting due to attenuation effects in the impoundment.
- Future research efforts should be geared toward determining the effect of duration and frequency on the fines in the impoundment by vibrations produced by blasting.
- Future research is needed to define the stress hardening dynamic characteristic of coal fines.
- Downstream and upstream failure should be considered in the dynamic analysis of coal impoundments subjected to blast vibrations. Upstream failure is most likely to occurs because of the saturation condition of the material at this side of the impoundment.

List of Graphical Materials

N/A

1. Introduction

Currently, mining water impacts (streams, creeks, etc.) are very sensitive topics for the mining industry, the public, and the government agencies. Due to the topographic conditions in the Appalachian area, impoundments or disposal facilities are developed close to streams or in valleys, using different configurations; side hill and the cross valley is shown in Figures 1 and 2 below (Engineering and Design Manual. Coal Refuse Disposal Facilities 2009).

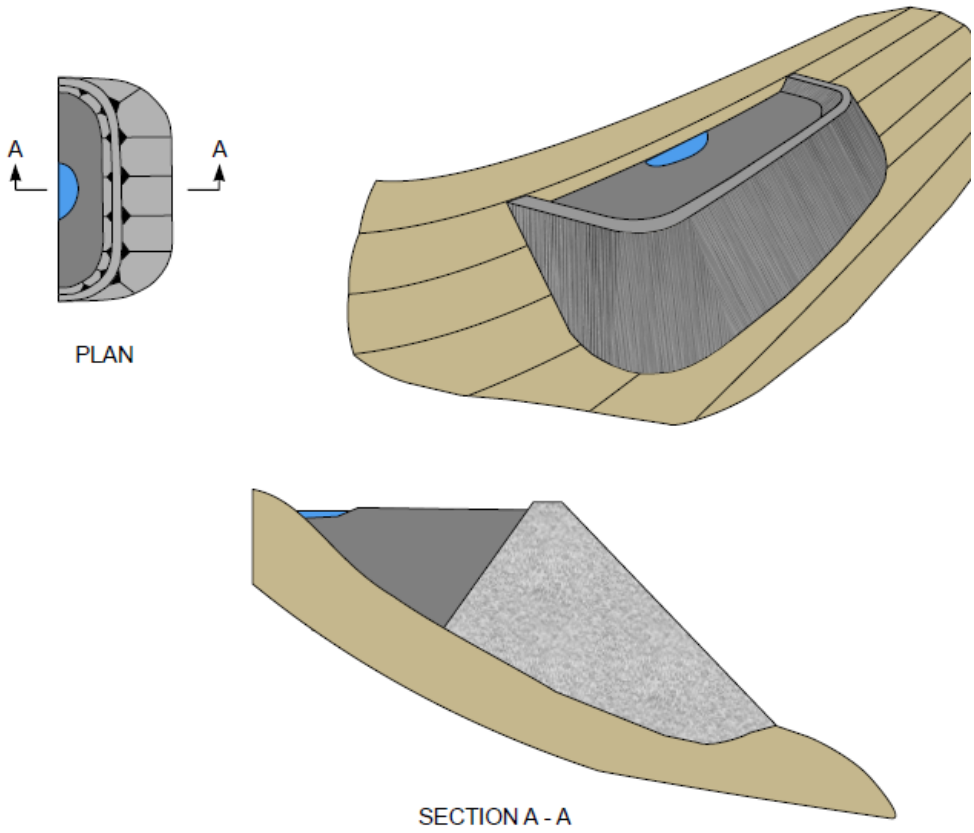

Figure 1 *Side-hill Impounding Embankment (Engineering and Design Manual. Coal Refuse Disposal Facilities 2009)*

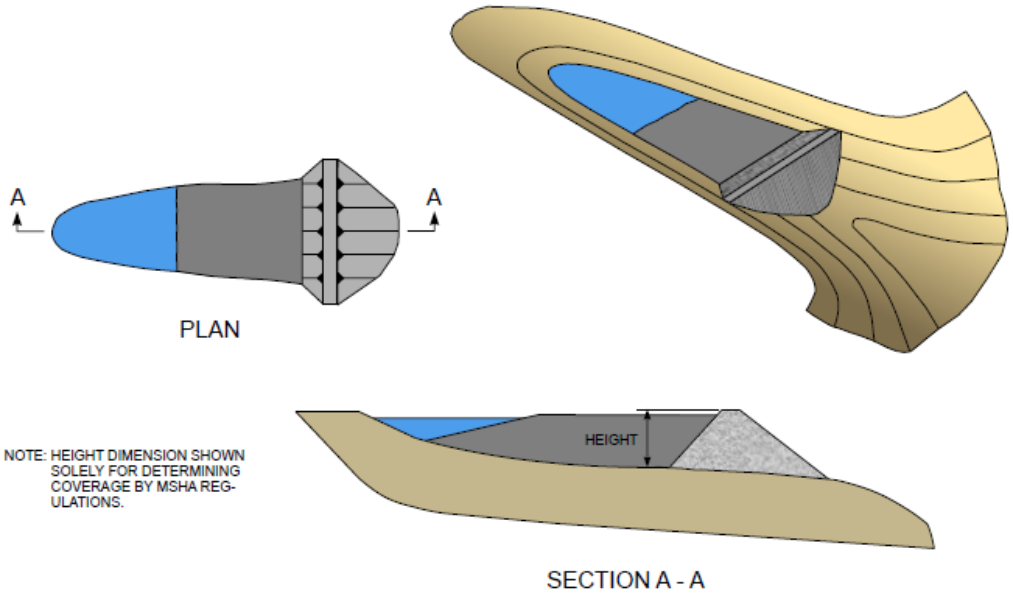

Figure 2 *Cross Valley Impounding Embankment (Engineering and Design Manual. Coal Refuse Disposal Facilities 2009)*

Cross Valley embankment facilities are the most common and are constructed by using one of three staging methods, upstream, centerline, or downstream staging methods shown in Figures 3 through 5 below (Engineering and Design Manual. Coal Refuse Disposal Facilities 2009).

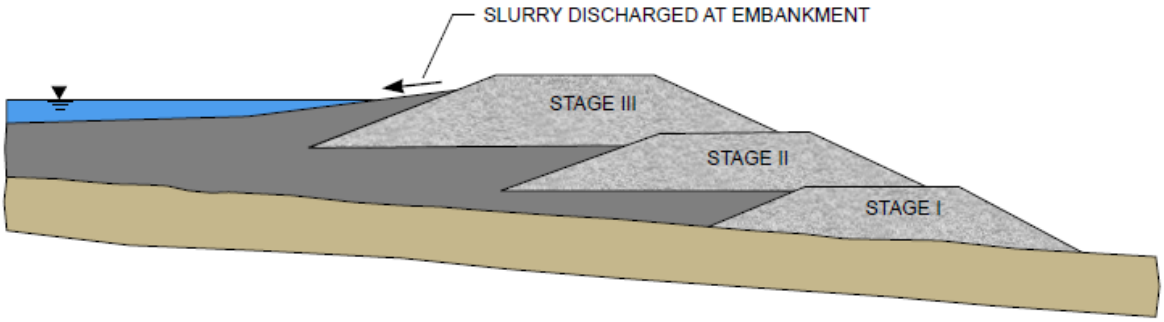

Figure 3 *Upstream Staging Method (Engineering and Design Manual. Coal Refuse Disposal Facilities 2009)*

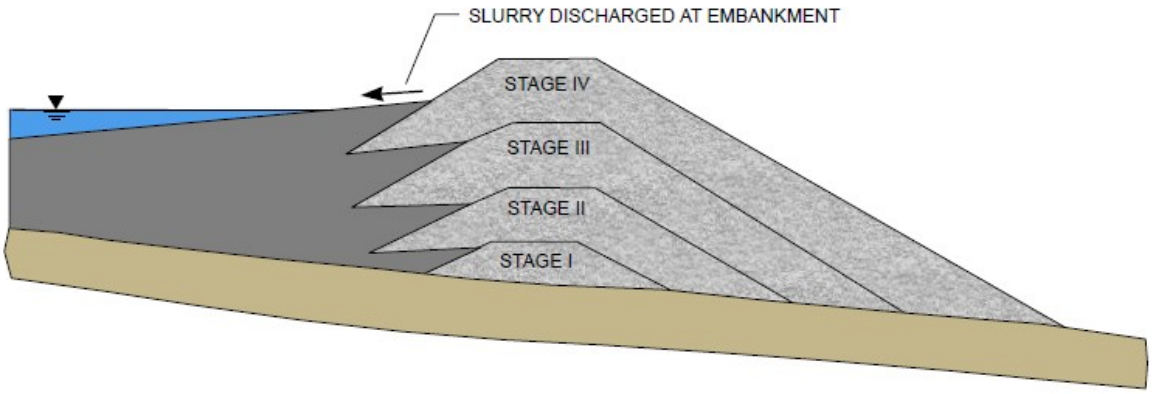

Figure 4 *Centerline Staging Method (Engineering and Design Manual. Coal Refuse Disposal Facilities 2009)*

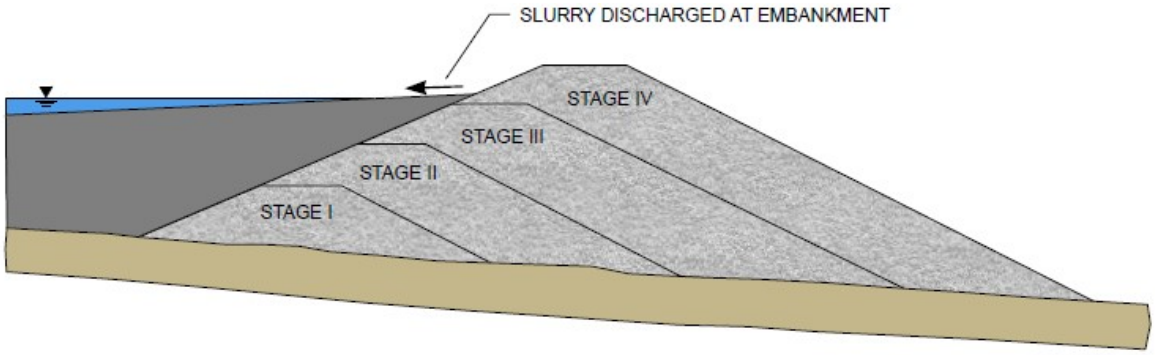

Figure 5 *Downstream Staging Method (Engineering and Design Manual. Coal Refuse Disposal Facilities 2009)*

An impoundment slope failure can be catastrophic involving human lives as well as environmental losses. Since 1972, after the Buffalo Creek failure, several regulations were promulgated to avoid new disasters. Currently, in the stage of impoundment design, it is recommended to evaluate the seismic instability of the impoundments under dynamic conditions as a consequence of earthquake motion. This evaluation assumes that the main source of ground motion that will impact the impoundment is generated by an earthquake source. There are few or no references to evaluate the stability when ground motions are generated by blasting activity. The hypothesis that blasting does not generate enough vibration levels to affect the impoundment facilities must be tested, and the question about the influence of blasting activity in this type of facility remains.

The main point of this project is to determine if near or adjacent blasting affects the stability of coal refuse impoundments and, if so, produce guidelines for blasting in the form of nomograms with upper bounds and lower bounds of charge weight and distance. To

economically gauge the blasting effects, a computer model will be generated. The model will be calibrated to data from an actual impoundment. The goal is to install instrumentation into an impoundment that has blasting occurring near or adjacent and collect particle velocity and acceleration data and pore pressure data that may be used to calibrate the model.

2. Literature Review

2.1 Impoundment Design Standards

As result of the processing activity of coal from underground or surface coal mining, there are two materials as sub products from processing that currently have low economic interest and are necessary for disposal. Those materials are classified as Coarse Coal Refuse (CCR) and Fine Coal Refuse (FCR) (Y.A. Hegazy, A.G. Cushing, & C.J. Lewis., 2004). These materials are disposed of close to the processing areas using the CCR as the body of the embankment, containing or supporting, and in some cases supported by, the FCR material.

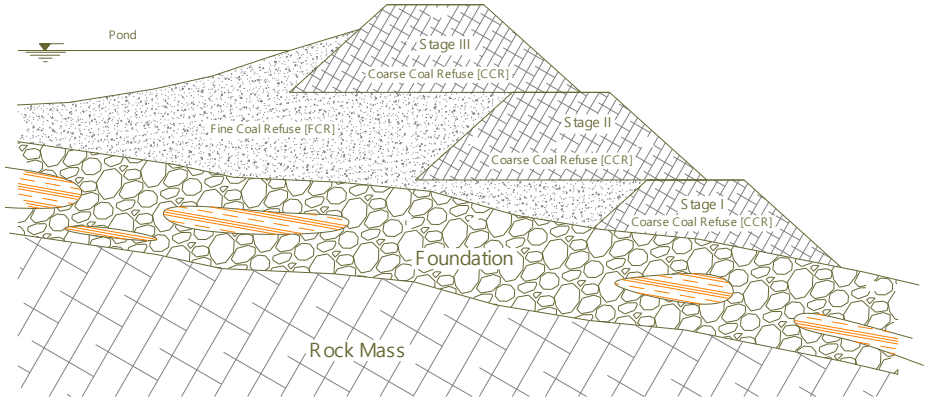

Figure 6 *Coal refuse schematic cross section*

FCR materials in its initial consolidation process behave like slurries and are often hydraulically placed in the impoundment. The composition of CCR and FCR materials is related to many factors among them: the genesis of the coal deposit, mining technique used, mineral processing methodology used and environmental and economic factors.

Before the 1972 Buffalo Creek failure, technical specification regarding slope stability for planning design and operation of coal refuse impoundments in the U.S. were minimal. Following the Buffalo Creek failure, several regulations and guidelines controlling the planning, design and operation stages of these facilities had been promulgated. In 1975,

the Engineering and Design Manual for Coal Refuse Facilities was published as a design and planning guide. In 2009, the manual was updated to reflect many improvements, and positive results from coal refuse impoundment research and experience since 1975.

As a result, geotechnical engineering principles, hydraulics considerations, dam safety guidelines and other technical considerations are now a major part of estimates for the design of disposal facilities included in the mining feasibility studies. Technical considerations include impoundment design considering seismic events, even though failures of coal disposal facilities due to seismic activity have not been reported in the U.S. (Engineering and Design Manual. Coal Refuse Disposal Facilities 2009).

Due to the high variability in the composition of the impoundments, studies have focused on the determination of the geotechnical properties of CCR and FCR materials. Some studies characterizing the geotechnical properties of coal refuse materials, including those developed in the Appalachian region, are; (Almes and Butail., 1976), (Chen C.Y 1976), (Busch et al 1974), (Saxena eta al 1984) and (Y.A. Hegazy, A.G. Cushing, & C.J. Lewis., 2000). The geotechnical parameters found by these researchers are useful for slope stability analysis of impoundments under static conditions.

However, what about design under dynamic conditions? General guidelines to analyze the impoundments under dynamic conditions are included in the 2009 Manual. Those guidelines are adapted from embankments, and dam facilities other than coal refuse disposal facilities and include specifically an earthquake as the main generator of the dynamic conditions. It is clear that a ground motion due to a blast when compared to a quake have different characteristics such as; frequency content of the movement, amplitude, duration, and energy released. These characteristics in both events are different, so it is intuitive to expect different responses under those two different dynamic scenarios. Therefore, it is necessary to research the behavior of the impoundments specifically under dynamic conditions due to mine blasting.

Recently, much work has been published and is ongoing concerning the geotechnical characterization of dynamic properties of coal refuse disposal impoundment materials; (Ulrich et al. 1991), (Castro 2003), (Genes et al. 2000), (Kalinski and Phillips 2008) and recently (Zeng and Gobe 2008). The Kalinski and Phillips project at the University of Kentucky was completed by a doctoral student who published his dissertation in 2013

(Salehien 2013). The results of these projects are the characterization of the dynamic properties of the materials using field and laboratory tests from undisturbed and disturbed samples of coal refuse. The parameters measured were; undrained shear strength, damping ratio, pore pressure changes and other parameters used to evaluate the behavior of coal refuse under dynamic conditions.

Seismic design of embankments and dams is a complex task that involves elaborate mathematical models, engineering judgment, educated assumptions and many iterative steps to achieve a satisfactory design. The first step in the process is the seismic hazard analysis. The seismic hazard analysis comprises the identification and evaluation of the earthquake sources. Two approaches are normally used deterministic and probabilistic approaches. As a result, the main characteristic of the design ground motion is determined, giving the level of shaking that the impoundment needs to withstand. Usually, the design ground motion is determined for the bedrock under the target site. Once the design ground motion is established, the next step is to develop a ground response analysis. The ground response analysis is the evaluation of the response of the soil and structures (natural or manmade) above the bedrock to ground motion wave propagation from the bed-rock up to the surface. This analysis is performed to predict ground surface motions and to evaluate the dynamic stresses and strains in the soil mass as a result of the passing seismic waves. The influence of soils on earthquake damage has been recognized for years, and this analysis allows prediction ground surface motions and the development of design response spectra, and evaluation of liquefaction hazards, strength loss of the materials, and the dynamic forces induced by the motion in the earth-structures (impoundments) or other structures supported by the soil. (Kramer 1996) There are two methods to perform the ground response analysis: equivalent analysis and nonlinear analysis using one, two or three-dimensional formulation depending on the problem under consideration.

2.2 Dam Failure Under Load

The main causes of impoundment or dam failures under dynamic loading are:

- Failure occurs during the ground motion in saturated materials when a reduction in the shear strength of the material causes the failure. The reduction in the shear strength is due to the increment in the pore pressure as a consequence of the dynamic load.

- Failure occurs during the ground motion, through the generation of incremental driving forces that cause the failure due to the dynamic load acting in the body of the impoundment. There is not a reduction in the strength of the materials.
- Failure occurs after the ground motion when a reduction in the shear strength of the material is presented, and the static gravity driven forces produce the failure.

Despite the absence of reported failures of coal refuse impoundments due to dynamic activity (earthquakes or blasting) within the U.S. coal fields, several cases have been reported worldwide in which blast-induced liquefaction and the subsequent slope failure of dams have occurred (Thomas E., Bretz 1990). The majority of the documented blast-induced dam's failures correspond to military research where the destructive capacity of explosives and missiles were tested. Very few or no destructive research has been conducted for mining impoundment structures. Some of the most well-known blasting-induced liquefaction events are:

- Calaveras Dam, California (1918) – Failure during construction. A flow failure occurred during construction using hydraulic placement of dam materials. The materials were still consolidating and weak. Blasting was not cited as the cause but was mentioned at the site. (Bretz, 1990, Regents, 2015)

- Pacific Atolls (the 1950's) – Not a dam failure at all but reports of liquefaction after a 15,000 kiloton above-ground nuclear blast cratering study. Liquefaction was evident in the crater as well as sand boils as far away as 4,265 feet. (Bretz, 1990)

- Pre-Dice Throw, New Mexico (1975) – These two events were crater tests where 100 tons of high explosives were detonated above ground. The surface consisted of 6.6 feet of dry to moist, silty clay over saturated clays, sands, and silts. The resulting craters were flat, and water springs flowed for several hours. (Bretz, 1990)

- Hayman Igloo test, Utah (1988) – In testing explosions in a weapons structure, 440,925 pounds of TNT equivalent high explosives were detonated. The resulting crater was 393.7 feet in diameter with a great deal of water in it after the test; the original water table was at a depth of 16.4-19.7 feet. One of the surrounding structures was swallowed and ended up 2 feet below the level of the apparent crater. (Bretz, 1990)

Despite all available information regarding liquefaction events, an explosion as a product of military applications has different characteristics than an explosion due to mining

applications, and it is necessary to research the dynamic response of impoundments subjects to mining blasting activity. In most cases for the military tests, explosives were embedded within or on top of the structure, or a nuclear explosion occurred. Mine blasts are adjacent to the structures, are not as energetic as a nuclear blast, and thus will not induce the type of cratering or effects expected in military tests. To analyze the effects of blasting on coal refuse impoundments, the study of slope stability under dynamic conditions is necessary.

The behavior of slopes subjected to dynamic loads can be grouped according to the behavior of the material under dynamic conditions (Kramer 1996). There are two categories based on the behavior of the materials under dynamic conditions:

- inertial stabilities or non-brittle or non-liquefiable behavior
- weakening instabilities, strength loss, brittle or liquefiable behavior

For each category, different analyses are performed to evaluate the safety factor and deformation characteristics of the slopes. On the other hand, several methods to evaluate the behavior of the materials under dynamic conditions in a slope are proposed, they are:

- Straightforward methods based on information about the material's properties collected during field testing; Standard Penetration test (SPT), Cone Penetration Test (CPT) and properties measured in lab test; particle size and Atterberg-limit data.

- Sophisticated methods based on pore-pressure measurements developed by Seed and updated by Youd et al. (2001). Strain–based methods developed by Castro (1994) and stress-based methods developed by Olson and Stark (2003). (Engineering and Design Manual. Coal Refuse Disposal Facilities 2009).

Two possible outputs are obtained after straightforward or sophisticated methods; strength loss or non-strength loss during and after the dynamic forces. If the analysis concludes that the material does not exhibit strength loss during or after the ground motion, a deformation analysis is performed. On the other hand, if analysis results show that the dynamic forces trigger strength loss, in other words, if there is a liquefaction potential or weakening instabilities due to the vibrations, seismic stability analyses are required (Engineering and Design Manual. Coal Refuse Disposal Facilities 2009).

To perform deformation analysis, pseudo-static, sliding block and stress-deformation methods can be used. The Makdisi-Seed approach, based on results of sliding block analysis,

is frequently used. Based on the results of the deformation analysis, tailing impoundments are classified in a range from susceptible to catastrophe if significant crest settlement occurs due to the deformation triggered by the dynamic forces (Harvey N., McLeod Steve Rice., and Michael P. Davies (1992)).

Additionally, pseudo-static analyses represent the effect of an earthquake by applying static horizontal and/or vertical accelerations to a potentially unstable mass of soil. The inertial forces induced by these pseudo-static accelerations, increase the driving forces and may decrease the resisting forces acting on the soil. The stability, in this case, is expressed regarding a pseudo-static factor of safety calculated by limit equilibrium procedures (Harvey N., McLeod Steve Rice., and Michael P. Davies (1992)).

Finally, the Makdisi-Seed procedure is based on sliding block analysis of earth dams. This procedure involves other factors, the fundamental period of vibration of the embankment and the yield acceleration of the slope under analysis. Figure 7 below shows the variation of average maximum acceleration with the depth of potential failure surface for dams and embankments under dynamic earthquake conditions (Makdisi and Seed 1978).

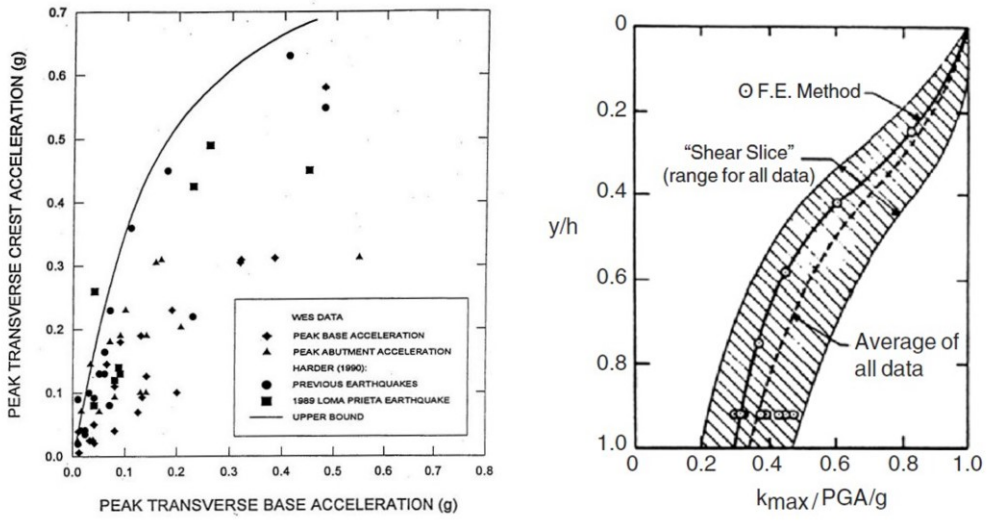

Figure 7 *Nomograms to estimate dam and embankment earthquake-induced deformations. After Makdisi and Seed (1978)*

Seismic stability analyses are functions of the level of strength loss due to the dynamic forces. The type of instability depends on the tendency in the reduction of the strength referenced to the stress required to maintain static equilibrium. If the reduced strength is greater than the stress required to maintain static equilibrium, the slope will present

deformation failures. On the other hand, if the reduced strength is lower than the stress required to maintain static equilibrium, the slope will exhibit flow failures.

To perform seismic stability analyses, there are four analytical procedures (Harvey N. McLeod, Steve Rice and Michael P. Davies., 1992).

- Residual strength analyses
- Modified Pseudo-Static Analyses
- Total stress equivalent linear dynamic analyses
- Effective stress finite-element analyses

To provide an understanding of the steps and analysis required for seismic stability analysis, design manual procedures must be discussed.

2.3 Seismic Stability Analysis

2.3.1 General Discussion

Seismic instability potentially occurs when the overall average post-event shear strength is less than the pre-event shear strength (Engineering and Design Manual. Coal Refuse Disposal Facilities 2009). When seismic instability is present in one or more zones of the impoundment, failure, if it happens, is driven by static gravitational forces (weight of the impoundment zone) (Engineering and Design Manual. Coal Refuse Disposal Facilities 2009). For seismic instability to occur, three conditions must be satisfied (Engineering and Design Manual. Coal Refuse Disposal Facilities 2009):

1. The event shaking must be strong enough to trigger undrained strength loss.
2. The post-event strengths must be less than the static driving shear stresses.
3. The amount of material experiencing strength loss must be sufficient to cause instability.

Given these conditions, seismic stability analysis has three components (Engineering and Design Manual. Coal Refuse Disposal Facilities 2009):

1. Perform a triggering analysis (evaluate whether the event is strong enough to cause strength loss).
2. Evaluate post-event strengths in the various soil zones that may be susceptible to strength loss.

3. Perform static, limit-equilibrium, slope-stability analyses using post-event strengths for the materials in the embankment and foundation.

2.3.1.1 Triggering Analysis

If a sand-like material is saturated, small shear strains (less than or equal to 1%) can trigger sudden decrease from undrained peak strength (*Sup*) to undrained steady-state (residual) strength (*Sus)* (Engineering and Design Manual. Coal Refuse Disposal Facilities 2009). For saturated clay-like material, higher shear strains (5% or greater) are usually needed to cause some strength loss, and very high shear strains are needed to cause strength loss to *Sus* (Engineering and Design Manual. Coal Refuse Disposal Facilities 2009). However, highly sensitive clays may behave like sand-like materials and exhibit strength loss at low strains (Engineering and Design Manual. Coal Refuse Disposal Facilities 2009). There are three general approaches to triggering analysis (Engineering and Design Manual. Coal Refuse Disposal Facilities 2009):

- Pore-pressure-based approach – Uses a method developed for evaluating whether event shaking will generate high excess pore pressure in sand-like materials. This approach is not applicable to clay-like materials.

- Strain-based approach – For clay-like material, this approach considers post-event strength as a function of shear strain that occurs. For sand-like material, this approach assumes that strength loss is triggered when the cyclic shear strain induced by the earthquake exceeds a critical value (i.e., the triggering shear strain).

- Stress-based approach – This approach assumes that strength loss is triggered when shear stresses exceed the undrained yield strength (the peak undrained strength). This approach is not applicable to clay-like materials.

For loose saturated sand-like material, a moderate to large earthquake will almost always be large enough to trigger strength loss and triggering analysis should not be used to confirm the design of an embankment if the peak ground acceleration (PGA) at the base of the embankment is higher than 0.2g, and the cyclic stress ratio (CSR) in this material is greater than 0.15 (Engineering and Design Manual. Coal Refuse Disposal Facilities 2009). In this case, assume the triggering of strength loss a post-event strength at *Sus* (Engineering and Design Manual. Coal Refuse Disposal Facilities 2009). For sites with PGA > 0.2g and CSR > 0.15, a triggering analysis may be beneficial to assess alternative stabilization

schemes to reduce the CSR within recommended guidelines (Engineering and Design Manual. Coal Refuse Disposal Facilities 2009).

2.3.1.2 Evaluation of Post-Event Strength

The undrained, steady state strength, *Sus,* is mostly a function of void ratio and is very sensitive to changes in void ratio (Engineering and Design Manual. Coal Refuse Disposal Facilities 2009). The void ratio in sand-like materials is a function of the method of deposition and material deposited by water such as fine coal refuse can have significant variations in void ratio even within a uniformly deposited zone such that samples from different areas within the zone will have different values of *Sus.* (Engineering and Design Manual. Coal Refuse Disposal Facilities 2009). Thus, the method of evaluating *Sus* must account for the variability within zones and between layers (Engineering and Design Manual. Coal Refuse Disposal Facilities 2009).

However, in clay-like materials, the void ratio is mostly a function of the consolidation pressure and stress history, and *Sup* and *Sus* are less sensitive to the void ratio (Engineering and Design Manual. Coal Refuse Disposal Facilities 2009). Thus, the post-event strength is likely to be more uniform within a particular zone or layer (Engineering and Design Manual. Coal Refuse Disposal Facilities 2009).

Three approaches to evaluate post-event strength of materials susceptible to strength loss are discussed in the guidelines (Engineering and Design Manual. Coal Refuse Disposal Facilities 2009):

1. Empirical correlations of standard penetration test (SPT) and/or cone penetration test (CPT) values with back-figured, post-event strengths from flow slides may be used to estimate *Sus* for sand-like material (assuming strength loss with the resultant post-event strength of *Sus*).

2. Laboratory tests on high-quality samples from the field can be used to estimate post-event strengths for both clay-like and sand-like material.

3. Field vane-shear tests and CPTs can be used to measure *Sus* for clay-like material. Remember that S*us* is often a conservative low estimate of the actual post-earthquake strength for clay-like material.

The scope of this research is to determine if blasting has an effect on coal refuse impoundments and the main concern is liquefaction in the fine coal refuse underlying the coarse refuse material forming the embankment. As such, an analysis of whether or not the

vibration from a blast will trigger strength loss is primary and pore-pressure based methods are targeted. There are two options to perform the stability analysis: downstream and upstream. For stability analysis, both directions are important, however, if it is considered that upstream direction the materials will have higher saturation compared to downstream, in a dynamic event upstream direction could become more critical than downstream direction.

2.3.2 Pore-Pressure-Based Method for Triggering of Strength Loss in Clay-Like Material

It is accepted that highly plastic clays (excepting highly sensitive clays) are not susceptible to significant pore pressure buildup (Engineering and Design Manual. Coal Refuse Disposal Facilities 2009).

Screening of susceptibility of clay-like materials to strength loss based on CPT data can be performed using the figure below (Engineering and Design Manual. Coal Refuse Disposal Facilities 2009):

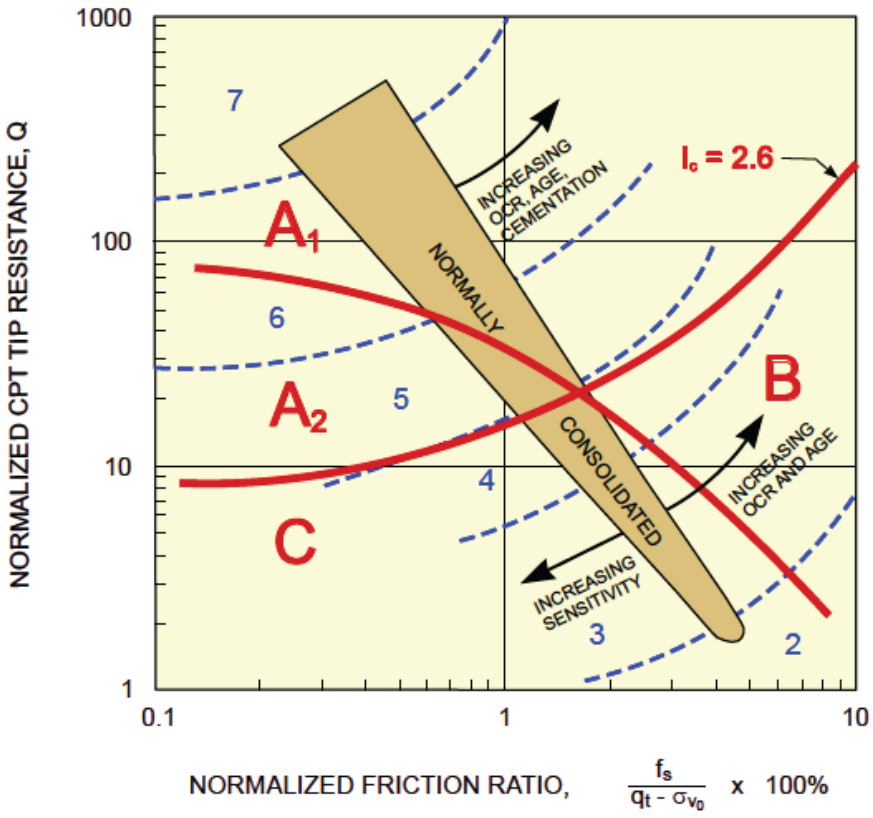

NOTE:
1. VALUES OF Q AND F ARE COMPUTED FROM CPT DATA AT THE DEPTHS OF INTEREST, AS DESCRIBED IN YOUD ET AL. (2001).
2. CPT DATA THAT PLOT IN ZONES A_1 AND A_2 INDICATE MATERIAL THAT IS NOT CONSIDERED CLAY-LIKE, SO THIS SCREENING METHOD IS NOT APPLICABLE.
3. CPT DATA THAT PLOT IN ZONE B INDICATE CLAY-LIKE MATERIAL THAT IS NOT SUSCEPTIBLE TO STRENGTH LOSS.
4. CPT DATA THAT PLOT IN ZONE C INDICATE CLAY-LIKE MATERIAL THAT MAY BE SUSCEPTIBLE TO STRENGTH LOSS.
5. NUMBERED ZONES SEPARATED BY DASHED BLUE LINES ARE FOR REFERENCE ONLY AND ARE A GUIDE TO SOIL TYPES, AS DESCRIBED IN YOUD ET AL. (2001). FOR EXAMPLE, DATA IN ZONE 3 INDICATE SILTY CLAY TO CLAY WHILE DATA IN ZONE 6 INDICATE CLEAN SAND TO SILTY SAND. THE LINE SEPARATING SAND-LIKE FROM CLAY-LIKE MATERIAL CORRESPONDS TO A SOIL BEHAVIOR TYPE INDEX (I_c) OF 2.6, AS ALSO DESCRIBED IN YOUD ET AL. (2001).

Figure 8 Use of CPT Data to Screen Clay-Like Material *(Engineering and Design Manual. Coal Refuse Disposal Facilities 2009)*

If CPT data is unavailable, SPT data can be used if the material is confirmed clay-like using the SPT data and Atterberg limits. An N > 6 corresponds to Zone B and N < 6 corresponds to Zone C with the SPT N-values corrected for hammer efficiency but not for overburden pressure (Engineering and Design Manual. Coal Refuse Disposal Facilities 2009).

2.3.3 Pore-Pressure-Based Method for Triggering of Strength Loss in Sand-Like Material

As discussed above, this method should not be used, and triggering should be assumed, if the PGA is greater than 0.2g and the CSR is greater than 0.15 with the resultant

post-event strength at *Sus,* unless assessing alternative stability schemes (Engineering and Design Manual. Coal Refuse Disposal Facilities 2009).

The steps of the method are as follows (Engineering and Design Manual. Coal Refuse Disposal Facilities 2009):

1. For the location at which each value of either SPT $N_{1,60}$ or CPT q_{t1N} was obtained in zones of material that may be susceptible to strength loss, compute CSR, which is the average cyclic shear stress caused by the design event in the zone of material divided by the initial effective vertical stress in the zone of material (τ_{av} /σ'_{vo}). Although the method was developed based on average SPT or CPT values, it should be applied to all measured values for added conservatism and improved delineation of loose zones.

2. Estimate the cyclic resistance ratio (*CRR*) from various published plots that give *CRR* as a function of $N_{1,60}$ or q_{t1N} and fines content. Alternatively, *CRR* may be computed using spreadsheets or other computer programs based on equations that approximate the curves shown in the published plots.

3. Compute the safety factor against triggering based on pore-pressure increase using *CSR*, *CRR*, and appropriate corrections for earthquake magnitude, overburden, and shear stress using the following relationship (Youd et al., 2001):
$FS = (CRR7.5 / CSR) \times MSF \times K\sigma \times K\alpha$ (7-1)
Methods for evaluating *CSR*, *CRR*, *MSF*, $K\sigma$ and $K\alpha$ are discussed below.

4. If the safety factor against a pore-pressure increase in a zone is greater than 1.4, then it can be assumed that the earthquake shaking will not be strong enough to trigger strength loss in that zone. For seismic stability analyses, the peak undrained strength *Sup* (but not more than the peak drained strength) may be used in that zone. If the safety factor (*CRR*/*CSR*) in a zone is less than 1.0, then triggering of strength loss should be assumed, and for seismic stability analyses, the undrained, steady-state (residual) strength *Sus* should be used in that zone. For safety factors between 1.0 and 1.4, triggering of strength loss is possible. Either assume that triggering of strength loss will occur or perform more rigorous triggering analyses (strain-based or stress-based methods, as discussed in Section 7.4.2.3) to make a final evaluation of whether or not triggering occurs.
***Commentary**: The safety factor of 1.4 is recommended guidance and is intended to account for the strength loss that can be triggered even if the pore-pressure increase is substantially lower than 100 percent.*

2.3.3.1 Evaluation of Cyclic Stress Ratio (CSR)

The cyclic stress ratio (*CSR*) at a particular depth is given by (Engineering and Design Manual. Coal Refuse Disposal Facilities 2009):

$$CSR = \tau_{av} / \sigma'_{vo}$$

Where:

τav = average cyclic shear stress induced by the event = 0.65 τmax (force/length2)

$\sigma'vo$ = effective vertical overburden stress (force/length2)

$$CSR = (\tau_{av} / \sigma'_{vo}) = 0.65 \, (a_{max} / g) \, (\sigma_{vo} / \sigma'_{vo}) \, r_d$$

Where:

amax = maximum horizontal acceleration at the ground surface (e.g., top of embankment) (mass × length/time2)

g = acceleration of gravity (mass × length/time2)

σ_{vo} = total overburden stress (force/length2)

σ'_{vo} = effective vertical overburden stress (force/length2)

r_d = stress reduction coefficient (1.0 at the ground surface, decreasing with depth) (dimensionless)

Note that (Engineering and Design Manual. Coal Refuse Disposal Facilities 2009):

$\tau_{av} = 0.65 \, \tau_{max}$

τ_{max} = peak seismic shear stress at any depth = $(\sigma_{vo}) \, (a_{max} / g) \, (r_d)$

$\tau_{max} / \sigma_{vo} = (a_{max} / g) \, (r_d)$

The stress reduction coefficient r_d is determined by replacing the product (a_{max} r_d) by the acceleration of the layers within the fine coarse refuse in the impoundment (k_{max}) and then using the figure below to provide a value for r_d. The figure shows an estimate based on published relationships of variations in depth-dependent maximum acceleration ratio variations where y is the depth below the surface of the target layer and h is the embankment height (Engineering and Design Manual. Coal Refuse Disposal Facilities 2009).

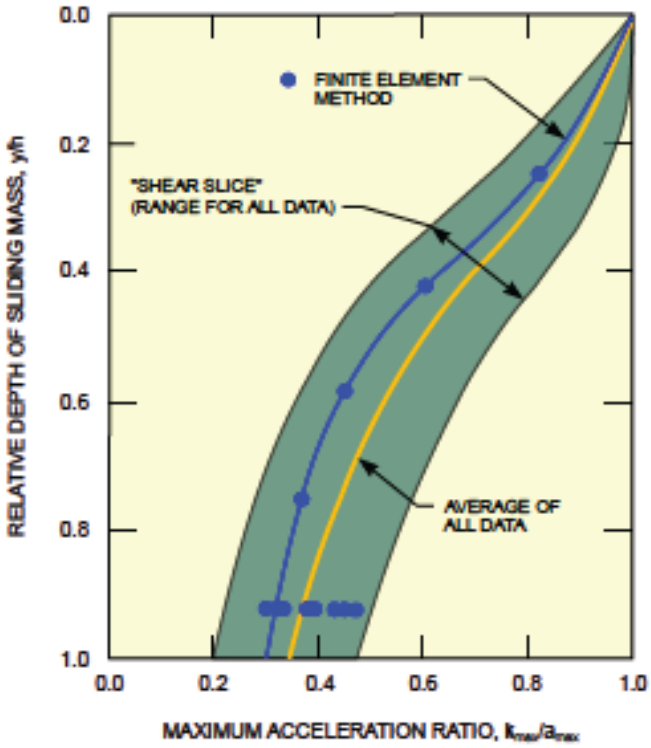

Figure 9 Variation of Maximum Acceleration Ratio with Depth of Sliding Mass *(Engineering and Design Manual. Coal Refuse Disposal Facilities 2009)*

2.3.3.2 Evaluation of Cyclic Resistance Ratio (CRR)

The normal procedure for evaluating CRR is based on earthquake events that have known the magnitude. The calculations are based on an earthquake with a magnitude of 7.5 and CRR calculated for earthquakes of other magnitudes are corrected to a magnitude 7.5 so that published curves can be used to determine CRR (Engineering and Design Manual. Coal Refuse Disposal Facilities 2009). However, in this research, the event is not an earthquake but blast vibrations from blasting operations near an impoundment. Given the different energy level and frequency of blast vibrations from earthquake seismic activity, the simplified method of determining CRR based on magnitude is not applicable. The University of Kentucky research performed cyclic triaxial testing on samples from two impoundments. (Salehien 2013). As a result, it was determined that an event or "earthquake capable of producing equivalent shear stresses of laboratory apply CSR values, has a duration equivalent to the number of uniform cycles applied in the laboratory, it is possible that it will induce peak pore pressure ratios ($r_u = 1.0$) in the coal mine tailings material" (Salehien 2013). These laboratory applied CSR values become the CRR values used in the analysis to determine if liquefaction is likely in the measured blast events.

Table 1: *Summary of Entire In-situ and Laboratory Geotechnical Properties (from Salehien 2013)*

sample name	depth (ft)	LL %	PI %	e	CSR	N_{ru}	τ_p psi	τ_r psi	$(N_1)_{60}$ (blows/ft)	$(N_1)_{60CS}$ (blows/ft)	q_t (psf)	Q_{tN}	Q_{tNCS}	f_s psf	S_{pf} (psf)	S_{rf} (psf)
TBBLAPST11S3	36.5	30	0	0.62	0.3	92	5.2		1	6	8.6	6	56.4	420	652	326
TBBLDPST4S1	144.8	38	5	0.72	0.29	12	13.6		0	5	18.5	2.3	38.9	920	652	326
TBBLDPST4S2	145.5	38	5	0.72	0.21	155	5.4		0	5	20.4	2.8	36.5	640	652	326
TBBLDPST4S3	146.2	38	5	0.78	0.25	47	6.7		0	5	25.8	3.8	47.3	1260	652	326
TBBLAPST16S1	135.3	43	7	0.96	0.43	2	10.3		5	11	13.4	1.3	27.7	460	869	543
TBBLAPST16S2	136	43	7	1.23	0.34	3	7		5	11	14.1	1.5	29.7	520	869	543
TBBLAPST12S1	55.3	33	8	0.62	0.2	79	7.7		0	5	7.6	2.6	46.8	600	652	217
TBBLDPST1S2	84.9	39	9	0.55	0.26	70	8.1		0	5	11.3	2.6	37.8	460	434	217
TBBLDPST1S3	85.6	39	9	0.58	0.32	6	7.9	2.9	0	5	10.3	2	33.5	360	434	217
TBBLDPST2S2	105.5	37	10	0.97	0.36	4	5.5		1	6	12.6	2	34.8	520	543	217
TBBLDPST2S3	106.1	37	10	0.97	0.27	20	12		1	6	13	2.2	43.3	1080	543	217
TBBLDPST2S4	106.7	37	10	0.89	0.2	140	20.9		1	6	13.6	2.9	47.1	1080	543	217
TBBLAPST15S1	115.2	39	10	0.56	0.24	55	4.5		1	6	12.6	1.7	31.4	460	652	217
TBBLAPST15S2	115.8	39	10	0.62	0.34	6	21		1	6	12.5	1.6	31.3	500	652	217
TBBLAPST15S3	116.4	39	10	0.62	0.28	24	14.2		1	6	12.9	1.7	31.7	480	652	217
TAFLBPST1S2	171.2	39	10	0.52	0.41	7	45.6	14.1	4	9	24.9	2.9	42.7	1240	4963	1809
TBBLDPST3S2	125.4	38	11	0.72	0.17	109	39.6		1	6	16.9	2.6	44.2	1200	597	272
TBBLAPST13S4	76.7	36	12	0.62	0.28	11	4.1		0	5	8.5	1.7	37	580	217	109
TBBLAPST14S3	96.5	38	14	0.97	0.29	11	8.6	2.1	0	5	10.1	1.5	33.7	580	652	217
TBBLAPST14S4	97	38	14	1.07	0.26	20	7.8		0	5	10.5	1.6	32.6	480	652	217
TAFLAPST1S1	239.6	38	14	0.52	0.37	21			10	0					9306	6204
TAFLBPST3S1	219.6	42	16	0.61	0.36	124	48.5		0	5	26.1	2	35.9	1240	8065	3412
TAFLBPST3S2	220.1	42	16	0.64	0.4	37	51	15.9	0	5	27.3	2.2	40.6	1800	8065	3412
TBBLDPST1S1	84.3	39	9	0.64	0.2		14.6		0	5	10.2	2	34.9	400	434	217
TAFLBPST2S1	200	43	16	0.51	0.4		37.6	11.7	2	7	24.8	2.2	38.7	1400	6204	2482
TAFLBPST2S2	200.6	43	16	0.51	0.32		30.6	7.1	2	7	24.5	2.1	37.7	1260	6204	2482

Definitions:

Depth: depth of the location relative to the surface

PI: Plasticity Index

CSR: Cyclic Stress Ratio

τ_p: Peak laboratory measured vane shear

(N1)60: Overburden corrected SPT blow counts (blows/ft)

q_t : pore water pressure corrected CPT Test tip resistance

Q_{tNCS} : Clean sand corrected normalized CPT tip resistance

S_{pf} : Peak field vane shear resistance

LL: Liquid Limit

e: Void ratio

Nru : Number of cycles to obtain peak pore pressure ratio (ru=1.0)

τ_r : Residual laboratory measured vane shear

(N1)60CS: Fines content corrected (N1)60

Q_{tN}: Normalized and pore water pressure corrected CPT Test tip resistance

Fs: CPT Sleeve friction

S_{rf} : Residual field vane shear resistance

2.4 Pore Pressure Effect on Stability: Total Pressure vs. Pore Pressure

Any force applied to soil is going to produce stress and pressure on the soil. (Dunnicliff, 1993) Stress and pressure are defined as force per unit area with typical units of pounds per square inch (psi) or Pascals (Pa). (Dunnicliff, 1993) Total stress is the total force transmitted across an area divided by that area. (Dunnicliff, 1993) Soils have void spaces that are filled with air or water. (Dunnicliff, 1993) In saturated or water-filled soils, total stress is equal to effective stress plus pore water pressure as shown in the following equation. (Dunnicliff, 1993)

$$\sigma = \sigma' + \mu \qquad (1)$$

Where:
σ = total stress,
σ' = effective stress,
μ = pore water pressure.

This relationship is known as Terzaghi's principle of effective stress. (Dunnicliff, 1993) Effective stress is defined as the force acting between the points of the mineral skeleton or points of contact among the soil particles per total area. (Dunnicliff, 1993) Pore water pressure is defined as the pressure in the water that fills the void spaces. (Dunnicliff, 1993) As soil becomes consolidated, a gradual squeezing out of the water in the soil with an accompanying transfer of total stress to effective stress and a decrease in pore water pressure. (Dunnicliff, 1993) The volume of the soil decreases and the grains of soil are presses closer together as the water leaves the soil matrix. (Dunnicliff, 1993) This increase in effective stress means that it is now harder to cause sliding between the grains because they are pressed closely together, increasing the soil's shear strength. (Dunnicliff, 1993) Shear strength is the resistance of the soil to sliding between its grains. (Dunnicliff, 1993)

When a load is applied to soil, whether it is gravitational or overburden vertical load or a lateral shearing load, the force is transferred to the soil, and the soil consolidates and settles under the load. (Dunnicliff, 1993) If a large enough force is transferred to the soil, it will tend to fail along a circular failure plane where shearing forces overcome the shear strength of the soil. (Dunnicliff, 1993) If the pore water is not allowed to dissipate, pore water pressure increases. As pore water pressure increases, effective stress decreases and,

consequently, shear strength decreases. (Dunnicliff, 1993) If shear strength is reduced below the level of stresses on the soil and the soil consists of small granular material, vibration can cause the soil to liquefy and flow. (Dunnicliff, 1993)

When monitoring impoundment behavior over time, there is an important difference in pore water pressure behavior in two very well defined stages of impoundment operative life; initial and final stages. In the initial stage, immediately post-construction, the effects of consolidation could produce a residual effect where the water pore pressure excesses would be the sum of the water pore pressure excesses generated by the construction of the impoundment plus the water pore pressure excesses, if any, generated by the dynamic forces when a mining blast event affect the impoundment. This is more relevant for upstream constructed impoundments. Upstream constructed impoundments are in a state of continuous construction, and the measurement or assessment of the water pressure excesses are generally difficult to evaluate and distinguish from the blast-induced water pressure excess.

In the final stage, with initial consolidation completed, it is reasonable to assume that there are not water pressure excesses generated by the construction process and the excesses in the pore pressure, if any, are the consequence only of the blast-induced dynamic forces absent a seismic event.

2.5 Pore Pressure Measurement: Static vs. Dynamic

There are commercially available a wide option of devices to measure the water pore pressures in earth materials. The definition of the appropriate device is related to the water parameter to be measured (water table, steady state water pressure, pore water pressure excess, etc.) and the characteristics of the saturated materials. Groundwater level or water table is defined as the upper level of a body of groundwater where the pressure is atmospheric. (Dunnicliff, 1993) Steady state water pressure or equilibrium water pressure is defined as the pore water pressure associated with soil that is in equilibrium, not loaded or when consolidation is complete after loading. Pore water pressure excess occurs during loading or consolidation and is the pressure of the pore water that exceeds equilibrium water pressure. (Dunnicliff, 1993) Measurement applications fall into two general categories: monitoring water flow, and providing an index of soil mass strength. (Dunnicliff, 1993) For

our purposes, the second category is key, measurement of pore water pressure as an estimation of effective stress and shear strength. (Dunnicliff, 1993)

For this project, Casagrande type open standpipe piezometers are used to allow instruments to be lowered before each blast and recovered after each blast due to the cost of the sensors. Casagrande type piezometers are not favored because of the reliance on the seal of the soil with the outside of the casing and potential damage to instruments as the casing moves downward due to consolidation from added overpressures of added lifts at the surface. (Dunnicliff, 1993) However, the concerns about sealing are more applicable to more solid embankment material, and Casagrande type piezometers are more useful in clayey soils similar to the fines in a coal refuse impoundment because the soil readily seals with the casing. (Dunnicliff, 1993) The limitation concerning the movement of the casing downward applies to more long-term instrumentation where, for this project, the instruments are located within the casing on a short term basis. Open standpipes have proved reliable with a long successful performance record, self-de-airing, seal integrity can be checked, can be converted to a diaphragm piezometer, can be used to check groundwater, and can be used to check permeability. (Dunnicliff, 1993) There is a long lag time in the readings. (Dunnicliff, 1993)

The types of piezometers available are varied. Twin-tube hydraulic piezometers consist of a porous filter element connected to two plastic tubes with a Bourdon tube pressure gauge on the end of each tube with the resultant pressure being the average of the pressure readings. (Dunnicliff, 1993) This instrument has proved reliable with inaccessible components having no moving parts and a long successful performance record. (Dunnicliff, 1993) However, the system needs frequent flushing and attention to many details for maintenance and operation and is normally used for long term piezometer readings in embankments. (Dunnicliff, 1993) Pneumatic piezometers consist of two tubes, a gas supply, a filter, and a Bourbon tube or gauge. (Dunnicliff, 1993) Gas is pumped into the tubes and pressure builds until it reaches the pressure at that location; once the gas pressure exceeds the target pressure, flow is indicated, the inlet valve is turned off, and the gas pressure is allowed to bleed off until the gas pressure equals the pressure at the location. (Dunnicliff, 1993) This instrument has a short lag time with the calibrated part of the system accessible and no freezing problems. (Dunnicliff, 1993) However, many details must be paid attention to in selecting the piezometer (Dunnicliff, 1993) and this instrument is not useful for dynamic

monitoring due to its nature of the operation, it reads a static value. The vibrating wire piezometer has a metallic diaphragm separating the pore water from the measuring system with a tensioned wire attached to the midpoint of the diaphragm such that deflection would cause changes in the wire tension, which changes the frequency of the wire from its natural frequency and the difference can be monitored as a strain transformed into pressure. (Dunnicliff, 1993) These piezometers are easy to read, have a short time lag, minimal lead wire effects, can be used to read negative pore pressures, and have no freezing problems. (Dunnicliff, 1993) However, special manufacturing techniques are required to minimize zero drift which makes this instrument more expensive. (Dunnicliff, 1993) Electrical resistance piezometers are available with bonded and unbonded strain gauges, but the bonded variety is costly. (Dunnicliff, 1993) Two wires are coiled around posts connected to a diaphragm which separates the measurement equipment from the pore water; deflection of the diaphragm causes one wire to lengthen while the other shortens, changing the electrical resistance which can be measured as strain and converted to pressure. (Dunnicliff, 1993) A schematic of an unbonded electrical strain gauge piezometer is shown in the figure below.

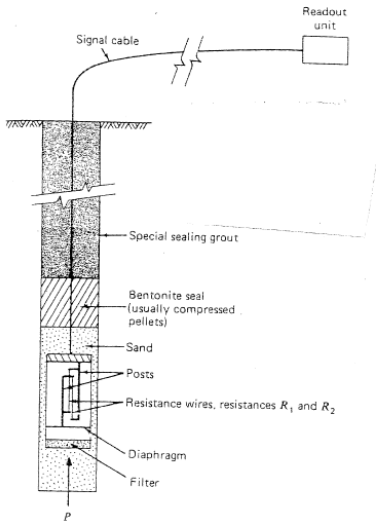

Figure 10 *Schematic of unbonded electrical strain gauge piezometer*

These instruments are easy to read, with a short time lag, can be used to read negative pore pressures, can be used for dynamic measurements, and have no freezing problems. (Dunnicliff, 1993) However, the instruments have low electrical output with lead wire effects, and errors could be caused by moisture and electrical connections. (Dunnicliff, 1993)

Due to their lesser cost and usefulness for dynamic measurement, electrical resistance piezometers are chosen for this project.

In this research, the major objective is to be able to measure the water pore pressure excess due to the ground motion generated by the blasting activity, so multiple-point piezometers using strain gauge principles or pore pressure transducers are preferred.

2.6 Preliminary Investigation of Instruments

In related research to gain preliminary data to better understand pore pressure response to dynamic blasting events, scaled tests have been performed inside a sand tank constructed of a Galfab 20 cubic yard dumpster filled with sand. (Larson-Robl et al. 2015)

Figure 11 *Galfab gasketed open top container where tests were performed. (Larson-Robl et al. 2015)*

Testing was performed at the University of Kentucky Explosive Research Team (UKERT) test facility located underground at the Nally and Gibson Quarry in Georgetown, Kentucky. Testing was performed in two parts, dry conditions, and saturated conditions. Before each dry condition blasting test, the sand material was compacted using a Mikasa plate compactor to maintain consistent density between tests. (Larson-Robl et al. 2015) The sand cone method for measuring the in-place density of soils was used, determining the average dry density of the compacted sand tank material to be 113.4 lb./ft^3 (1,816 kg/m^3). (Larson-Robl et al. 2015) The charges were set off at a depth of 18 inches (0.46 m) below the sand surface and 3.5 ft. (1.1 m) from the end and sides of the tank. (Larson-Robl et al. 2015) Standard geophones with attached accelerometers were set at 2.5 ft. (0.76 m), 4.5 ft.

(1.4 m), and 14.5 ft. (4.4 m) from the charge and buried 12 inches (0.30 m) below the sand surface. All instruments were centered 3.5 ft. (1.1 m) from either side of the tank. (Larson-Robl et al. 2015) The figure below shows a diagram of the instrumentation and charge setup within the container.

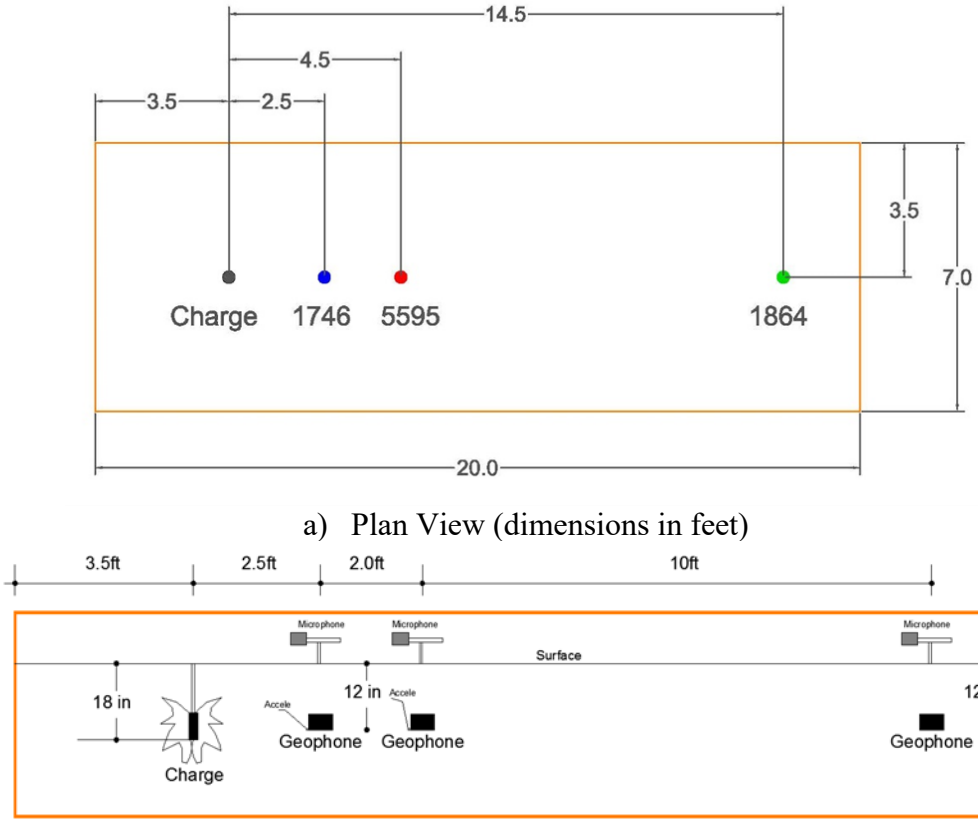

Figure 12 *Sand tank setup a) plan view, b) cross-section view. (Larson-Robl et al. 2015)*

The closest seismograph, unit 1746, at 2.5 ft. (0.76 m) from the charge was a NOMIS Mini-Graph® 7000 with three PCB Piezotronics ICP® Uniaxial Accelerometers in each component (x, y and z), model number 352B01. (Larson-Robl et al. 2015) The middle seismograph, unit 5595, was a White Mini-Seis™ with a PCB Piezotronics ICP® Triaxial Accelerometer, model number 356A02, as shown in the figure below. (Larson-Robl et al. 2015)

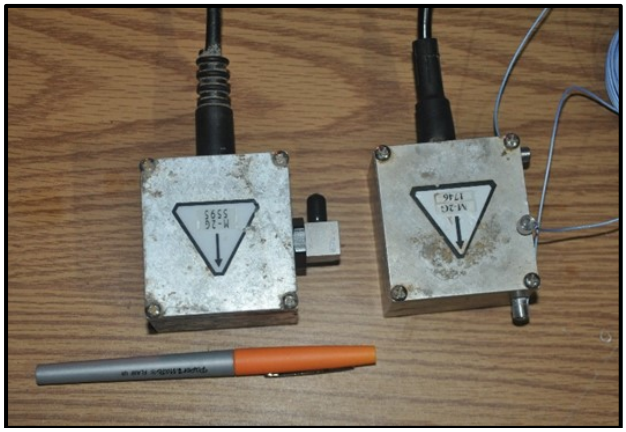

Figure 13 *Left: seismograph unit 5595 with a triaxial accelerometer, Right: seismograph unit 1746 with uniaxial accelerometers in each component. (Larson-Robl et al. 2015)*

The farthest seismograph at 14.5 ft. (4.4 m) from the charge was another NOMIS Mini-Graph® 7000, no accelerometers were attached here. (Larson-Robl et al. 2015) The accelerometers were used in junction with a MREL DataTrap II. (Larson-Robl et al. 2015) The PCB Piezotronics ICP® Triaxial Accelerometer was calibrated 05/07/14, and the PCB Piezotronics ICP® Uniaxial Accelerometers were calibrated 06/16/14. (Larson-Robl et al. 2015) Seismograph microphones were also placed inches (0.30 m) above the sand at these locations. (Larson-Robl et al. 2015)

Before blasting tests, the geotechnical properties of the sand were determined through lab tests. (Larson-Robl et al. 2015) Grain size analysis was performed according to ASTM standards D422 and D1140 and classified using the Unified Soil Classification System resulting in a poorly-graded sand with 1.2% gravel, 97.7% sand, and 1.1% silt and clay as shown in the figure below. (Larson-Robl et al. 2015)

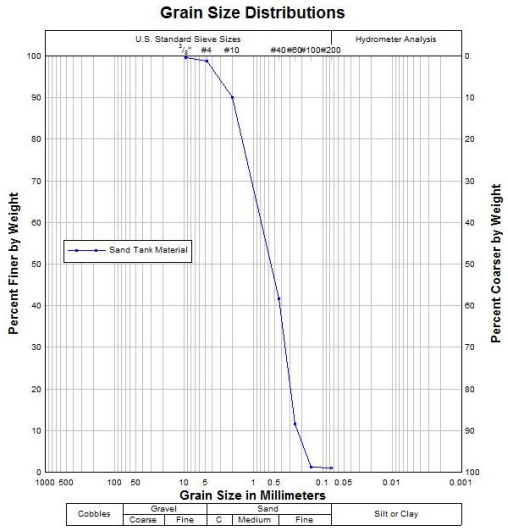

Figure 14 *Grain Size Distribution (from Larson-Robl et al. 2015)*

The moisture content, assumed to be constant over the duration of the test series as the sand tank was housed underground, was determined according to ASTM D2216 to be 3.87%. (Larson-Robl et al. 2015) Direct Shear tests were performed using a ShearTrac-II Direct Shear Apparatus by Geocomp, shown in the figure below, according to ASTM D3080 in both unsaturated and saturated conditions. (Larson-Robl et al. 2015)

Figure 15 *ShearTrac-II Direct Shear Apparatus by Geocomp (from Larson-Robl et al. 2015)*

The moisture content during the unsaturated direct shear tests was 5.6%. (Larson-Robl et al. 2015) The resulting data was used to create a Mohr-Coulomb failure envelope; assuming a cohesionless material, the friction angle of the material unsaturated was determined to be 38.8° as shown in the figure below. (Larson-Robl et al. 2015)

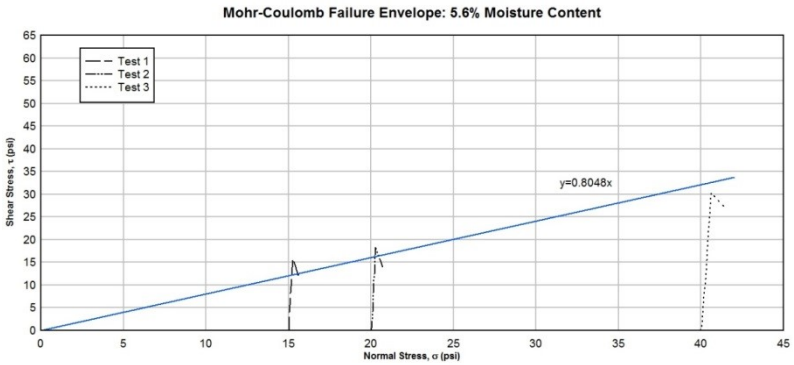

Figure 16 *Failure envelope to determine the friction angle during unsaturated conditions. (from Larson-Robl et al. 2015)*

The saturated laboratory tests resulted in a friction angle of 56.7°, again assuming a cohesionless material as shown in the figure below. (Larson-Robl et al. 2015) Standard and modified Proctor tests (ASTM D698 and ASTM D1557) were performed to determine an optimum water content of the saturated sand, but the results proved erroneous given the nature of the material. (Larson-Robl et al. 2015)

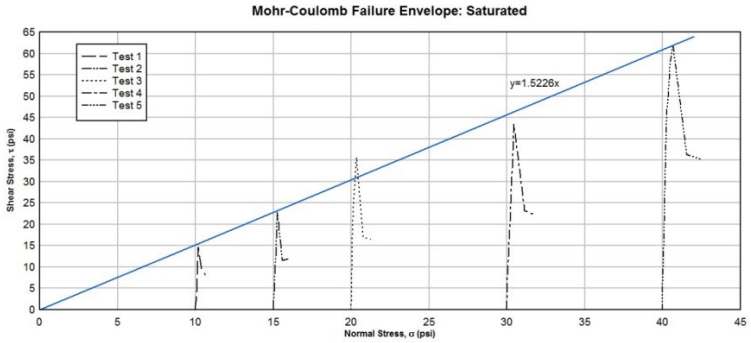

Figure 17 *Failure envelope to determine the friction angle during saturated conditions. (from Larson-Robl et al. 2015)*

Three tests were performed under unsaturated conditions. For each test, a 20 g cast booster as shown in the figure below, initiated using an electric detonator, was buried in the sand by first driving a hollow steel pipe into the sand and removing it to produce a "drill hole," and then lowered into the hole with sand poured and tamped into the hole to couple the charge to the surrounding material. (Larson-Robl et al. 2015)

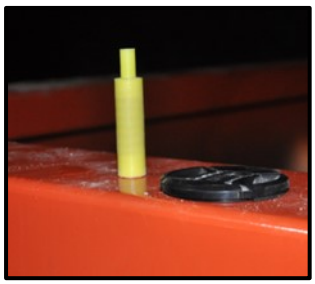

Figure 18 *20 g cast booster (from Larson-Robl et al. 2015)*

The three figures below show the typical particle velocity vs. time curve obtained from the geophones used during test 1 in the radially, vertically, and transverse component respectively. (Larson-Robl et al. 2015)

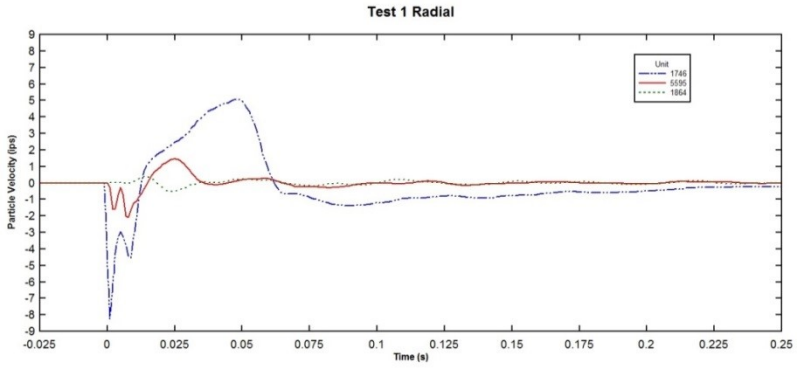

Figure 19 *Radial particle velocity obtained from each unit during test 1. (from Larson-Robl et al. 2015)*

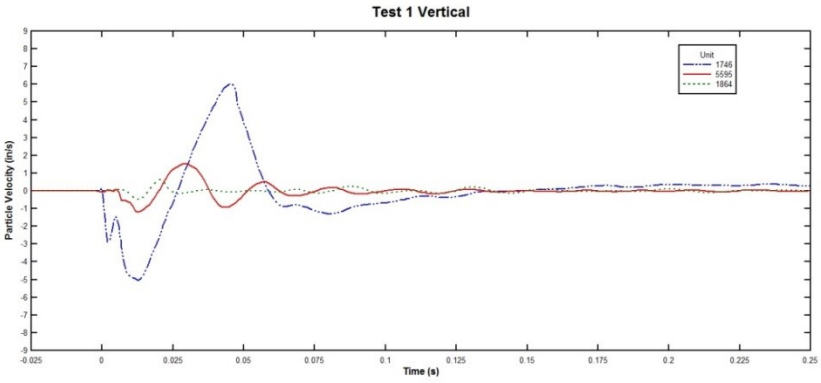

Figure 20 *Vertical velocities obtained from each unit during test 1. (from Larson-Robl et al. 2015)*

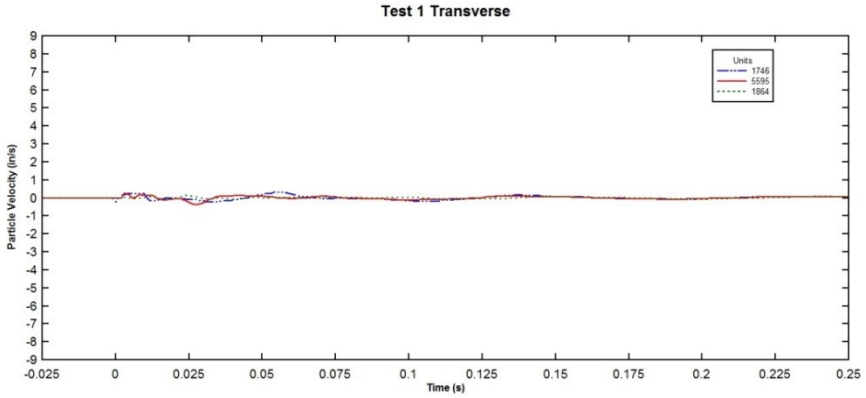

Figure 21 *Transverse velocities obtained from each unit during test 1. (from Larson-Robl et al. 2015)*

The table below shows the peak particle velocity (PPV) data and the calculated scaled distances (SD) for each test. To calculate scaled distances, the square root scaling method was chosen. (Larson-Robl et al. 2015)

Table 2: *Summary of testing data with calculated scaled distances. (from Larson-Robl et al. 2015)*

Test 1					Peak Particle Velocity (ips)		
Charge (g)	Charge (lbs)	Unit	Distance to charge (ft)	Scaled Distance (ft/lbs^½)	Radial	Vertical	Transverse
20	0.044	1746	2.5	11.9	5.04	6.00	0.32
		5595	4.5	21.4	1.44	1.56	0.26
		1864	14.5	69.1	0.39	0.64	0.15
Test 2					Peak Particle Velocity (ips)		
Charge (g)	Charge (lbs)	Unit	Distance to charge (ft)	Scaled Distance (ft/lbs^½)	Radial	Vertical	Transverse
20	0.044	1746	2.5	11.9	5.28	6.16	0.56
		5595	4.5	21.4	1.48	1.60	0.22
		1864	14.5	69.1	0.38	0.64	0.175
Test 3					Peak Particle Velocity (ips)		
Charge (g)	Charge (lbs)	Unit	Distance to charge (ft)	Scaled Distance (ft/lbs^½)	Radial	Vertical	Transverse
20	0.044	1746	2.5	11.9	5.84	6.08	0.48
		5595	4.5	21.4	1.32	1.56	0.20
		1864	14.5	69.1	0.355	0.60	0.18

Square root scaled distance is calculated using the following formula:

$$SD = \frac{R}{\sqrt{W}} \qquad (2)$$

Where:
SD = square root scaled distance
R = distance from blast to the point of interest
W = maximum charge-weight detonated within any 8-millisecond delay (ISEE, 2011)

The following figure shows the peak particle velocity versus scaled distance graph. (Larson-Robl et al. 2015)

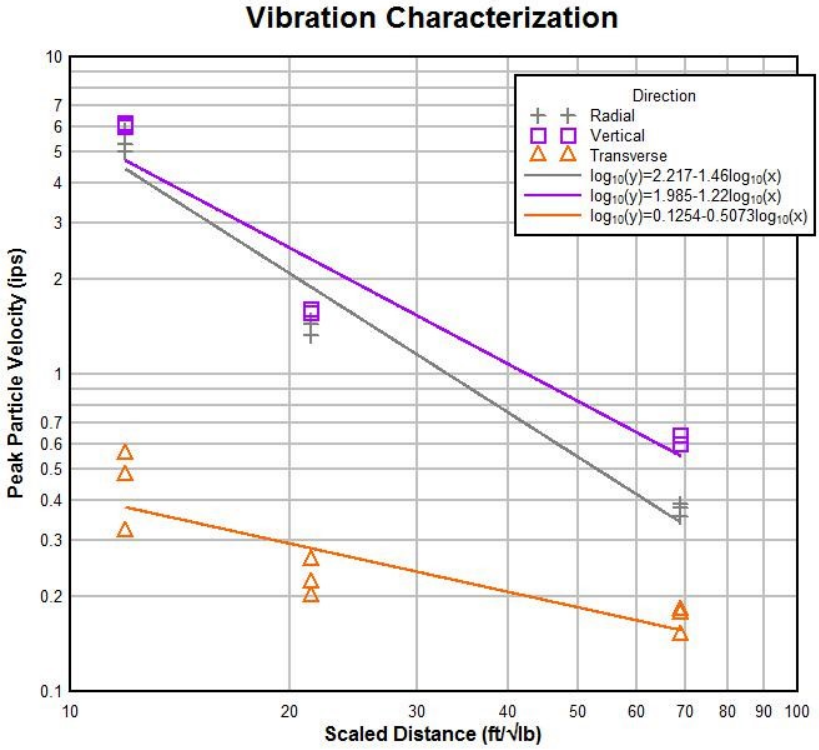

Figure 22 *PPV versus scaled distance graph of all tests with attenuation lines for radial, transverse, and vertical directions. (from Larson-Robl et al. 2015)*

Two factors influence vibration amplitude (measured as PPV), charge-weight (an increase in charge-weight increases amplitude) and distance. (ISEE, 2011) Geologic material changes can also impact vibration amplitude. (ISEE, 2011) Due to the controlled conditions of the setup in the lab for the tests (i.e. using a fixed charge weight, uniform material, and controlled variation of distance, the values of peak particle velocity are very consistent test-to-test. (Larson-Robl et al. 2015) With such low variability, it is possible to assess the equation of peak particle velocity versus scaled distance for dry conditions in the three components as (Larson-Robl et al. 2015):

Radial

$$PPV_{radial} = 164.81 * (SD)^{-1.46} \qquad (3)$$

Vertical

$$PPV_{vertical} = 96.60 * (SD)^{-1.22} \quad (4)$$

Transverse

$$PPV_{transverse} = 1.33 * (SD)^{-0.50} \quad (5)$$

To test under saturated conditions, the sand tank was filled with water up to six inches below the surface. (Larson-Robl et al. 2015) With the exception of the added water and saturated sand, all equipment and conditions (burial depths, distances, charges, etc.) remained consistent with those during the unsaturated testing. (Larson-Robl et al. 2015)

To collect excess pore pressure data, several tests were performed using tourmaline piezometers. (Larson-Robl et al. 2015). Initially, strain gauge piezometers were selected from RST Instruments, LTD, using strain gauge (SG) pressure transmitters with a ported nose and blast overpressure protection. Along with the piezometers, a FlexDAQ Series 800 Datalogger is used to record the measurements from the piezometers.

In order to monitor the pore water pressure during a blast event, the instrument must be able to record at a sampling rate high enough (sub-millisecond to the millisecond) to capture the initial peak caused by the blast. In the initial stages of the current research to measure pore water pressure excesses due to blasting, it was noted that strain gauge piezometers have a response time of approximately four seconds which results in missing the first four seconds of the dynamic event, consequentially, the entire blast event. (Charlie et al., 2001) The result is an inability to measure the residual pore pressure and peak values during this event, values which may be higher or lower than the values provided by the piezometer. (Charlie et al., 2001). The RST piezometers on hand have a sampling rate of 33 samples per minute or every 1.8 seconds. The search for a conventional strain gauge piezometer with an appropriate sampling rate for dynamic measurements during blasting events revealed no adequate instruments. However, research has revealed that the RST piezometers may be used in conjunction with an instrument with an appropriate sampling rate to capture the entire impact of the blast on pore pressure within the impoundment. Because of that, tourmaline sensors were investigated.

Given that typical sampling rates between 1,024 and 2,048 samples per second are used to measure vibration from blasting, the piezometers used in the first attempt were far from the adequate sampling rate. (Larson-Robl et al. 2015). Tourmaline pressure sensors are expensive, sensitive and sophisticated instruments with limited availability in the market.

(Larson-Robl et al. 2015) However, discussions with several sensor manufacturers revealed that tourmaline sensors have been used in several research projects when the desire is to monitor pressure during a blasting event. Consequently, two tourmaline pressure sensors (PCB Piezotronics) W138A were acquired for this research. (Larson-Robl et al. 2015) Data of pore pressures with calculated square root scaled distances is shown in the table below. (Larson-Robl, 2015)

Table 3: *Summary of saturated testing data with calculated scaled distances. (from Larson-Robl, 2015)*

Test 1						
Charge (g)	Charge (kg)	Unit	Distance to charge (m)	Scaled Distance (m/kg^½)	Peak Pore Pressure (psi)	Peak Pore Pressure (kPa)
20	0.020	Tourmaline 1	0.3302	1.2	133.0592	917.4108892
		Tourmaline 2	0.7874	2.9	5.887874	40.59546218
Test 2						
Charge (g)	Charge (kg)	Unit	Distance to charge (m)	Scaled Distance (ft/lbs^½)		
20	0.020	Tourmaline 1	0.3302	1.2	141.3039	974.2560946
		Tourmaline 2	0.7874	2.9	7.052326	48.6240761
Test 3						
Charge (g)	Charge (kg)	Unit	Distance to charge (m)	Scaled Distance (ft/lbs^½)		
20	0.020	Tourmaline 1	0.3302	1.2	135.8877	936.9127102
		Tourmaline 2	0.7874	2.9	8.80814	60.72998748
Test 4						
Charge (g)	Charge (kg)	Unit	Distance to charge (m)	Scaled Distance (ft/lbs^½)		
20	0.020	Tourmaline 1	0.3302	1.2	119.7793	825.8492019
		Tourmaline 2	0.7874	2.9		

The following figure shows the peak pressure versus scaled distance graph. (Larson-Robl, 2015)

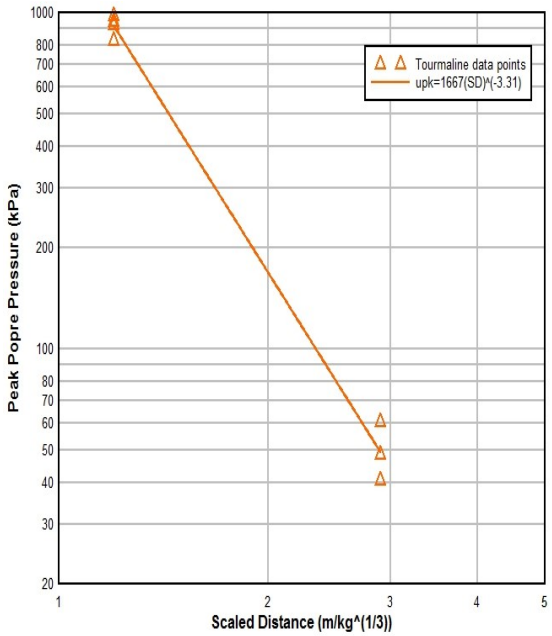

Figure 23 *Peak pressure versus scaled distance. (from Larson-Robl, 2015)*

When compared to equations produced from other researchers investigating blast-induced pressure in the sand, the saturated sand results gave lower pressure than others as shown in the figure below. (Larson-Robl, 2015) This difference could account for variation in the properties of the material used.

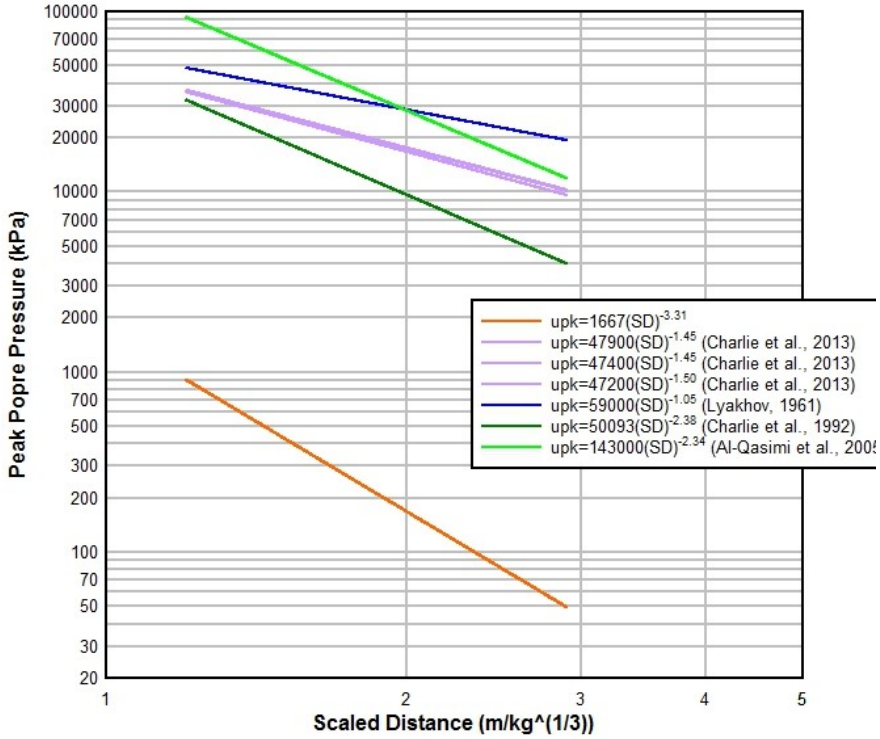

Figure 24 *Peak pressure versus scaled distance. (from Larson-Robl, 2015)*

Graphs of data from the tourmaline sensors are shown in the figure below. (Larson-Robl, 2015)

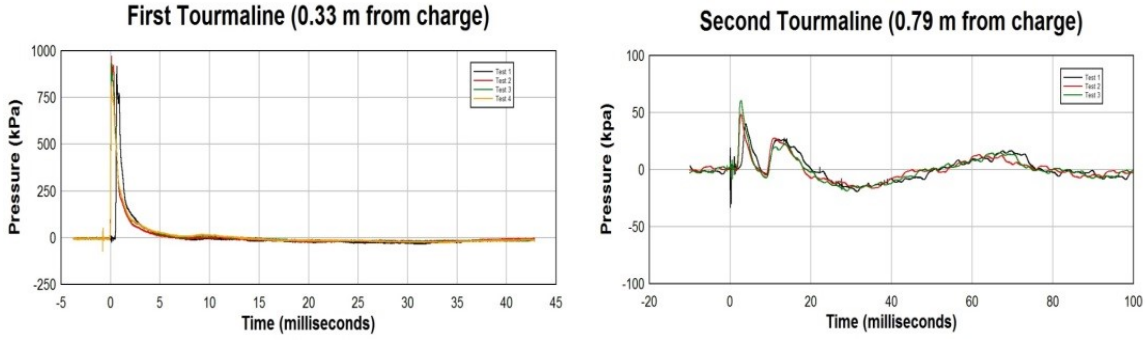

Figure 25 *Tourmaline test results in saturated conditions. (Larson-Robl, 2015)*

The figure above shows results that have been tediously filtered in an attempt to reduce the noise in the signal. The collected data revealed that the signal from tourmalines is very noisy such that measurement of very low levels of dynamic pressure as is expected in the impoundment may be lost in the noise of the signal. (Larson-Robl et al. 2015) The problems experienced with tourmaline sensors triggered the need to exchange some ideas about this system with experienced researchers using this system. (Larson-Robl et al. 2015) According to this exchange of ideas with other scholars, it was concluded that tourmaline sensors are very good sensor devices but those instruments had several limitations making the collection of information tedious tasks where several trial and errors are needed. (Larson-Robl et al. 2015)

After these tests, the concern was that a buried tourmaline tested total pressure and not just pore pressure which is a part of the total pressure (total pressure = pore pressure + interstitial or particle pressure). Proof-of-concept testing was performed in the sand box. A screening device was constructed to allow only water to contact the tourmaline sensor as shown in the figure below.

Figure 26 *Tourmaline sensor without (on left) and with (on right) screening device*

However, due to the noise in the tourmaline sensors, the difference in pore pressures could not be definitively assessed. More testing is needed to overcome the limitations of the sensors.

At the same time, proof-of-concept tests using a tourmaline sensor in a standpipe similar to the Casagrande type piezometers (standpipe with slits in the lowest ten feet of pipe) used in most impoundments were performed to determine applicability. Tests were performed under saturated conditions. Explosive charges were set off at equal distances to the standpipe and other sensors. Data analysis indicates that measurements in standpipes may be used for dynamic analysis.

Given the signal from tourmalines is very noisy such that measurement of very low levels of dynamic pressure as is expected in the impoundment may be lost in the noise of the signal, a new sensor using a PCB Piezoelectric pressure sensor encased in a metal shield with #230 mesh to allow only water to come in contact with the sensor was developed and tested. The resultant signal is much less noisy, and the new sensor is able to measure low levels of dynamic pressure. It was noted that both the tourmalines and the new sensor stabilized to zero once dynamic load ceased. The concern is that residual pore pressures would be more static than dynamic in nature which would consequently not be measured by the tourmalines or new pressure sensor due to the slower rate of decreasing load. Therefore, the tourmaline sensors or new sensor will be used in conjunction with the RST instruments on hand to measure pore pressure, not only to catch the first part of the explosive event but also to capture the residual pore pressure that could result from blast vibrations.

3. Project Methodology

The plan for this project covers theoretical and practical aspects. Theoretical aspects will include mathematical modeling of blasting vibration effects on impoundment materials using 3D finite element analysis. Practical aspects include analyzing the dynamic geotechnical characteristics of fine coal refuse, from published sources, from a selected impoundment and from a recent research project at the University of Kentucky (Salehian 2013), to determine an adequate set of characteristics for model configuration and threshold values for liquefaction. These threshold values will first be used to determine if current field data for blasting vibrations approach or surpass the thresholds to predict model response. From work at a selected impoundment, field values of particle velocity, acceleration, and pore pressure will be used to verify and calibrate model response. Once the model is

calibrated, several runs of varying blast strength and distance, modeled as vibrational load, will be performed to determine what limit values will potentially cause failure in the impoundment.

These results will be used to create a nomogram for guidance when blasting near impoundments.

3.1 Project Goals and Objectives

The general objective of the project is the analysis of slope stability of impoundments (coal refuse/slurry) over time under static and specifically under dynamic conditions produced as consequences of the blasting activity in a surface coal mine. Several specific objectives support the general objective with a combination of field measurement and study, computational and numerical modeling of the impoundment structures, validation of the models with field measurements, and development of simulations for highly dynamic blast events that could cause failure of the impoundment structures. The following is a more specific list of objectives.

- Study of the generation of water pore pressure excess, if any, and particle velocity/acceleration in impoundments due to dynamic loads produced by the mining production blasting activity in a surface coal mine near to impoundments.
  .
- Computational evaluation (modeling) of coal refuse impoundments subject to dynamic activity produced by production blasting in a surface coal mine.

- Determination of the best practices for blast design in a surface coal operation when impoundments are the structures under protection or close to the production area. The result should be a guide to determine stability ratings or factors to consider when blasting near impoundment structures.

The hypotheses to be tested is the low generation of water pore pressure excess and relative low accelerations in the body of the impoundment as a result of the ground motion due to mine blasting. These hypotheses are supported by the fact that no impoundment failures have been related to dynamic blast activity in the U.S. Also, several subsurface nuclear test developed in the U.S. Navajo Dam, New Mexico (maximum PPV @ toe 0.5 cm/s

(0.19 in/s) and @ crest 1.3 cm/s (0.51 in/s)); Rifle Gap Dam, Colorado (maximum acceleration @ toe 0.1g and @ crest 0.2g) showed little or no increase in pore pressure excess, (Rouse and Roehm 1969, Rouse et al. 1970, and Ahlberg et al. 1972, see Charlie, U.S. Bureau of Reclamation, November 1985). The data gained from the first objective above will be used to calibrate the model. If pore pressure data is not available, seismograph data will be used to calibrate the model. Once calibrated, the vibrational forces can be varied to study if any pore pressure and subsequent liquefaction is generated in the impoundment.

3.2 Work Plan

3.2.1 Site Description of Impoundment

The impoundment used in this project is located in West Virginia and is part of an Appalachian coal mine which mines both surface and underground coal. The following figure shows the impoundment.

Figure 27 *Impoundment at Study Site.*

The preparation plant on site generates both CCR and FCR which is placed in the impoundment. The impoundment is currently finishing its fourth stage of development and is beginning construction of the fifth stage. The figure below shows a cross-sectional view of the impoundment.

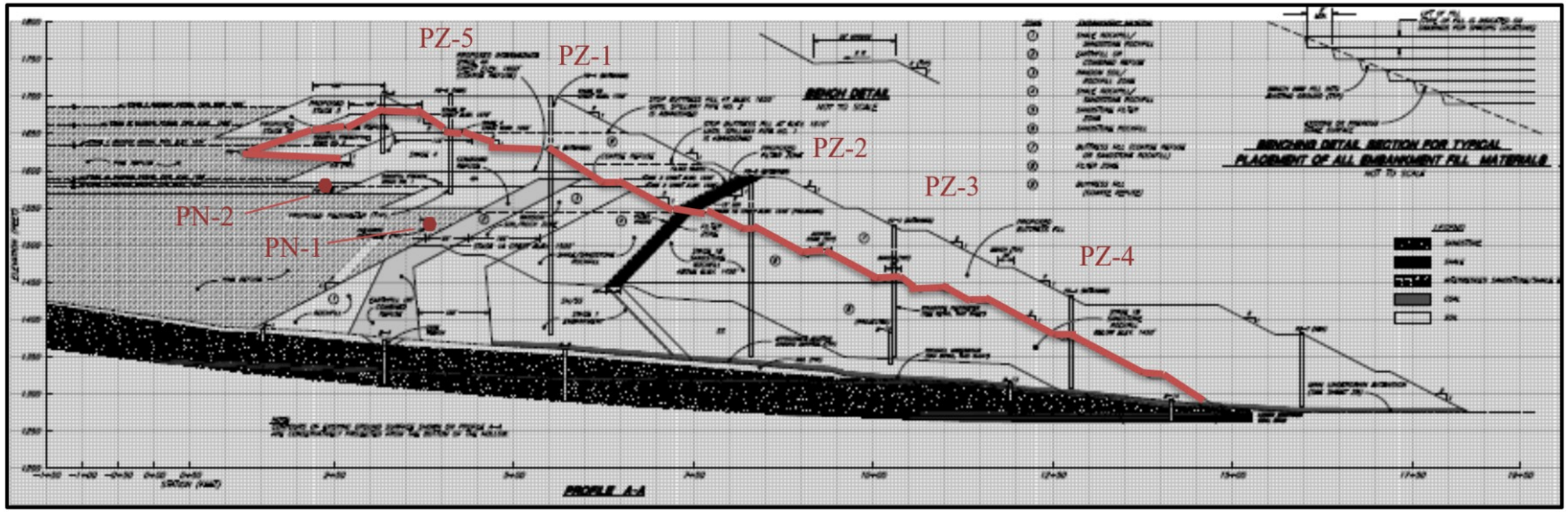

Figure 28 *Cross-sectional View of Dam Stages (Modified from GeoEnvironmental Permit Drawing, 2009)*

The figure below shows a closer cross-section of the dam.

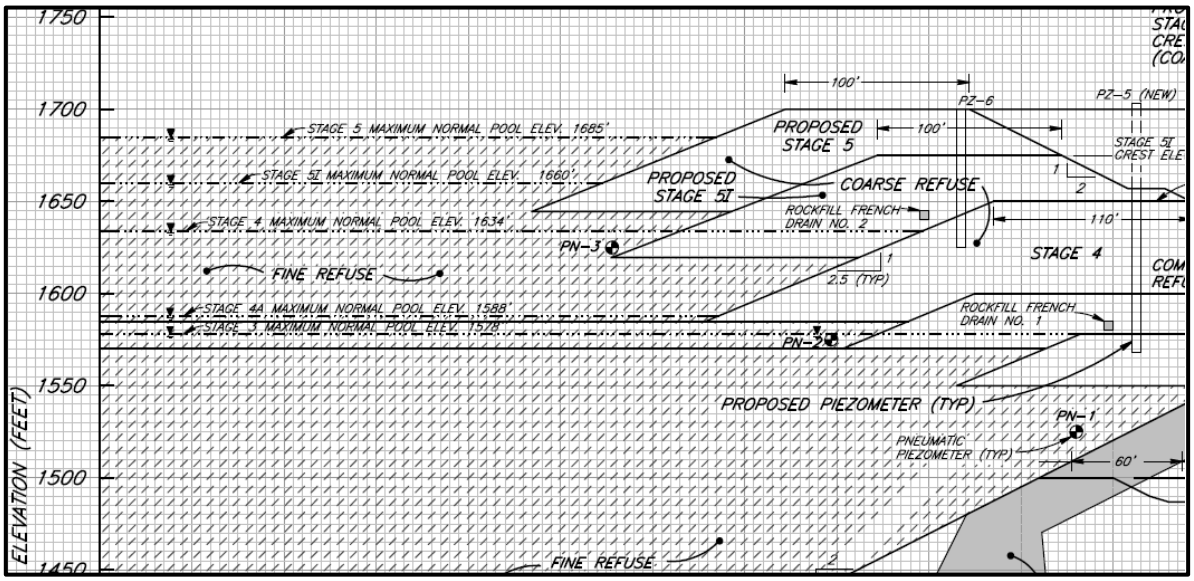

Figure 29 *Cross-section of Dam (Modified from GeoEnvironmental Permit Drawing, 2009)*

The dam is a cross-valley upstream construction with earth fill and rockfill sections as needed for stability. (GeoEnvironmental, 2010) Coarse refuse is placed in one-foot lifts and compacted by a D-8 dozer or an equivalent weight of loaded haul truck. (GeoEnvironmental, 2010) Fine refuse is placed hydraulically using slurry lines on the upstream face of the dam. (GeoEnvironmental, 2010) Fines are pumped across the dam to build a uniform beach of fines across the impoundment. (GeoEnvironmental, 2010) The impoundment is designed to reach a stage 5 dam elevation of 1700 feet with a pool elevation of 1685 feet. (GeoEnvironmental, 2010) Piezometer 5 (PZ-5) is currently installed, but piezometer 6 (PZ-6) has yet to be installed. A pushout of coarse material has recently been constructed on top of the slurry upstream of the dam at 1650 feet elevation, the same elevation of stage 4 as shown in the figure below.

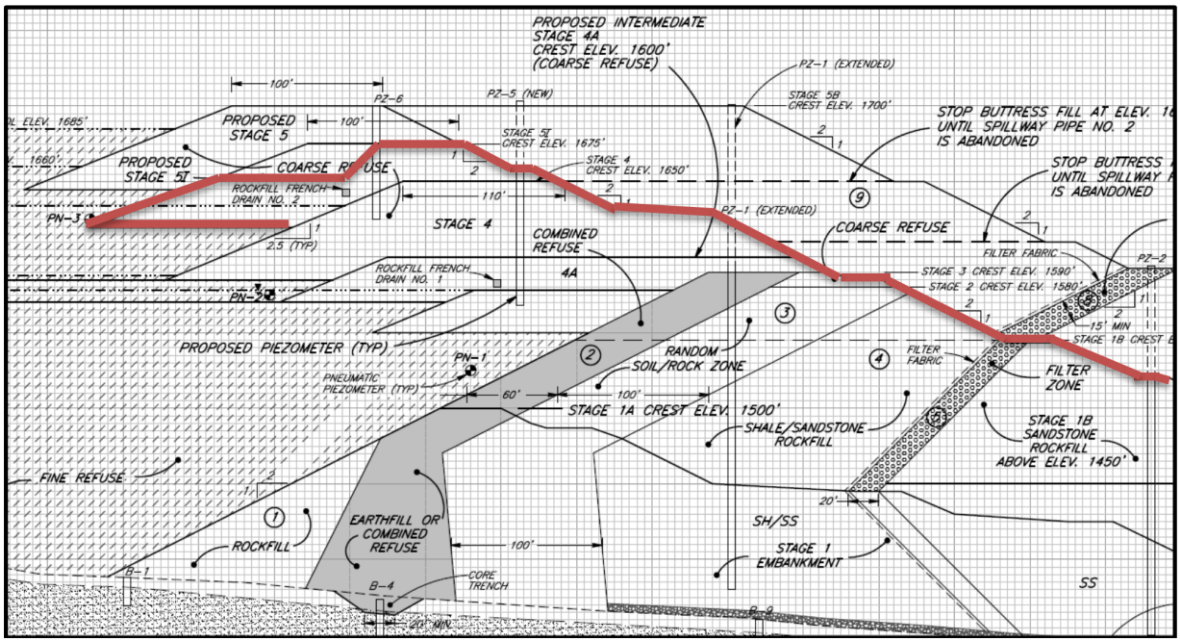

Figure 30 *Cross-section of Dam Showing Pushout (Modified from GeoEnvironmental Permit Drawing, 2009)*

To provide more storage space for coarse refuse produced by the plant, the coal company is blasting and mining a surface coal seam adjacent to the north side of the impoundment as shown in the figure below.

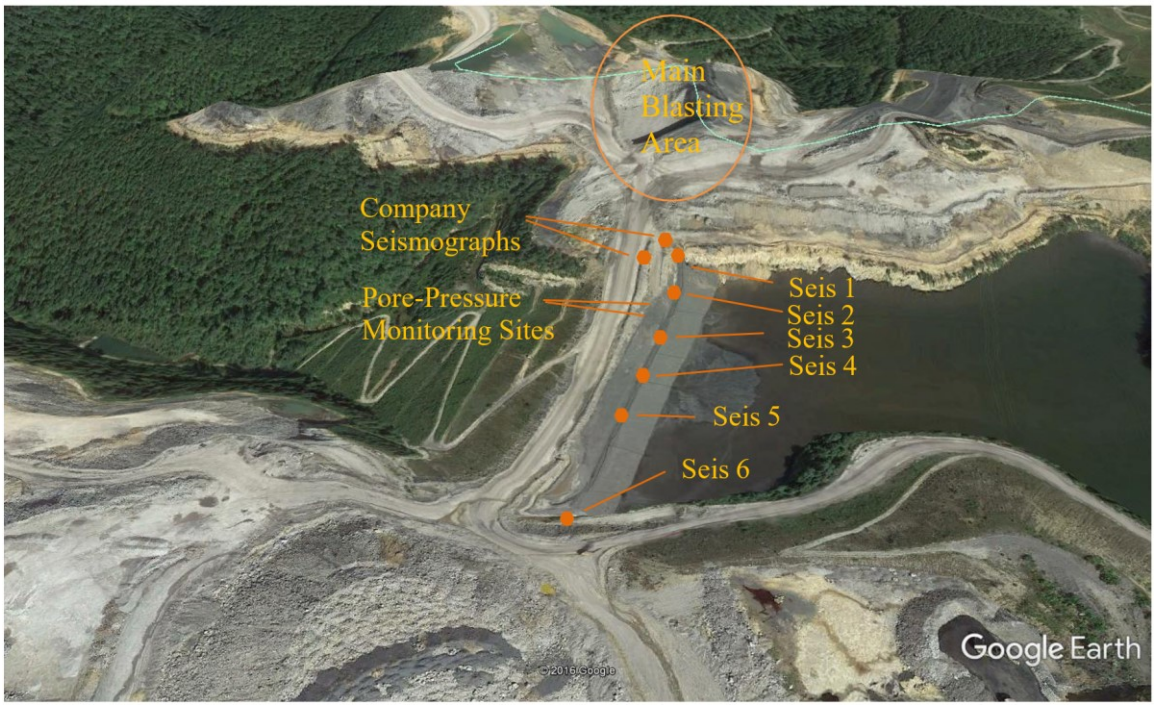

Figure 31 *Aerial Photo Showing Main Blasting Area (Google Earth, 2015)*

3.2.2 Dynamic Measurement Plan

The study of dams or other earth structures under dynamic conditions requires complete vibration time history records to evaluate the behavior of stresses and strains on the ground. The coal company has two seismographs with geophones on the north side of the dam nearest to the blasting area, with one seismograph on the solid material adjacent to the dam and the other on the coarse refuse material of the dam.

Figure 32 *Showing Company Seismograph 1 on Dam (on right) and Company Seismograph 2 on Solid Bank (on left)*

The coal company has provided copies of records from both seismographs throughout 2014 and January of 2015. The company also provided weekly piezometer records from the same period so that historic vibrational and piezometer records can be compared. Casagrande type piezometers 1-5 are located in the coarse material of the dam while pneumatic piezometers 1 and 2 are located in the fines material. During analysis of the data, it appeared that blasting did not affect the piezometer levels in the coarse material of the dam but that the piezometer levels did respond to the pool elevation, particularly piezometers #1 and #5, as shown in the following figures. However, more data over time and details on other effects on the readings would give more conclusive results. Further study is necessary.

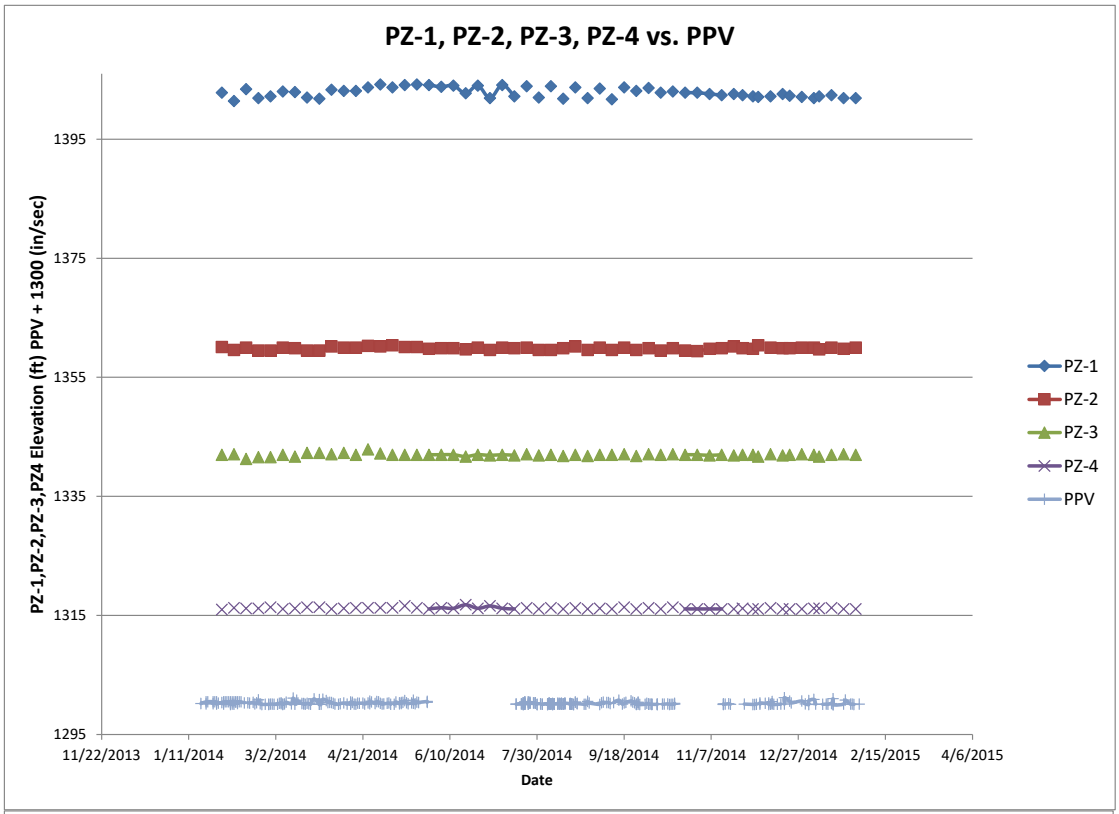

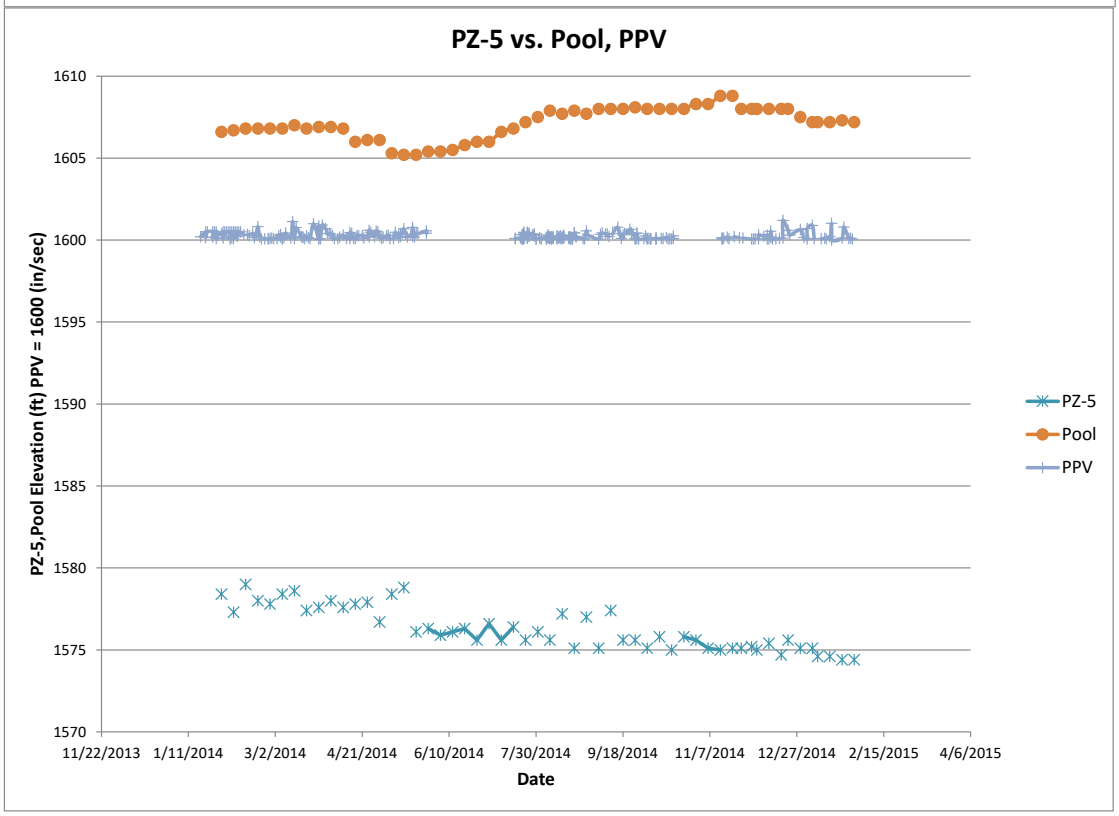

Figure 33 *Historic Piezometer and Pool Records*

Note that, in order to compare the data from the piezometers and the PPV, 1300 was added to PPV values in the upper chart while 1600 was added to PPV values in the lower chart. Otherwise, the variation in PPV data remained the same. Similarly, there appeared to be no correlation between vibrational records and pneumatic piezometer records and pool elevations. Again, for comparison purposes, 1600 was added to PPV values to create the chart below (Figure 34).

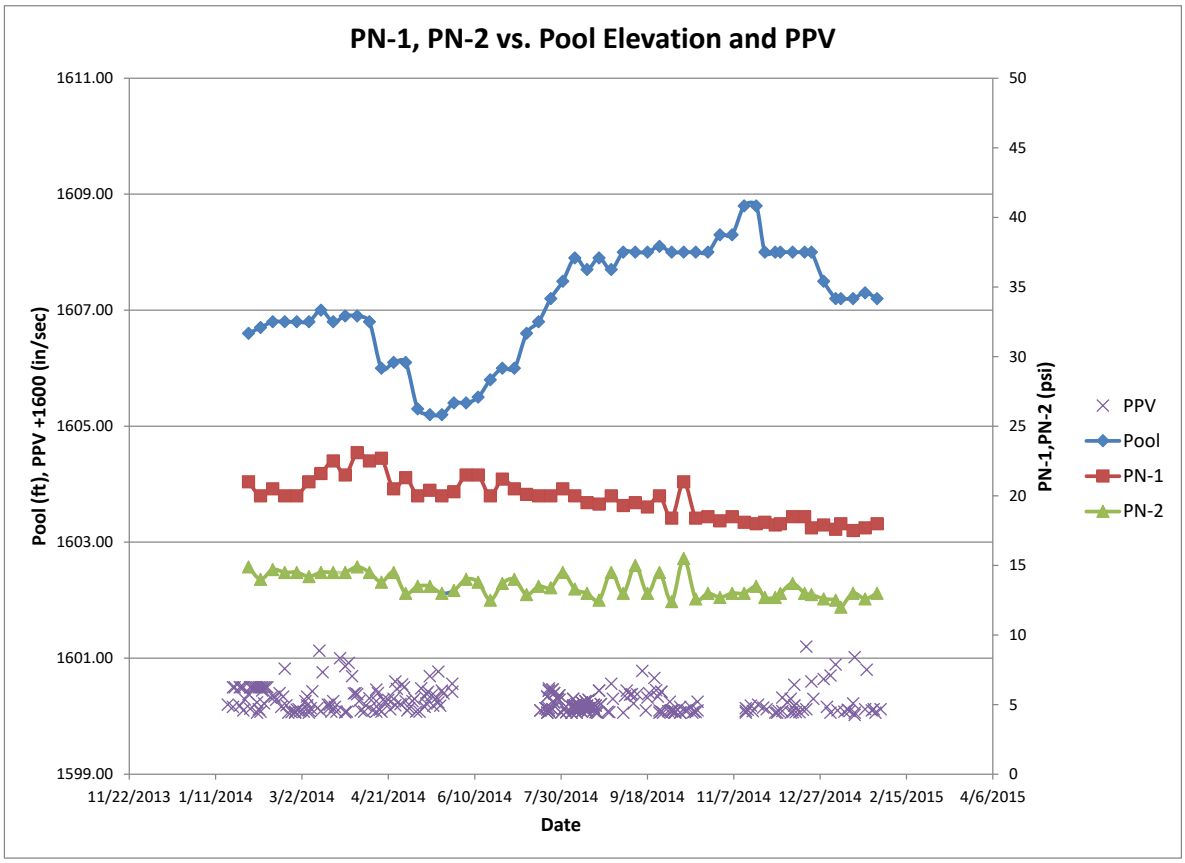

Figure 34 *Historic Pneumatic Piezometer vs. Pool and PPV Records*

Note that the record for both pneumatic piezometers trend downward as PPV and pool levels rise and fall. It appears that there is not a long-term effect of blasting on pore pressure, no residual rise in pressure due to blasting was shown by the historic records. However, more data over time and details on other effects on the readings would give more conclusive results. Further study is necessary.

Starting in June 2015, the West Virginia Department of Environmental Protection (WVDEP) placed 6 geophones and seismographs on the solid bank and along the edge of the pushout in order to monitor blast vibrations.

Figure 35 *Photos of WVDEP Seismographs along Pushout Edge*

WVDEP provided copies of blasting records and seismograph records so that an analysis of the vibrations due to blasting could be made for the locations of the seismographs. Blasting took place in two locations, the main blasting area north of the impoundment (Charges Adjacent in the chart below) and on a point adjacent to the toe of the impoundment dam just south (Charges at Point in the chart below). Vibration amplitude (measured as peak particle velocity or PPV) attenuates with increasing distance. (ISEE, 2011) Two factors influence vibration amplitude, charge-weight per delay (an increase in charge-weight per delay increases amplitude) and distance. (ISEE, 2011) The data was normalized by calculating the square root scaled distance between each blast and the seismographs. Maximum PPV is usually plotted on a log-log graph against scaled distance to give an equation that can be used for vibration prediction. (ISEE, 2011) The following figure shows the results of the analysis of WVDEP data.

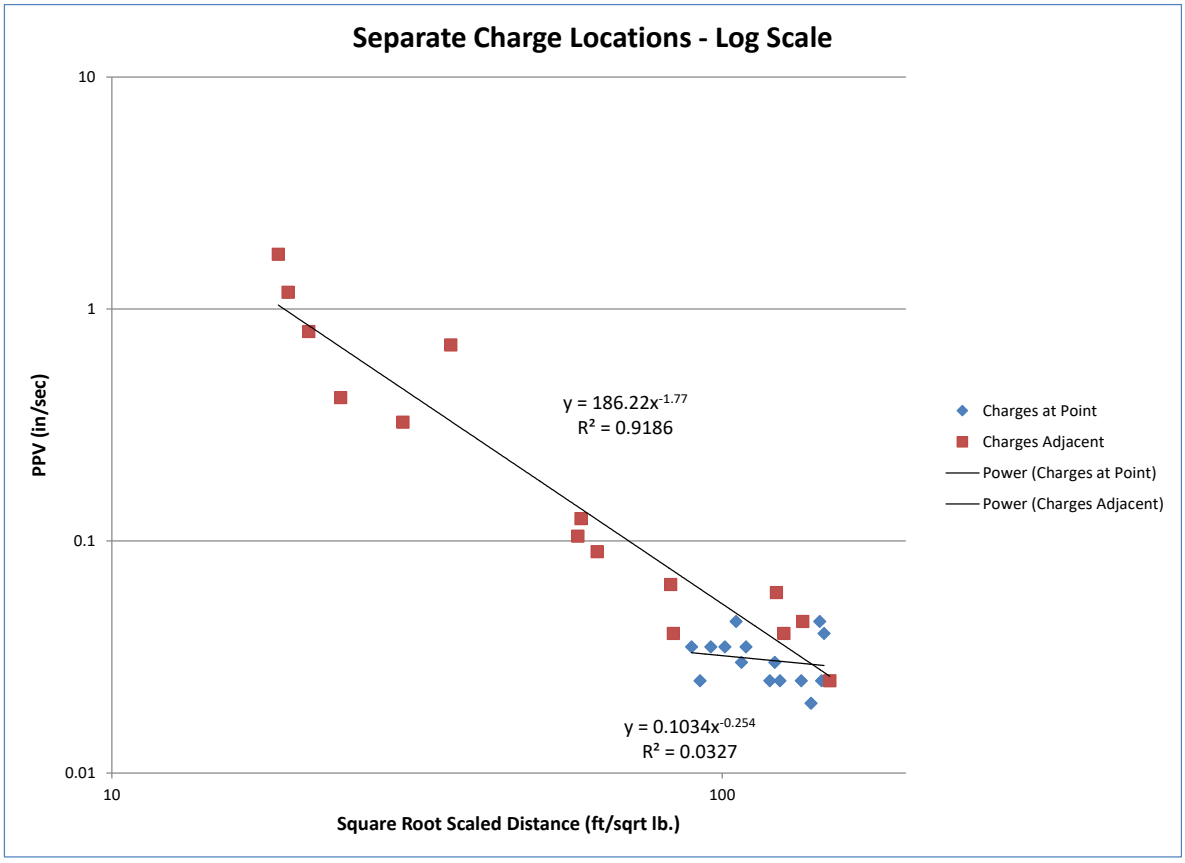

Figure 36 *WVDEP Data PPV vs. Scaled Distance*

Note that there are two sets of data for the separate locations. The equations of best-fit lines from both sets of data are shown in the chart above with Y = PPV (in/sec) and X = Square Root Scaled Distance. Research over the years has resulted in several general equations for predicting ground vibrations in lieu of site-specific data. (ISEE, 2011) The figure below compares the trend lines of several industry equations with the original data. The square root scaled distance from the original data was plugged into the various industry equations to obtain the resulting trend lines and equations shown in the figure. Note that the trend of the original data is close to the industry trend lines, particularly for quarry operations. This suggests that general equations from industry could be used to verify model outputs for vibrations from blasting inputs allowing the model to be more generally applicable to coal refuse impoundments and less site-specific.

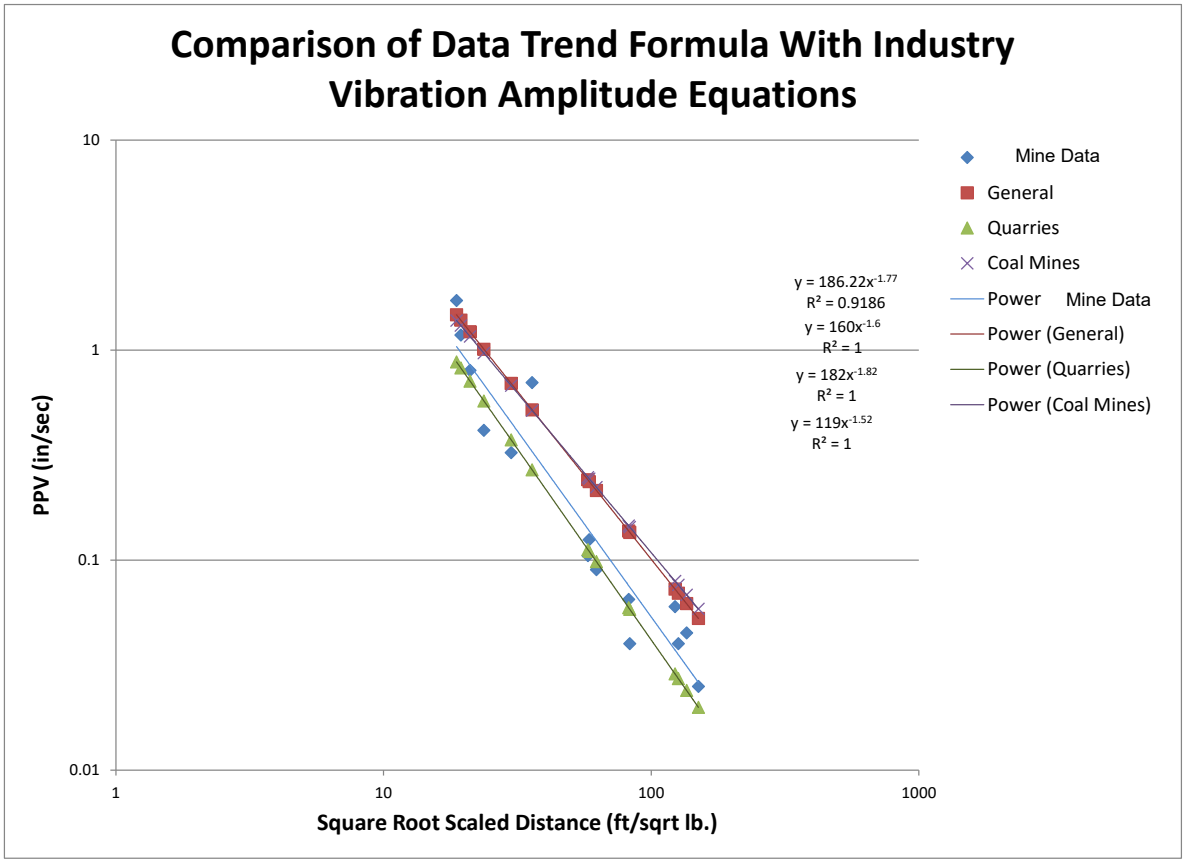

Figure 37 *Comparison of Data Trend with General Industry Equations*

With the coal refuse impoundment selected, records of geotechnical field testing (SPT and CPT test) and sampling activities were provided in the impoundment design. These records will be used to define the dynamic properties of the materials in the specific location of the project. The dynamic properties will be compared against published information from previous or ongoing research. Due to the high heterogeneity of the slurry a wide range of change in the values of dynamic parameters is expected, however, the variations will be included in the dynamic slope stability analysis performed.

Regarding vibrations, it is possible to measure accelerations or particle velocity. The measurement of these variables is preferable in the body of the impoundment at different depths. From the acceleration/velocity records, it is possible to reproduce nomograms like those developed by Makdisi and Seed (1978) for dams (Figure 2). During the development of the project, the possibility to use down-hole accelerometers was evaluated but proved to be too difficult and costly. Two holes 75 feet deep and approximately 50 feet apart along the pushout were drilled vertically through the pushout and into the fines below so that

instrumentation can be used to monitor the pore pressure in the fines. The figure below shows the cross-sectional location of the monitoring system used in the development of this project.

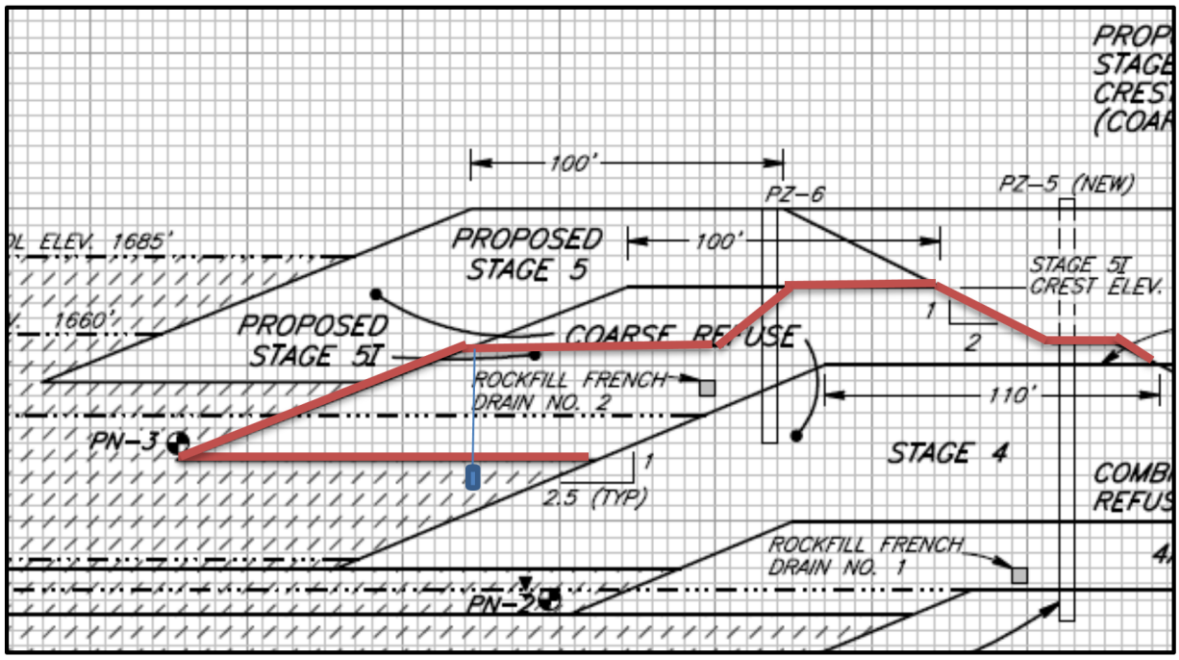

Figure 38 *Schematic Cross-sections of the monitoring system used in this research. (Modified from GeoEnvironmental Permit Drawing, 2009)*

The main variables to measure are particle accelerations/velocities, and water pore pressures in the impoundment due to ground vibrations produced by blasting.

The information collected during the monitoring stage is useful to establish the possible effects of the vibrations in the materials. Strength loss after or during the ground vibration can be evaluated. Also, this information can be used to calibrate numerical models. Further analysis of the energy, frequency, and duration of impact on any given area of the impoundment should provide an evaluation of the cyclic stress ratio and a number of vibrational cycles to compare with recently determined thresholds for potential liquefaction.

3.2.3 Model Development

The main propose of the computational evaluation objective is to develop a computer model using advanced numerical modeling techniques, finite elements or finite difference analysis to study the performance of impoundments under static and dynamic conditions. This necessary, nondestructive tool allows analysis of the consequences of exposing

simulated impoundments beyond the dynamic limit imposed by common mining production blasting.

The information collected from field tests and laboratory tests was used to attempt calibration of the computer model. Several approaches were to be used to calculate the slope stability safety factors in dynamic conditions produced by blasting to create final product recommendations about the best procedure for design and evaluation of the stability of impoundments subjected to production surface mine blasting.

Itasca's FLAC3D software was used to create computer models and to implement dynamic analysis of the effects of blasting on an impoundment. The configuration of the model is shown in Figure 39 below.

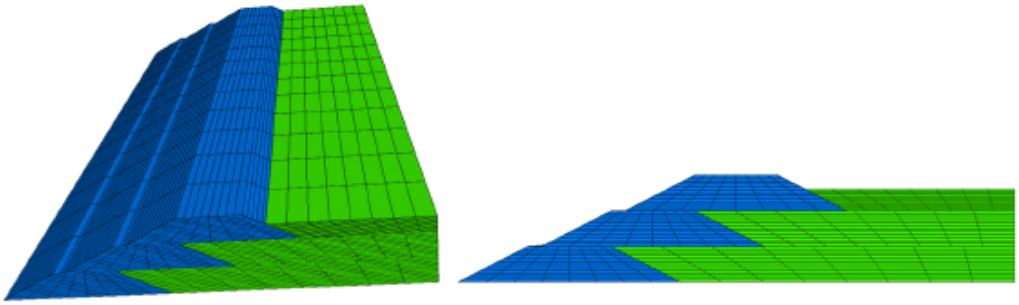

Figure 39: *Model in isometric (on left) and side (on right) views*

Note that the configuration of the model is not representative of the actual Impoundment were data was collected. The goal of this project was to create a model that was representative of coal slurry impoundments in general, specifically those using upstream construction. Thus, the model is more generic than a specific site, modeling the construction technique to study potential liquefaction in fines under the various coarse sections of the dam. Secondly, FLAC3D is so complex and detailed in its analysis that using a model that may be more representative of an in-situ impoundment creates such complexity that the run time required for analysis would potentially be days instead of hours to run one modeling scenario. Initially, properties gleaned from records for the selected impoundment were used for the coarse and fines materials so that the model could be calibrated to in-the-field responses to blasting. The model can be loaded with material properties of typical impoundments in order give results for a greater range of impoundments found on mine sites.

In order to properly represent the conditions within a coal refuse impoundment, water levels based on historic water level data are used as well to attempt to calibrate and code the

water level in the model. In order to reflect the potential behavior of the coarse and fine materials in the impoundment, a Mohr-Coulomb behavior model for all materials in the impoundment is used initially to calculate the initial stability of the impoundment and equivalent-linear analysis is used to simulate the behavior of the materials during cyclic dynamic loading.

The goal was to use complete time history records and in-situ testing data to calibrate the model to field data. Once the model was calibrated, simulated inputs were to be explored which cause the computationally simulated impoundment structures to fail. These failures were correlated to current surface mine blasting practices, and a field guide tool was produced. This blast design guide tool could help to identify the hazardous characteristics of the vibration time history generated by blast events affecting impoundments. General recommendations regarding blast design would result from the analysis when impoundments are the structures close to the blasting site.

A database was to be developed associating blasting parameters like pattern of the blast, distance from the source to recording point, the weight of explosives per delay, water pore pressure excesses, accelerations and deformations in the impoundment. From the analysis of the database, it would be possible to specify the best practices to develop the mining blast when a coal refuse impoundment is the nearest structure under protection.

The goal was to develop several nomograms involving the main variables of the problem. The main variables to be involved were the acceleration in the base and the crest of the impoundment due to blasting, water pore pressure excess, and geometry of the impoundment compared to the dynamic properties of the materials that compose the impoundment. The nomograms would include safety factors against failure for slope stability analysis under dynamic conditions due to mining blast vibrations. In the analysis, an acceleration time series history would propagate from the bottom of the impoundment to the top. The monitoring proposed, will allow for measured time series from mining blast events to be used for calibration of the models.

Using both, limit-equilibrium and dynamic methods of evaluation, safety factors under dynamic conditions for different values of the variables involved in the problem can be calculated. According to the results, recommendations about the more efficient or best procedure to evaluate the impoundment response subjected to ground vibrations due to

blasting will be given. Figure 40 shows examples of stability charts for uniform slopes (Radoslaw L., Michalowski. (2002)).

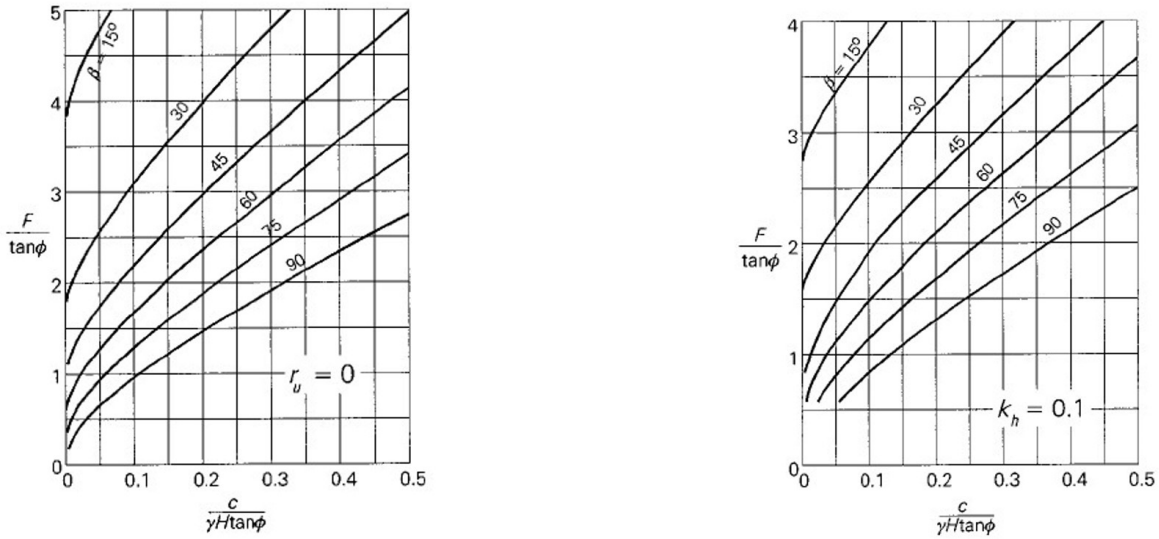

a) Static Conditions b) Dynamic Conditions

Figure 40 *Stability charts for uniform slopes (After Radoslaw L., Michalowski. 2002)*

In the figure above, the main parameters involved in the stability are included, they are:

F: Safety factor	ϕ: internal friction angle
γ: Unit weight of the soil mass	c: cohesion
H: slope high	β: slope inclination
r_u: water pore pressure parameter	k_h: dynamic horizontal acceleration

For information and theoretical background information concerning finite element modeling for dynamic analysis, a discussion is provided in Appendix 1.

3.3 Calibration of the Model

In order to calibrate the model, the data from the array of seismographs placed by WVDEP was used. Given the complexity of the model with the multiple properties and strata of differing materials, a simple model of the pushout was created to lower the potential impact from other strata, such as fines or additional coarse sections of the dam, allowing for less potential variability in the model. Similarly, an assumption is made to use a one-dimensional load only on the side of the dam. The transverse signature from

the blast is applied to the side of the dam nearest to the blast. Seismograph 1 is located on the solid just outside of the dam material and is the source of the load. This load is assumed to be applied to the side of the entire dam equally. It was soon discovered that using a Mohr-coulomb materials property did not allow for the positive and negative phases characteristic of a blasting waveform in the model but only produced a positive waveform with the little negative waveform. A switch to an elastic materials property allowed for the characteristic blasting waveform with positive and negative alternating waveforms.

In the model, grid points corresponding to the locations of the WVDEP seismographs are monitored for velocity, stress, strain, and other parameters. In order to calibrate the model, velocity values in the x-direction, x-velocity (xvel), are monitored. Seismograph 1 (Seis1) in the model is on the edge of the model nearest the blast and shows good correlation with the frequency and waveform of the load. However, the amplitude at the Seis1 location is less than the load. For the remaining seismographs on the dam (Seis 2, Seis 3, Seis 4, and Seis 5) the amplitude and frequency are much different from the corresponding transverse signatures from each seismograph. The difference in frequency was discovered by performing a Fast Fourier Transform (FFT) on the results from the corresponding seismograph and the monitored xvel from the model, hence the need for calibration of the model. These differences are likely due to the complex nature of the material in the dam versus the homogeneity of the model. Amplitude calibration is a matter of applying a multiplication factor to the model. Frequency calibration was a bit more complex. The effects of several properties (Shear Modulus, Bulk Modulus, Density, and Poisson's Ratio) on frequency were investigated. It was found that modifying the Shear modulus and Bulk Modulus had the greatest effect on frequency.

The shear modulus (G) and bulk modulus (K) are calculated using the following formulas:

$$G = E/(2*(1+\nu)) \quad (58) \text{ and,}$$

$$K = E/(3*(1+\nu)) \quad (59),$$

where,

E = Modulus of Elasticity

ν= Poisson's Ratio

In order to discover the best fit for frequency and timing to calibrate the model to the field data, the Poisson's ratio is held constant, and the modulus of elasticity is varied by roughly 20% to provide a set of Shear and Bulk moduli. The resulting moduli are found in the table below.

Table 4: *Range of Shear and Bulk Moduli used for calibration analysis.*

Material	E (psf)	Poisson's Ratio	G Shear Mod. (psf)	K Bulk Mod. (psf)	Percentage of E
Fines	454000	0.3	174615.38	378333.33	
Coarse	746000	0.28	291406.25	565151.52	100%
	1600000	0.28	625000	1212121.2	214%
	895200	0.28	349687.5	678181.82	120%
	596800	0.28	233125	452121.21	80%
	1044400	0.28	407968.75	791212.12	140%
	1193600	0.28	466250	904242.42	160%
	1342800	0.28	524531.25	1017272.7	180%
	447600	0.28	174843.75	339090.91	60%

To allow a manageable analysis for calibration purposes, the transverse seismograph data for Seis 2 and the corresponding xvel data for that location in the model are used with an assumption that the remaining material of the dam has similar properties as the material between the location of Seis 1 and Seis 2. The Shear and Bulk moduli were entered into the model and produced resulting xvel data for the Seis 2 grid point location. These data for each percentage of the modulus of elasticity were inputted into DPlot, Graphing Software for Scientists and Engineers (DPlot 2001-2004), and a Fast Fourier Transform (FFT) was performed on each data set. The resulting curves were compared with the Fast Fourier Transform curve from the WVDEP Seismograph 2 curve to determine which data set was the best fit. It was determined that the curves for 80% E and 120% E were the best fit as shown by the comparison in the figures below.

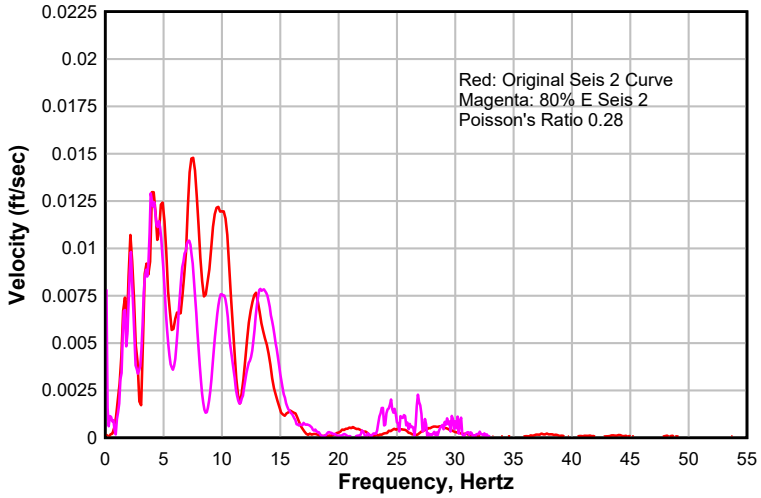

Figure 41: *Fast Fourier Transform of waveforms for Seis 2 vs 80% Young modulus (from DPlot, 2016)*

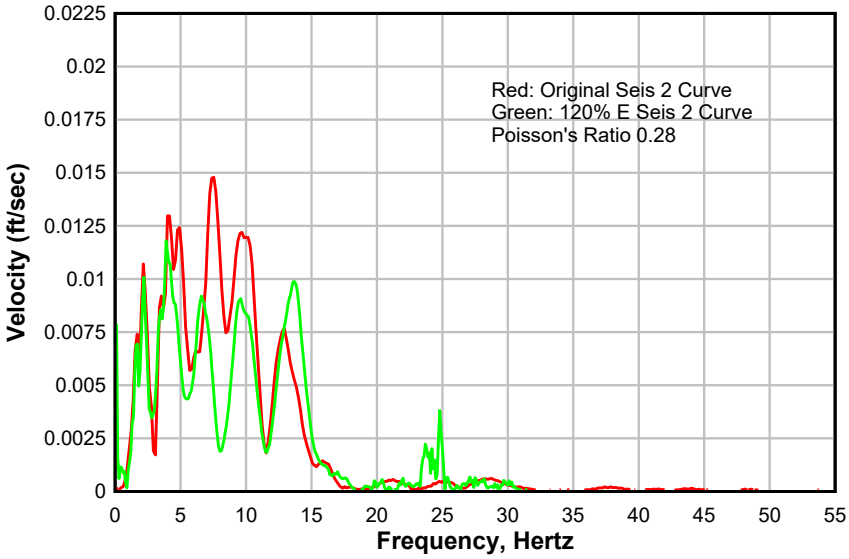

Figure 42: *Fast Fourier Transform of waveforms for Seis 2 vs 120% Young modulus (from DPlot, 2016)*

The correlation between the original Seis 2 FFT data and the range of model FFT data were calculated with the 80% E FFT data having the greatest correlation coefficient as shown in the table below.

Table 5: *Correlation Coefficients for a select range of FFT.*

FFT	Correlation Coefficient
60%	0.809
80%	0.817
100%	0.747
120%	0.767
140%	0.800
160%	0.776
180%	0.769
214%	0.776

These correlations and calibration efforts are made within DPLOT which allows for manipulation of frequencies and amplitudes. Unfortunately, making the same changes to the loading in FLAC3D has proven very difficult, and the model has not responded to several attempts to calibrate the load. 6.5 months have been spent to try to calibrate the model so that the load can be properly applied. If this load is not properly applied and calibrated, the resultant pore pressures generated by the model if any, would not be reliable and therefore could not be used in this analysis. Furthermore, calibrating frequency be modifying the properties of the materials can and most likely will result in unrealistic material properties used in the model that will be unrepresentative of any field values. Copies of the code used to create and calibrate the model are provided in Appendix 2 so that another researcher can perhaps continue to work with FLAC3D and find a solution.

In light of this setback, the analysis will turn to calculated values of CSR using the data obtained from the WVDEP seismographs with the resulting CSR compared to the CRR from the Salehian dissertation to provide an analysis whether the blasting effects will have a potential to cause liquefaction in coal fines.

3.4 Calculated Effects of Blasting on Coal Fines

Access to the study site was initially restricted due to a bankruptcy and later due to some disagreement between the new owners of the site and University of Kentucky personnel. As a result, very little data was able to be collected for the project. Access was allowed for three days but the data collected was inconclusive. A sensor array comprising a tourmaline pressure sensor and a piezometer was lowered in each piezometer hole drilled into the pushout. The tourmaline sensors did not show any reading as a result of blasting. The piezometer, which had been modified to run faster than designed, only collected data for one blast as the memory was filled by each blast unbeknownst to the operator. Unfortunately, a second chance to collect data was not available. As a result, the only available data from the site is the results from the array of six WVDEP seismographs placed along the edge of the crest of the pushout.

These seismographs were triggered each time a blast was shot resulting in peak particle velocity (PPV), frequency, and sound measurements. However, not all of the six seismographs triggered on each blast. In order to have cohesive data to analyze, shot records were analyzed, and shots, where all six seismographs or the first five seismographs were triggered, were selected for use. Seismograph six was installed in rock, so it was not used at all for the liquefaction analysis. The seismograph records constitute the blasting load on the impoundment from each shot and are shown in the table below.

Table 6: *Selected shots used to analyze liquefaction potential.*

Shot Record	Date	Time	Charge Weight /Delay (lbs/8ms)	Total Weight of Explosives (lbs)	WV Unit	Distance (ft)	Scaled Distance	PPV (in/s)	Frequency (hertz)	Acceleration (g)
332	6/22/2015	1425	5389.1	173994.1	1	1375.8	18.74119	1.72	8.3	0.23238019
332	6/22/2015	1425	5389.1	173994.1	2	1427	19.43864	1.18	8.2	0.157502852
332	6/22/2015	1425	5389.1	173994.1	3	1543.7	21.02833	0.8	3.1	0.040368652
332	6/22/2015	1425	5389.1	173994.1	4	1740.9	23.71459	0.415	5.5	0.037153809
332	6/22/2015	1425	5389.1	173994.1	5	2201.2	29.98482	0.325	7.6	0.040205875
332	6/22/2015	1425	5389.1	173994.1	6	2636.6	35.91585	0.7	13.1	0.149266345
394	7/27/2015	1359	1004.3	36131.7	1	1809.7	24.65179	0.085	10	0.01383603
394	7/27/2015	1359	1004.3	36131.7	2	1860.9	58.72071	0.125	8.6	0.017498508
394	7/27/2015	1359	1004.3	36131.7	3	1978.2	62.42211	0.09	7.2	0.010547938
394	7/27/2015	1359	1004.3	36131.7	4	2175.7	68.65423	0.05	9.4	0.007650511
394	7/27/2015	1359	1004.3	36131.7	5	2636.5	83.19477	0.04	12.8	0.008334173
397	7/28/2015	902	2800.2	66026	1	1034.3	32.63734	1.18	9.8	0.188235116
397	7/28/2015	902	2800.2	66026	2	1085.4	34.2498	1.02	10.2	0.169353005
397	7/28/2015	902	2800.2	66026	3	1204.4	38.00485	0.56	9.4	0.085685719
397	7/28/2015	902	2800.2	66026	4	1402.5	44.2559	0.285	5.8	0.026907009
397	7/28/2015	902	2800.2	66026	5	1865.1	58.85324	0.205	3	0.010010775
397	7/28/2015	902	2800.2	66026	6	2300.6	72.59545	0.18	15	0.043949742
164	4/7/2016	1657	919.5	64451.25	1	1545.7	48.77457	0.33	6.9	0.037064282
164	4/7/2016	1657	919.5	64451.25	2	1596.2	50.3681	0.29	7.7	0.036348064
164	4/7/2016	1657	919.5	64451.25	3	1716.9	54.17679	0.3	5.1	0.024904854
164	4/7/2016	1657	919.5	64451.25	4	1914.5	60.41206	0.17	5.6	0.015496353
164	4/7/2016	1657	919.5	64451.25	5	2377.3	75.01572	0.145	6	0.014161583
168	4/11/2016	1644	901.5	50484	1	1461.3	46.11133	0.315	6.8	0.034866795
168	4/11/2016	1644	901.5	50484	2	1511.8	47.70486	0.365	7.2	0.042777749
168	4/11/2016	1644	901.5	50484	3	1632.6	51.5167	0.42	7.3	0.049907373
168	4/11/2016	1644	901.5	50484	4	1830.1	57.74882	0.2	5.1	0.016603236
168	4/11/2016	1644	901.5	50484	5	2292.9	72.35247	0.125	3.6	0.007324957
168	4/11/2016	1644	901.5	50484	6	2727.1	86.05366	0.08	15	0.019533219

"Seed and Lee (1966) defined initial liquefaction as the point at which the increase in pore pressure is equal to the effective confining pressure." (Kramer, 1996). Excess pore pressure required to initiate liquefaction is dependent on the amplitude and duration of cyclic loading. (Kramer, 1996) The cyclic stress approach is used to characterize the load. (Kramer, 1996) This approach is based on the assumption that excess pore pressure generation is based on cyclic shear stress. (Kramer, 1996) However, laboratory data used to estimate liquefaction resistance have uniform amplitude while blasting waveforms do not. (Kramer, 1996) For a comparison to work, the non-uniform blasting waveforms need to be converted to uniform stress cycles. (Kramer, 1996). In 1975, Seed et al. determined that the cyclic shear stress τ_{cyc} at 65% of the maximum shear stress produce uniform stress cycles that give an equivalent

increase in pore pressure to that of an irregular time history. (Kramer, 1996) This discovery led to the following equation by Seed and Idriss in 1971 (Kramer, 1996):

$$\tau_{cyc} = 0.65 \, (a_{max}/g) \, \sigma_v \, r_d$$

Where a_{max} is the peak ground surface acceleration, g is the acceleration due to gravity, σ_v is the total vertical stress, and r_d is the stress reduction factor at a depth of interest. (Kramer, 1996) The acceleration divided by the acceleration of gravity a_{max}/g (labeled a (g) in the results below) is calculated using the data from the WVDEP seismographs as follows (ISEE, 2011):

$$a = a_{max}/g = (2\pi f PPV)/386$$

Where f is the frequency in Hertz, PPV is the peak particle velocity in inches/second, and the constant 386 inches/second^2 is the acceleration due to gravity. (ISEE, 2011). The total vertical stress for each layer of interest is calculated in the results below using the following formula:

$$\sigma_v \text{ Layer} = \text{Depth x Specific Gravity x } 62.4$$

Where Depth is the depth of the layer of interest, Specific Gravity is the specific gravity of the material in the layer of interest, and 62.4 lbs/ft^{3}is the density of water. The total vertical stress at a depth of interest is calculated as follows:

$$\sigma_v \text{ Depth} = \sigma_v \text{ Layer} + \sigma_v \text{ Depth of next higher layer}$$

In the results below, an intermediary calculation τ_r is calculated as follows:

$$\tau_r = \sigma_v \text{ Depth x a}$$

The cyclic shear stress is then calculated as follows:

$$\tau_{cyc} = 0.65 \, \tau_r \, \sigma_v \, r_d$$

The stress reduction factor r_d is found using the average value from Seed and Idriss 1971 figure plotting the stress reduction factor versus the total depth of the point of interest.

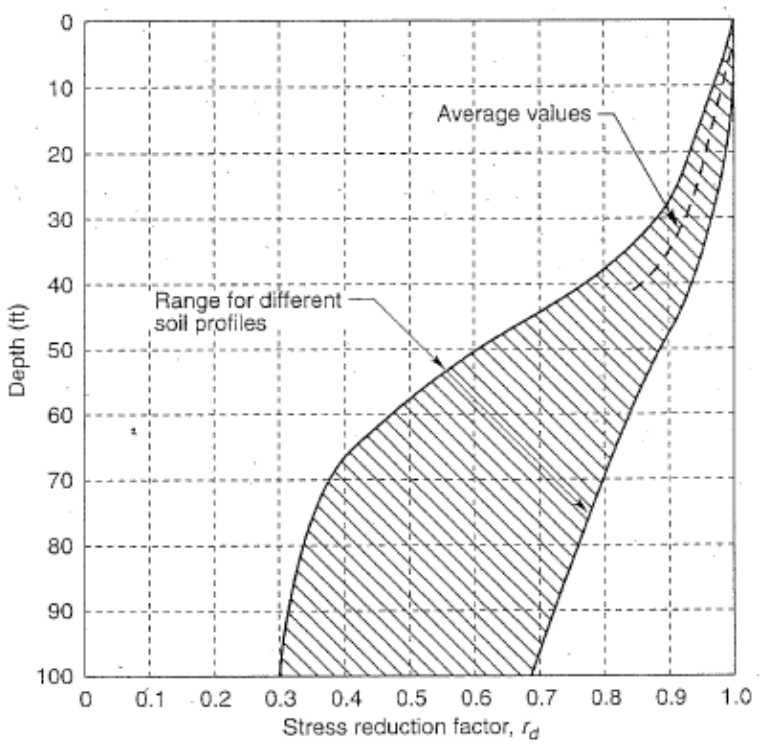

Figure 43: *Reduction factor to estimate the variation of cyclic shear stress with depth below gently sloping ground surfaces after Seed and Idriss 1971 (from Kramer, 1996)*

To normalize the cyclic stress for comparison with the cyclic stress resistance of the material, the total cyclic stress is divided by the effective vertical stress to produce a cyclic stress ratio (CSR). (Kramer, 1996) The CSR is calculated in the results below as follows:

$$CSR = \tau_{cyc}/(\sigma_v \text{ Depth} - (\text{Depth} \times 62.4))$$

The calculated values of CSR represent the loading due to blasting operations near an impoundment.

Due to the lack of access to the impoundment as mentioned above, it was not possible to collect adequate data to calculate the cyclic resistance of the coal fines in the instrumented impoundment. Therefore, in order to analyze the potential liquefaction of coal fines due to blasting, the cyclic resistance ratio results (CRR) in the Salehian dissertation for samples from the toe in the Big Branch impoundment were used. (Salehian, 2013) To ensure as much continuity to the analysis as possible, the toe samples were chosen because the location gave samples of only coal fines and not both coarse material and coal fines as found in the crest location. (Salehian, 2013) Furthermore, the properties of the fines and the various depths of the samples from the Big Branch site were used in the calculations of the CSR loading from

the blasts recorded by the WVDEP at the instrumented site. The CRR values are the threshold strengths of the coal fines at various depths of interest. A factor of safety in the results is calculated for each layer of fines as follows:

Factor of Safety = CRR/CSR

Any Factor of Safety above the value of 1.0 does not have liquefaction potential and a "NO" is entered for that layer in the Liquefy column of the results. Any Factor of Safety below the value of 1.0 does have liquefaction potential and a "YES" is entered for that layer in the Liquefy column.

The analyzed estimations are found in the figures below in the form of Excel Spreadsheet results. There are five spreadsheets, each showing results from a particular shot. At the upper left is a table that shows the calculation of acceleration in g's for each of the seismograph readings across the impoundment. Note the attenuation of peak particle velocity exhibited across the dam in the figure below.

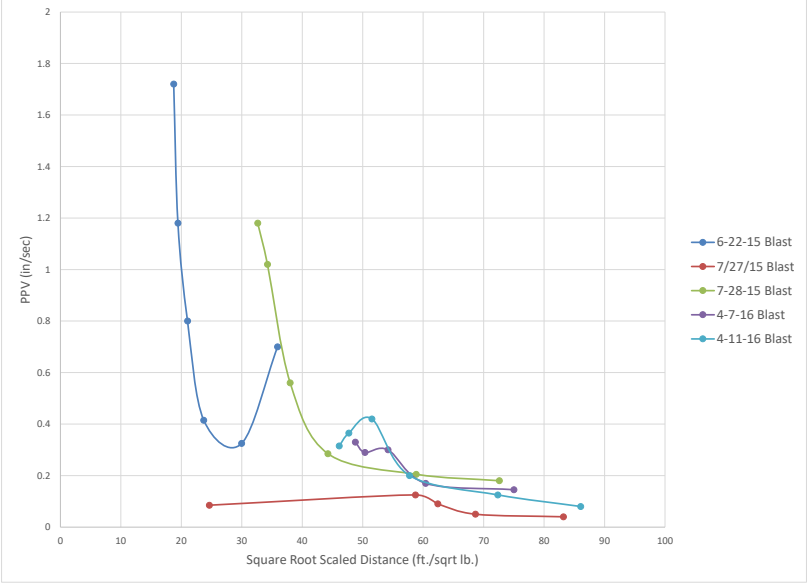

Figure 44: *Scaled distance versus peak particle velocity showing the attenuation of values across the impoundment (each point is a seismograph)*

The remaining columns are the various inputs and calculations mentioned above to calculate the CSR, CRR, and safety factor for each layer. Each figure has a table of calculated analysis for each of the seismograph readings across the dam. As noted in the last column of the results, the only liquefaction potential noted for all blasts is for the blast on June 22, 2015 at the 36.5 feet depth of interest. The PPV for Seismograph 1 on that shot was 1.72 inches per

second with a frequency of 8.4 hertz producing a factor of safety of 0.8814. It would appear that this would indicate that these values are close to a threshold values of blasting operations near impoundments except that seismograph 1 is located just on the solid off the edge of the impoundment and may not reflect the true values in the fines adjacent to this location. The values of CSR at this point may be less and thus under the calculated "threshold" due to reflection and refraction of the vibration waves by the interface between the solid material and the fines in the impoundment.

6/22/15 Blast

Seis	PPV (in/sec)	f (Hertz)	a (g)
Seis 1	1.72	8.3	0.23238
Seis 2	1.18	8.2	0.157503
Seis 3	0.8	3.1	0.040369
Seis 4	0.415	5.5	0.037154
Seis 5	0.35	7.6	0.043299

P_a (psf) 30.03 2124.58 psf

Seis 1

Total Depth (ft)	Sample	Depth (ft)	Specific Gravity	Total Unit Weight (pcf)	σ_v Layer (psf)	σ_v Depth (psf)	τ_r (psf)	r_d	τ_{cyc} (psf)	CSR	CRR	CRRa	Factor of Safety	Liquefy
36.5	TBBLAPST11S3	36.5	1.69	105.456	3849.144	3849.144	894.46	0.92	534.89	0.340	0.3	2.7567	0.881421	YES
55.3	TBBLAPST12S1	18.8	1.76	109.824	549.12	4398.264	1022.07	0.74	491.62	0.519	0.2	1.8378	0.385482	YES
76.7	TBBLAPST13S4	21.4	2.08	129.792	1297.92	5696.184	1323.68	0.60	516.24	0.567	0.28	2.57292	0.49363	YES
96.5	TBBLAPST14S3	19.8	2.47	154.128	1541.28	7237.464	1681.84	0.53	579.40	0.477	0.29	2.66481	0.608567	YES
97	TBBLAPST14S4	0.5	2.47	154.128	1541.28	8778.744	2040.01	0.52	689.52	0.253	0.26	2.38914	1.027879	NO
115.2	TBBLAPST15S1	18.2	1.92	119.808	1198.08	9976.824	2318.42	0.50	753.49	0.270	0.24	2.20536	0.888143	YES
115.8	TBBLAPST15S2	0.6	1.92	119.808	1198.08	11174.9	2596.83	0.50	843.97	0.214	0.34	3.12426	1.590882	NO
116.4	TBBLAPST15S3	0.6	1.92	119.808	1198.08	12372.98	2875.24	0.50	934.45	0.183	0.28	2.57292	1.531052	NO
135.3	TBBLAPST16S1	18.9	2.16	134.784	1347.84	13720.82	3188.45	0.50	1036.25	0.196	0.43	3.95127	2.1902	NO
136	TBBLAPST16S2	0.7	2.16	134.784	1347.84	15068.66	3501.66	0.50	1138.04	0.173	0.34	3.12426	1.966514	NO

Seis 2

Total Depth (ft)	Sample	Depth (ft)	Specific Gravity	Total Unit Weight (pcf)	σ_v Layer (psf)	σ_v Depth (psf)	τ_r (psf)	r_d	τ_{cyc} (psf)	CSR	CRR	CRRa	Factor of Safety	Liquefy
36.5	TBBLAPST11S3	36.5	1.69	105.456	3849.144	3849.144	606.25	0.92	362.54	0.231	0.3	2.7567	1.300451	NO
55.3	TBBLAPST12S1	18.8	1.76	109.824	549.12	4398.264	692.74	0.74	333.21	0.352	0.2	1.8378	0.568741	YES
76.7	TBBLAPST13S4	21.4	2.08	129.792	1297.92	5696.184	897.17	0.60	349.89	0.384	0.28	2.57292	0.728303	YES
96.5	TBBLAPST14S3	19.8	2.47	154.128	1541.28	7237.464	1139.92	0.53	392.70	0.323	0.29	2.66481	0.897881	YES
97	TBBLAPST14S4	0.5	2.47	154.128	1541.28	8778.744	1382.68	0.52	467.34	0.171	0.26	2.38914	1.516536	NO
115.2	TBBLAPST15S1	18.2	1.92	119.808	1198.08	9976.824	1571.38	0.50	510.70	0.183	0.24	2.20536	1.310369	NO
115.8	TBBLAPST15S2	0.6	1.92	119.808	1198.08	11174.9	1760.08	0.50	572.03	0.145	0.34	3.12426	2.347192	NO
116.4	TBBLAPST15S3	0.6	1.92	119.808	1198.08	12372.98	1948.78	0.50	633.35	0.124	0.28	2.57292	2.258919	NO
135.3	TBBLAPST16S1	18.9	2.16	134.784	1347.84	13720.82	2161.07	0.50	702.35	0.133	0.43	3.95127	3.231428	NO
136	TBBLAPST16S2	0.7	2.16	134.784	1347.84	15068.66	2373.36	0.50	771.34	0.117	0.34	3.12426	2.9014	NO

Seis 3

Total Depth (ft)	Sample	Depth (ft)	Specific Gravity	Total Unit Weight (pcf)	σ_v Layer (psf)	σ_v Depth (psf)	τ_r (psf)	r_d	τ_{cyc} (psf)	CSR	CRR	CRRa	Factor of Safety	Liquefy
36.5	TBBLAPST11S3	36.5	1.69	105.456	3849.144	3849.144	155.38	0.92	92.92	0.059	0.3	2.7567	5.073857	NO
55.3	TBBLAPST12S1	18.8	1.76	109.824	549.12	4398.264	177.55	0.74	85.40	0.090	0.2	1.8378	2.219007	NO
76.7	TBBLAPST13S4	21.4	2.08	129.792	1297.92	5696.184	229.95	0.60	89.68	0.099	0.28	2.57292	2.841556	NO
96.5	TBBLAPST14S3	19.8	2.47	154.128	1541.28	7237.464	292.17	0.53	100.65	0.083	0.29	2.66481	3.503185	NO
97	TBBLAPST14S4	0.5	2.47	154.128	1541.28	8778.744	354.39	0.52	119.78	0.044	0.26	2.38914	5.916937	NO
115.2	TBBLAPST15S1	18.2	1.92	119.808	1198.08	9976.824	402.75	0.50	130.89	0.047	0.24	2.20536	5.112551	NO
115.8	TBBLAPST15S2	0.6	1.92	119.808	1198.08	11174.9	451.12	0.50	146.61	0.037	0.34	3.12426	9.157836	NO
116.4	TBBLAPST15S3	0.6	1.92	119.808	1198.08	12372.98	499.48	0.50	162.33	0.032	0.28	2.57292	8.813429	NO
135.3	TBBLAPST16S1	18.9	2.16	134.784	1347.84	13720.82	553.89	0.50	180.01	0.034	0.43	3.95127	12.60778	NO
136	TBBLAPST16S2	0.7	2.16	134.784	1347.84	15068.66	608.30	0.50	197.70	0.030	0.34	3.12426	11.32014	NO

Seis 4

Total Depth (ft)	Sample	Depth (ft)	Specific Gravity	Total Unit Weight (pcf)	σ_v Layer (psf)	σ_v Depth (psf)	τ_r (psf)	r_d	τ_{cyc} (psf)	CSR	CRR	CRRa	Factor of Safety	Liquefy
36.5	TBBLAPST11S3	36.5	1.69	105.456	3849.144	3849.144	143.01	0.92	85.52	0.054	0.3	2.7567	5.512887	NO
55.3	TBBLAPST12S1	18.8	1.76	109.824	549.12	4398.264	163.41	0.74	78.60	0.083	0.2	1.8378	2.411014	NO
76.7	TBBLAPST13S4	21.4	2.08	129.792	1297.92	5696.184	211.63	0.60	82.54	0.091	0.28	2.57292	3.08743	NO
96.5	TBBLAPST14S3	19.8	2.47	154.128	1541.28	7237.464	268.90	0.53	92.64	0.076	0.29	2.66481	3.806309	NO
97	TBBLAPST14S4	0.5	2.47	154.128	1541.28	8778.744	326.16	0.52	110.24	0.040	0.26	2.38914	6.428917	NO
115.2	TBBLAPST15S1	18.2	1.92	119.808	1198.08	9976.824	370.68	0.50	120.47	0.043	0.24	2.20536	5.55493	NO
115.8	TBBLAPST15S2	0.6	1.92	119.808	1198.08	11174.9	415.19	0.50	134.94	0.034	0.34	3.12426	9.950245	NO
116.4	TBBLAPST15S3	0.6	1.92	119.808	1198.08	12372.98	459.70	0.50	149.40	0.029	0.28	2.57292	9.576037	NO
135.3	TBBLAPST16S1	18.9	2.16	134.784	1347.84	13720.82	509.78	0.50	165.68	0.031	0.43	3.95127	13.6987	NO
136	TBBLAPST16S2	0.7	2.16	134.784	1347.84	15068.66	559.86	0.50	181.95	0.028	0.34	3.12426	12.29965	NO

Seis 5

Total Depth (ft)	Sample	Depth (ft)	Specific Gravity	Total Unit Weight (pcf)	σ_v Layer (psf)	σ_v Depth (psf)	τ_r (psf)	r_d	τ_{cyc} (psf)	CSR	CRR	CRRa	Factor of Safety	Liquefy
36.5	TBBLAPST11S3	36.5	1.69	105.456	3849.144	3849.144	166.66	0.92	99.66	0.063	0.3	2.7567	43.46869	NO
55.3	TBBLAPST12S1	18.8	1.76	109.824	549.12	4398.264	190.44	0.74	91.60	0.097	0.2	1.8378	19.01065	NO
76.7	TBBLAPST13S4	21.4	2.08	129.792	1297.92	5696.184	246.64	0.60	96.19	0.106	0.28	2.57292	24.34414	NO
96.5	TBBLAPST14S3	19.8	2.47	154.128	1541.28	7237.464	313.37	0.53	107.96	0.089	0.29	2.66481	30.01245	NO
97	TBBLAPST14S4	0.5	2.47	154.128	1541.28	8778.744	380.11	0.52	128.48	0.047	0.26	2.38914	50.69151	NO
115.2	TBBLAPST15S1	18.2	1.92	119.808	1198.08	9976.824	431.98	0.50	140.39	0.050	0.24	2.20536	43.80019	NO
115.8	TBBLAPST15S2	0.6	1.92	119.808	1198.08	11174.9	483.86	0.50	157.25	0.040	0.34	3.12426	78.45691	NO
116.4	TBBLAPST15S3	0.6	1.92	119.808	1198.08	12372.98	535.73	0.50	174.11	0.034	0.28	2.57292	75.5063	NO
135.3	TBBLAPST16S1	18.9	2.16	134.784	1347.84	13720.82	594.09	0.50	193.08	0.037	0.43	3.95127	108.0132	NO
136	TBBLAPST16S2	0.7	2.16	134.784	1347.84	15068.66	652.45	0.50	212.05	0.032	0.34	3.12426	96.98178	NO

Figure 45: *Liquefaction potential analysis for the June 22, 2015 blast*

7/27/15 Blast

Seis	PPV (in/sec)	f (Hertz)	a (g)
Seis 1	0.085	10	0.013836
Seis 2	0.125	8.6	0.017499
Seis 3	0.09	7.4	0.010841
Seis 4	0.05	9.4	0.007651
Seis 5	0.04	12.8	0.008334

P_a (psf) 30.03 2124.58 psf

Seis 1

Total Depth (ft)	Sample	Depth (ft)	Specific Gravity	Total Unit Weight (pcf)	σ_v Layer (psf)	σ_v Depth (psf)	τ_r (psf)	r_d	τ_{cyc} (psf)	CSR	CRR	Factor of Safety	Liquefy
36.5	TBBLAPST11S3	36.5	1.69	105.456	3849.144	3849.144	53.26	0.92	31.85	0.020	0.3	14.80372	NO
55.3	TBBLAPST12S1	18.8	1.76	109.824	549.12	4398.264	60.85	0.74	29.27	0.031	0.2	6.474281	NO
76.7	TBBLAPST13S4	21.4	2.08	129.792	1297.92	5696.184	78.81	0.60	30.74	0.034	0.28	8.290657	NO
96.5	TBBLAPST14S3	19.8	2.47	154.128	1541.28	7237.464	100.14	0.53	34.50	0.028	0.29	10.22106	NO
97	TBBLAPST14S4	0.5	2.47	154.128	1541.28	8778.744	121.46	0.52	41.05	0.015	0.26	17.26353	NO
115.2	TBBLAPST15S1	18.2	1.92	119.808	1198.08	9976.824	138.04	0.50	44.86	0.016	0.24	14.91662	NO
115.8	TBBLAPST15S2	0.6	1.92	119.808	1198.08	11174.9	154.62	0.50	50.25	0.013	0.34	26.71933	NO
116.4	TBBLAPST15S3	0.6	1.92	119.808	1198.08	12372.98	171.19	0.50	55.64	0.011	0.28	25.71448	NO
135.3	TBBLAPST16S1	18.9	2.16	134.784	1347.84	13720.82	189.84	0.50	61.70	0.012	0.43	36.78505	NO
136	TBBLAPST16S2	0.7	2.16	134.784	1347.84	15068.66	208.49	0.50	67.76	0.010	0.34	33.02818	NO

Seis 2

Total Depth (ft)	Sample	Depth (ft)	Specific Gravity	Total Unit Weight (pcf)	σ_v Layer (psf)	σ_v Depth (psf)	τ_r (psf)	r_d	τ_{cyc} (psf)	CSR	CRR	Factor of Safety	Liquefy
36.5	TBBLAPST11S3	36.5	1.69	105.456	3849.144	3849.144	67.35	0.92	40.28	0.026	0.3	11.70527	NO
55.3	TBBLAPST12S1	18.8	1.76	109.824	549.12	4398.264	76.96	0.74	37.02	0.039	0.2	5.119199	NO
76.7	TBBLAPST13S4	21.4	2.08	129.792	1297.92	5696.184	99.67	0.60	38.87	0.043	0.28	6.555403	NO
96.5	TBBLAPST14S3	19.8	2.47	154.128	1541.28	7237.464	126.64	0.53	43.63	0.036	0.29	8.081767	NO
97	TBBLAPST14S4	0.5	2.47	154.128	1541.28	8778.744	153.61	0.52	51.92	0.019	0.26	13.65024	NO
115.2	TBBLAPST15S1	18.2	1.92	119.808	1198.08	9976.824	174.58	0.50	56.74	0.020	0.24	11.79454	NO
115.8	TBBLAPST15S2	0.6	1.92	119.808	1198.08	11174.9	195.54	0.50	63.55	0.016	0.34	21.12692	NO
116.4	TBBLAPST15S3	0.6	1.92	119.808	1198.08	12372.98	216.51	0.50	70.37	0.014	0.28	20.33238	NO
135.3	TBBLAPST16S1	18.9	2.16	134.784	1347.84	13720.82	240.09	0.50	78.03	0.015	0.43	29.08585	NO
136	TBBLAPST16S2	0.7	2.16	134.784	1347.84	15068.66	263.68	0.50	85.70	0.013	0.34	26.1153	NO

Seis 3

Total Depth (ft)	Sample	Depth (ft)	Specific Gravity	Total Unit Weight (pcf)	σ_v Layer (psf)	σ_v Depth (psf)	τ_r (psf)	r_d	τ_{cyc} (psf)	CSR	CRR	Factor of Safety	Liquefy
36.5	TBBLAPST11S3	36.5	1.69	105.456	3849.144	3849.144	41.73	0.92	24.95	0.016	0.3	18.89364	NO
55.3	TBBLAPST12S1	18.8	1.76	109.824	549.12	4398.264	47.68	0.74	22.93	0.024	0.2	8.262971	NO
76.7	TBBLAPST13S4	21.4	2.08	129.792	1297.92	5696.184	61.75	0.60	24.08	0.026	0.28	10.58117	NO
96.5	TBBLAPST14S3	19.8	2.47	154.128	1541.28	7237.464	78.46	0.53	27.03	0.022	0.29	13.04489	NO
97	TBBLAPST14S4	0.5	2.47	154.128	1541.28	8778.744	95.17	0.52	32.17	0.012	0.26	22.03304	NO
115.2	TBBLAPST15S1	18.2	1.92	119.808	1198.08	9976.824	108.16	0.50	35.15	0.013	0.24	19.03773	NO
115.8	TBBLAPST15S2	0.6	1.92	119.808	1198.08	11174.9	121.15	0.50	39.37	0.010	0.34	34.10125	NO
116.4	TBBLAPST15S3	0.6	1.92	119.808	1198.08	12372.98	134.13	0.50	43.59	0.009	0.28	32.81878	NO
135.3	TBBLAPST16S1	18.9	2.16	134.784	1347.84	13720.82	148.75	0.50	48.34	0.009	0.43	46.94789	NO
136	TBBLAPST16S2	0.7	2.16	134.784	1347.84	15068.66	163.36	0.50	53.09	0.008	0.34	42.15308	NO

Seis 4

Total Depth (ft)	Sample	Depth (ft)	Specific Gravity	Total Unit Weight (pcf)	σ_v Layer (psf)	σ_v Depth (psf)	τ_r (psf)	r_d	τ_{cyc} (psf)	CSR	CRR	Factor of Safety	Liquefy
36.5	TBBLAPST11S3	36.5	1.69	105.456	3849.144	3849.144	29.45	0.92	17.61	0.011	0.3	26.77269	NO
55.3	TBBLAPST12S1	18.8	1.76	109.824	549.12	4398.264	33.65	0.74	16.19	0.017	0.2	11.70881	NO
76.7	TBBLAPST13S4	21.4	2.08	129.792	1297.92	5696.184	43.58	0.60	17.00	0.019	0.28	14.99374	NO
96.5	TBBLAPST14S3	19.8	2.47	154.128	1541.28	7237.464	55.37	0.53	19.08	0.016	0.29	18.48489	NO
97	TBBLAPST14S4	0.5	2.47	154.128	1541.28	8778.744	67.16	0.52	22.70	0.008	0.26	31.22128	NO
115.2	TBBLAPST15S1	18.2	1.92	119.808	1198.08	9976.824	76.33	0.50	24.81	0.009	0.24	26.97687	NO
115.8	TBBLAPST15S2	0.6	1.92	119.808	1198.08	11174.9	85.49	0.50	27.79	0.007	0.34	48.3222	NO
116.4	TBBLAPST15S3	0.6	1.92	119.808	1198.08	12372.98	94.66	0.50	30.76	0.006	0.28	46.5049	NO
135.3	TBBLAPST16S1	18.9	2.16	134.784	1347.84	13720.82	104.97	0.50	34.12	0.006	0.43	66.52615	NO
136	TBBLAPST16S2	0.7	2.16	134.784	1347.84	15068.66	115.28	0.50	37.47	0.006	0.34	59.73181	NO

Seis 5

Total Depth (ft)	Sample	Depth (ft)	Specific Gravity	Total Unit Weight (pcf)	σ_v Layer (psf)	σ_v Depth (psf)	τ_r (psf)	r_d	τ_{cyc} (psf)	CSR	CRR	Factor of Safety	Liquefy
36.5	TBBLAPST11S3	36.5	1.69	105.456	3849.144	3849.144	32.08	0.92	19.18	0.012	0.3	24.57649	NO
55.3	TBBLAPST12S1	18.8	1.76	109.824	549.12	4398.264	36.66	0.74	17.63	0.019	0.2	10.74832	NO
76.7	TBBLAPST13S4	21.4	2.08	129.792	1297.92	5696.184	47.47	0.60	18.51	0.020	0.28	13.76379	NO
96.5	TBBLAPST14S3	19.8	2.47	154.128	1541.28	7237.464	60.32	0.53	20.78	0.017	0.29	16.96855	NO
97	TBBLAPST14S4	0.5	2.47	154.128	1541.28	8778.744	73.16	0.52	24.73	0.009	0.26	28.66016	NO
115.2	TBBLAPST15S1	18.2	1.92	119.808	1198.08	9976.824	83.15	0.50	27.02	0.010	0.24	24.76392	NO
115.8	TBBLAPST15S2	0.6	1.92	119.808	1198.08	11174.9	93.13	0.50	30.27	0.008	0.34	44.35827	NO
116.4	TBBLAPST15S3	0.6	1.92	119.808	1198.08	12372.98	103.12	0.50	33.51	0.007	0.28	42.69005	NO
135.3	TBBLAPST16S1	18.9	2.16	134.784	1347.84	13720.82	114.35	0.50	37.16	0.007	0.43	61.06893	NO
136	TBBLAPST16S2	0.7	2.16	134.784	1347.84	15068.66	125.58	0.50	40.82	0.006	0.34	54.83194	NO

Figure 46: *Liquefaction potential analysis for the July 27, 2015 blast*

7/28/15 Blast

Seis	PPV (in/sec)	f (Hertz)	a (g)
Seis 1	1.18	9.8	0.188235
Seis 2	1.02	10.2	0.169353
Seis 3	0.56	9.4	0.085686
Seis 4	0.285	5.8	0.026907
Seis 5	0.205	3	0.010011

P_a (psf) 30.03 2124.58 psf

Seis 1

Total Depth (ft)	Sample	Depth (ft)	Specific Gravity	Total Unit Weight (pcf)	σ_v Layer (psf)	σ_v Depth (psf)	τ_r (psf)	r_d	τ_{cyc} (psf)	CSR	CRR	Factor of Safety	Liquefy
36.5	TBBLAPST11S3	36.5	1.69	105.456	3849.144	3849.144	724.54	0.92	433.28	0.276	0.3	1.088133	NO
55.3	TBBLAPST12S1	18.8	1.76	109.824	549.12	4398.264	827.91	0.74	398.22	0.420	0.2	0.475885	YES
76.7	TBBLAPST13S4	21.4	2.08	129.792	1297.92	5696.184	1072.22	0.60	418.17	0.459	0.28	0.609396	YES
96.5	TBBLAPST14S3	19.8	2.47	154.128	1541.28	7237.464	1362.34	0.53	469.33	0.386	0.29	0.751288	YES
97	TBBLAPST14S4	0.5	2.47	154.128	1541.28	8778.744	1652.47	0.52	558.53	0.205	0.26	1.268938	NO
115.2	TBBLAPST15S1	18.2	1.92	119.808	1198.08	9976.824	1877.99	0.50	610.35	0.219	0.24	1.096431	NO
115.8	TBBLAPST15S2	0.6	1.92	119.808	1198.08	11174.9	2103.51	0.50	683.64	0.173	0.34	1.963977	NO
116.4	TBBLAPST15S3	0.6	1.92	119.808	1198.08	12372.98	2329.03	0.50	756.93	0.148	0.28	1.890116	NO
135.3	TBBLAPST16S1	18.9	2.16	134.784	1347.84	13720.82	2582.74	0.50	839.39	0.159	0.43	2.703848	NO
136	TBBLAPST16S2	0.7	2.16	134.784	1347.84	15068.66	2836.45	0.50	921.85	0.140	0.34	2.427702	NO

Seis 2

Total Depth (ft)	Sample	Depth (ft)	Specific Gravity	Total Unit Weight (pcf)	σ_v Layer (psf)	σ_v Depth (psf)	τ_r (psf)	r_d	τ_{cyc} (psf)	CSR	CRR	Factor of Safety	Liquefy
36.5	TBBLAPST11S3	36.5	1.69	105.456	3849.144	3849.144	651.86	0.92	389.81	0.248	0.3	1.209455	NO
55.3	TBBLAPST12S1	18.8	1.76	109.824	549.12	4398.264	744.86	0.74	358.28	0.378	0.2	0.528944	YES
76.7	TBBLAPST13S4	21.4	2.08	129.792	1297.92	5696.184	964.67	0.60	376.22	0.413	0.28	0.677341	YES
96.5	TBBLAPST14S3	19.8	2.47	154.128	1541.28	7237.464	1225.69	0.53	422.25	0.347	0.29	0.835054	YES
97	TBBLAPST14S4	0.5	2.47	154.128	1541.28	8778.744	1486.71	0.52	502.51	0.184	0.26	1.410419	NO
115.2	TBBLAPST15S1	18.2	1.92	119.808	1198.08	9976.824	1689.61	0.50	549.12	0.197	0.24	1.218678	NO
115.8	TBBLAPST15S2	0.6	1.92	119.808	1198.08	11174.9	1892.50	0.50	615.06	0.156	0.34	2.182952	NO
116.4	TBBLAPST15S3	0.6	1.92	119.808	1198.08	12372.98	2095.40	0.50	681.01	0.133	0.28	2.100856	NO
135.3	TBBLAPST16S1	18.9	2.16	134.784	1347.84	13720.82	2323.66	0.50	755.19	0.143	0.43	3.005315	NO
136	TBBLAPST16S2	0.7	2.16	134.784	1347.84	15068.66	2551.92	0.50	829.38	0.126	0.34	2.698381	NO

Seis 3

Total Depth (ft)	Sample	Depth (ft)	Specific Gravity	Total Unit Weight (pcf)	σ_v Layer (psf)	σ_v Depth (psf)	τ_r (psf)	r_d	τ_{cyc} (psf)	CSR	CRR	Factor of Safety	Liquefy
36.5	TBBLAPST11S3	36.5	1.69	105.456	3849.144	3849.144	329.82	0.92	197.23	0.126	0.3	2.390419	NO
55.3	TBBLAPST12S1	18.8	1.76	109.824	549.12	4398.264	376.87	0.74	181.27	0.191	0.2	1.045429	NO
76.7	TBBLAPST13S4	21.4	2.08	129.792	1297.92	5696.184	488.08	0.60	190.35	0.209	0.28	1.338727	NO
96.5	TBBLAPST14S3	19.8	2.47	154.128	1541.28	7237.464	620.15	0.53	213.64	0.176	0.29	1.650437	NO
97	TBBLAPST14S4	0.5	2.47	154.128	1541.28	8778.744	752.21	0.52	254.25	0.093	0.26	2.787615	NO
115.2	TBBLAPST15S1	18.2	1.92	119.808	1198.08	9976.824	854.87	0.50	277.83	0.100	0.24	2.408649	NO
115.8	TBBLAPST15S2	0.6	1.92	119.808	1198.08	11174.9	957.53	0.50	311.20	0.079	0.34	4.314482	NO
116.4	TBBLAPST15S3	0.6	1.92	119.808	1198.08	12372.98	1060.19	0.50	344.56	0.067	0.28	4.152223	NO
135.3	TBBLAPST16S1	18.9	2.16	134.784	1347.84	13720.82	1175.68	0.50	382.10	0.072	0.43	5.939835	NO
136	TBBLAPST16S2	0.7	2.16	134.784	1347.84	15068.66	1291.17	0.50	419.63	0.064	0.34	5.333197	NO

Seis 4

Total Depth (ft)	Sample	Depth (ft)	Specific Gravity	Total Unit Weight (pcf)	σ_v Layer (psf)	σ_v Depth (psf)	τ_r (psf)	r_d	τ_{cyc} (psf)	CSR	CRR	Factor of Safety	Liquefy
36.5	TBBLAPST11S3	36.5	1.69	105.456	3849.144	3849.144	103.57	0.92	61.93	0.039	0.3	7.61232	NO
55.3	TBBLAPST12S1	18.8	1.76	109.824	549.12	4398.264	118.34	0.74	56.92	0.060	0.2	3.329182	NO
76.7	TBBLAPST13S4	21.4	2.08	129.792	1297.92	5696.184	153.27	0.60	59.77	0.066	0.28	4.263193	NO
96.5	TBBLAPST14S3	19.8	2.47	154.128	1541.28	7237.464	194.74	0.53	67.09	0.055	0.29	5.255838	NO
97	TBBLAPST14S4	0.5	2.47	154.128	1541.28	8778.744	236.21	0.52	79.84	0.029	0.26	8.877195	NO
115.2	TBBLAPST15S1	18.2	1.92	119.808	1198.08	9976.824	268.45	0.50	87.25	0.031	0.24	7.670373	NO
115.8	TBBLAPST15S2	0.6	1.92	119.808	1198.08	11174.9	300.68	0.50	97.72	0.025	0.34	13.73952	NO
116.4	TBBLAPST15S3	0.6	1.92	119.808	1198.08	12372.98	332.92	0.50	108.20	0.021	0.28	13.22281	NO
135.3	TBBLAPST16S1	18.9	2.16	134.784	1347.84	13720.82	369.19	0.50	119.99	0.023	0.43	18.91548	NO
136	TBBLAPST16S2	0.7	2.16	134.784	1347.84	15068.66	405.45	0.50	131.77	0.020	0.34	16.98364	NO

Seis 5

Total Depth (ft)	Sample	Depth (ft)	Specific Gravity	Total Unit Weight (pcf)	σ_v Layer (psf)	σ_v Depth (psf)	τ_r (psf)	r_d	τ_{cyc} (psf)	CSR	CRR	Factor of Safety	Liquefy
36.5	TBBLAPST11S3	36.5	1.69	105.456	3849.144	3849.144	38.53	0.92	23.04	0.015	0.3	20.46043	NO
55.3	TBBLAPST12S1	18.8	1.76	109.824	549.12	4398.264	44.03	0.74	21.18	0.022	0.2	8.948193	NO
76.7	TBBLAPST13S4	21.4	2.08	129.792	1297.92	5696.184	57.02	0.60	22.24	0.024	0.28	11.45863	NO
96.5	TBBLAPST14S3	19.8	2.47	154.128	1541.28	7237.464	72.45	0.53	24.96	0.021	0.29	14.12667	NO
97	TBBLAPST14S4	0.5	2.47	154.128	1541.28	8778.744	87.88	0.52	29.70	0.011	0.26	23.86017	NO
115.2	TBBLAPST15S1	18.2	1.92	119.808	1198.08	9976.824	99.88	0.50	32.46	0.012	0.24	20.61647	NO
115.8	TBBLAPST15S2	0.6	1.92	119.808	1198.08	11174.9	111.87	0.50	36.36	0.009	0.34	36.92916	NO
116.4	TBBLAPST15S3	0.6	1.92	119.808	1198.08	12372.98	123.86	0.50	40.26	0.008	0.28	35.54033	NO
135.3	TBBLAPST16S1	18.9	2.16	134.784	1347.84	13720.82	137.36	0.50	44.64	0.008	0.43	50.84113	NO
136	TBBLAPST16S2	0.7	2.16	134.784	1347.84	15068.66	150.85	0.50	49.03	0.007	0.34	45.6487	NO

Figure 47: *Liquefaction potential analysis for the July 28, 2015 blast*

4/7/16 Blast

Seis	PPV (in/sec)	f (Hertz)	a (g)
Seis 1	0.33	6.9	0.037064
Seis 2	0.29	7.7	0.036348
Seis 3	0.3	5.1	0.024905
Seis 4	0.17	5.6	0.015496
Seis 5	0.145	6	0.014162

P_a (psf) 30.03 2124.58 psf

Seis 1

Total Depth (ft)	Sample	Depth (ft)	Specific Gravity	Total Unit Weight (pcf)	σ_v Layer (psf)	σ_v Depth (psf)	τ_r (psf)	r_d	τ_{cyc} (psf)	CSR	CRR	Factor of Safety	Liquefy
36.5	TBBLAPST11S3	36.5	1.69	105.456	3849.144	3849.144	142.67	0.92	85.31	0.054	0.3	5.526203	NO
55.3	TBBLAPST12S1	18.8	1.76	109.824	549.12	4398.264	163.02	0.74	78.41	0.083	0.2	2.416837	NO
76.7	TBBLAPST13S4	21.4	2.08	129.792	1297.92	5696.184	211.12	0.60	82.34	0.090	0.28	3.094887	NO
96.5	TBBLAPST14S3	19.8	2.47	154.128	1541.28	7237.464	268.25	0.53	92.41	0.076	0.29	3.815503	NO
97	TBBLAPST14S4	0.5	2.47	154.128	1541.28	8778.744	325.38	0.52	109.98	0.040	0.26	6.444446	NO
115.2	TBBLAPST15S1	18.2	1.92	119.808	1198.08	9976.824	369.78	0.50	120.18	0.043	0.24	5.568347	NO
115.8	TBBLAPST15S2	0.6	1.92	119.808	1198.08	11174.9	414.19	0.50	134.61	0.034	0.34	9.97428	NO
116.4	TBBLAPST15S3	0.6	1.92	119.808	1198.08	12372.98	458.60	0.50	149.04	0.029	0.28	9.599167	NO
135.3	TBBLAPST16S1	18.9	2.16	134.784	1347.84	13720.82	508.55	0.50	165.28	0.031	0.43	13.73179	NO
136	TBBLAPST16S2	0.7	2.16	134.784	1347.84	15068.66	558.51	0.50	181.52	0.028	0.34	12.32936	NO

Seis 2

Total Depth (ft)	Sample	Depth (ft)	Specific Gravity	Total Unit Weight (pcf)	σ_v Layer (psf)	σ_v Depth (psf)	τ_r (psf)	r_d	τ_{cyc} (psf)	CSR	CRR	Factor of Safety	Liquefy
36.5	TBBLAPST11S3	36.5	1.69	105.456	3849.144	3849.144	139.91	0.92	83.67	0.053	0.3	5.635094	NO
55.3	TBBLAPST12S1	18.8	1.76	109.824	549.12	4398.264	159.87	0.74	76.90	0.081	0.2	2.46446	NO
76.7	TBBLAPST13S4	21.4	2.08	129.792	1297.92	5696.184	207.05	0.60	80.75	0.089	0.28	3.15587	NO
96.5	TBBLAPST14S3	19.8	2.47	154.128	1541.28	7237.464	263.07	0.53	90.63	0.075	0.29	3.890685	NO
97	TBBLAPST14S4	0.5	2.47	154.128	1541.28	8778.744	319.09	0.52	107.85	0.040	0.26	6.57143	NO
115.2	TBBLAPST15S1	18.2	1.92	119.808	1198.08	9976.824	362.64	0.50	117.86	0.042	0.24	5.678069	NO
115.8	TBBLAPST15S2	0.6	1.92	119.808	1198.08	11174.9	406.19	0.50	132.01	0.033	0.34	10.17082	NO
116.4	TBBLAPST15S3	0.6	1.92	119.808	1198.08	12372.98	449.73	0.50	146.16	0.029	0.28	9.788314	NO
135.3	TBBLAPST16S1	18.9	2.16	134.784	1347.84	13720.82	498.73	0.50	162.09	0.031	0.43	14.00237	NO
136	TBBLAPST16S2	0.7	2.16	134.784	1347.84	15068.66	547.72	0.50	178.01	0.027	0.34	12.5723	NO

Seis 3

Total Depth (ft)	Sample	Depth (ft)	Specific Gravity	Total Unit Weight (pcf)	σ_v Layer (psf)	σ_v Depth (psf)	τ_r (psf)	r_d	τ_{cyc} (psf)	CSR	CRR	Factor of Safety	Liquefy
36.5	TBBLAPST11S3	36.5	1.69	105.456	3849.144	3849.144	95.86	0.92	57.33	0.036	0.3	8.224291	NO
55.3	TBBLAPST12S1	18.8	1.76	109.824	549.12	4398.264	109.54	0.74	52.69	0.056	0.2	3.596823	NO
76.7	TBBLAPST13S4	21.4	2.08	129.792	1297.92	5696.184	141.86	0.60	55.33	0.061	0.28	4.605921	NO
96.5	TBBLAPST14S3	19.8	2.47	154.128	1541.28	7237.464	180.25	0.53	62.10	0.051	0.29	5.678366	NO
97	TBBLAPST14S4	0.5	2.47	154.128	1541.28	8778.744	218.63	0.52	73.90	0.027	0.26	9.590852	NO
115.2	TBBLAPST15S1	18.2	1.92	119.808	1198.08	9976.824	248.47	0.50	80.75	0.029	0.24	8.287011	NO
115.8	TBBLAPST15S2	0.6	1.92	119.808	1198.08	11174.9	278.31	0.50	90.45	0.023	0.34	14.84407	NO
116.4	TBBLAPST15S3	0.6	1.92	119.808	1198.08	12372.98	308.15	0.50	100.15	0.020	0.28	14.28582	NO
135.3	TBBLAPST16S1	18.9	2.16	134.784	1347.84	13720.82	341.72	0.50	111.06	0.021	0.43	20.43614	NO
136	TBBLAPST16S2	0.7	2.16	134.784	1347.84	15068.66	375.28	0.50	121.97	0.019	0.34	18.34899	NO

Seis 4

Total Depth (ft)	Sample	Depth (ft)	Specific Gravity	Total Unit Weight (pcf)	σ_v Layer (psf)	σ_v Depth (psf)	τ_r (psf)	r_d	τ_{cyc} (psf)	CSR	CRR	Factor of Safety	Liquefy
36.5	TBBLAPST11S3	36.5	1.69	105.456	3849.144	3849.144	59.65	0.92	35.67	0.023	0.3	13.21761	NO
55.3	TBBLAPST12S1	18.8	1.76	109.824	549.12	4398.264	68.16	0.74	32.78	0.035	0.2	5.780608	NO
76.7	TBBLAPST13S4	21.4	2.08	129.792	1297.92	5696.184	88.27	0.60	34.43	0.038	0.28	7.402372	NO
96.5	TBBLAPST14S3	19.8	2.47	154.128	1541.28	7237.464	112.15	0.53	38.64	0.032	0.29	9.125945	NO
97	TBBLAPST14S4	0.5	2.47	154.128	1541.28	8778.744	136.04	0.52	45.98	0.017	0.26	15.41387	NO
115.2	TBBLAPST15S1	18.2	1.92	119.808	1198.08	9976.824	154.60	0.50	50.25	0.018	0.24	13.31841	NO
115.8	TBBLAPST15S2	0.6	1.92	119.808	1198.08	11174.9	173.17	0.50	56.28	0.014	0.34	23.85655	NO
116.4	TBBLAPST15S3	0.6	1.92	119.808	1198.08	12372.98	191.74	0.50	62.31	0.012	0.28	22.95935	NO
135.3	TBBLAPST16S1	18.9	2.16	134.784	1347.84	13720.82	212.62	0.50	69.10	0.013	0.43	32.84379	NO
136	TBBLAPST16S2	0.7	2.16	134.784	1347.84	15068.66	233.51	0.50	75.89	0.012	0.34	29.48944	NO

Seis 5

Total Depth (ft)	Sample	Depth (ft)	Specific Gravity	Total Unit Weight (pcf)	σ_v Layer (psf)	σ_v Depth (psf)	τ_r (psf)	r_d	τ_{cyc} (psf)	CSR	CRR	Factor of Safety	Liquefy
36.5	TBBLAPST11S3	36.5	1.69	105.456	3849.144	3849.144	54.51	0.92	32.60	0.021	0.3	14.46341	NO
55.3	TBBLAPST12S1	18.8	1.76	109.824	549.12	4398.264	62.29	0.74	29.96	0.032	0.2	6.325447	NO
76.7	TBBLAPST13S4	21.4	2.08	129.792	1297.92	5696.184	80.67	0.60	31.46	0.035	0.28	8.100067	NO
96.5	TBBLAPST14S3	19.8	2.47	154.128	1541.28	7237.464	102.49	0.53	35.31	0.029	0.29	9.986091	NO
97	TBBLAPST14S4	0.5	2.47	154.128	1541.28	8778.744	124.32	0.52	42.02	0.015	0.26	16.86667	NO
115.2	TBBLAPST15S1	18.2	1.92	119.808	1198.08	9976.824	141.29	0.50	45.92	0.016	0.24	14.57371	NO
115.8	TBBLAPST15S2	0.6	1.92	119.808	1198.08	11174.9	158.25	0.50	51.43	0.013	0.34	26.1051	NO
116.4	TBBLAPST15S3	0.6	1.92	119.808	1198.08	12372.98	175.22	0.50	56.95	0.011	0.28	25.12334	NO
135.3	TBBLAPST16S1	18.9	2.16	134.784	1347.84	13720.82	194.31	0.50	63.15	0.012	0.43	35.93942	NO
136	TBBLAPST16S2	0.7	2.16	134.784	1347.84	15068.66	213.40	0.50	69.35	0.011	0.34	32.26891	NO

Figure 48: *Liquefaction potential analysis for the April 7, 2016 blast*

4/11/16 Blast

Seis	PPV (in/sec)	f (Hertz)	a (g)
Seis 1	0.315	6.8	0.034867
Seis 2	0.365	7.2	0.042778
Seis 3	0.42	7.3	0.049907
Seis 4	0.2	5.1	0.016603
Seis 5	0.125	3.6	0.007325

P_a (psf) 30.03 2124.58 psf

Seis 1

Total Depth (ft)	Sample	Depth (ft)	Specific Gravity	Total Unit Weight (pcf)	σ_v Layer (psf)	σ_v Depth (psf)	τ_r (psf)	r_d	τ_{cyc} (psf)	CSR	CRR	Factor of Safety	Liquefy
36.5	TBBLAPST11S3	36.5	1.69	105.456	3849.144	3849.144	134.21	0.92	80.26	0.051	0.3	5.874493	NO
55.3	TBBLAPST12S1	18.8	1.76	109.824	549.12	4398.264	153.35	0.74	73.76	0.078	0.2	2.569159	NO
76.7	TBBLAPST13S4	21.4	2.08	129.792	1297.92	5696.184	198.61	0.60	77.46	0.085	0.28	3.289943	NO
96.5	TBBLAPST14S3	19.8	2.47	154.128	1541.28	7237.464	252.35	0.53	86.93	0.071	0.29	4.055976	NO
97	TBBLAPST14S4	0.5	2.47	154.128	1541.28	8778.744	306.09	0.52	103.46	0.038	0.26	6.850609	NO
115.2	TBBLAPST15S1	18.2	1.92	119.808	1198.08	9976.824	347.86	0.50	113.05	0.041	0.24	5.919294	NO
115.8	TBBLAPST15S2	0.6	1.92	119.808	1198.08	11174.9	389.63	0.50	126.63	0.032	0.34	10.60291	NO
116.4	TBBLAPST15S3	0.6	1.92	119.808	1198.08	12372.98	431.41	0.50	140.21	0.027	0.28	10.20416	NO
135.3	TBBLAPST16S1	18.9	2.16	134.784	1347.84	13720.82	478.40	0.50	155.48	0.029	0.43	14.59724	NO
136	TBBLAPST16S2	0.7	2.16	134.784	1347.84	15068.66	525.40	0.50	170.75	0.026	0.34	13.10642	NO

Seis 2

Total Depth (ft)	Sample	Depth (ft)	Specific Gravity	Total Unit Weight (pcf)	σ_v Layer (psf)	σ_v Depth (psf)	τ_r (psf)	r_d	τ_{cyc} (psf)	CSR	CRR	Factor of Safety	Liquefy
36.5	TBBLAPST11S3	36.5	1.69	105.456	3849.144	3849.144	164.66	0.92	98.47	0.063	0.3	4.788115	NO
55.3	TBBLAPST12S1	18.8	1.76	109.824	549.12	4398.264	188.15	0.74	90.50	0.096	0.2	2.094041	NO
76.7	TBBLAPST13S4	21.4	2.08	129.792	1297.92	5696.184	243.67	0.60	95.03	0.104	0.28	2.681529	NO
96.5	TBBLAPST14S3	19.8	2.47	154.128	1541.28	7237.464	309.60	0.53	106.66	0.088	0.29	3.305898	NO
97	TBBLAPST14S4	0.5	2.47	154.128	1541.28	8778.744	375.53	0.52	126.93	0.047	0.26	5.583715	NO
115.2	TBBLAPST15S1	18.2	1.92	119.808	1198.08	9976.824	426.79	0.50	138.71	0.050	0.24	4.82463	NO
115.8	TBBLAPST15S2	0.6	1.92	119.808	1198.08	11174.9	478.04	0.50	155.36	0.039	0.34	8.642098	NO
116.4	TBBLAPST15S3	0.6	1.92	119.808	1198.08	12372.98	529.29	0.50	172.02	0.034	0.28	8.317087	NO
135.3	TBBLAPST16S1	18.9	2.16	134.784	1347.84	13720.82	586.95	0.50	190.76	0.036	0.43	11.89775	NO
136	TBBLAPST16S2	0.7	2.16	134.784	1347.84	15068.66	644.60	0.50	209.50	0.032	0.34	10.68263	NO

Seis 3

Total Depth (ft)	Sample	Depth (ft)	Specific Gravity	Total Unit Weight (pcf)	σ_v Layer (psf)	σ_v Depth (psf)	τ_r (psf)	r_d	τ_{cyc} (psf)	CSR	CRR	Factor of Safety	Liquefy
36.5	TBBLAPST11S3	36.5	1.69	105.456	3849.144	3849.144	192.10	0.92	114.88	0.073	0.3	4.104098	NO
55.3	TBBLAPST12S1	18.8	1.76	109.824	549.12	4398.264	219.51	0.74	105.58	0.111	0.2	1.794892	NO
76.7	TBBLAPST13S4	21.4	2.08	129.792	1297.92	5696.184	284.28	0.60	110.87	0.122	0.28	2.298454	NO
96.5	TBBLAPST14S3	19.8	2.47	154.128	1541.28	7237.464	361.20	0.53	124.43	0.102	0.29	2.833627	NO
97	TBBLAPST14S4	0.5	2.47	154.128	1541.28	8778.744	438.12	0.52	148.09	0.054	0.26	4.786042	NO
115.2	TBBLAPST15S1	18.2	1.92	119.808	1198.08	9976.824	497.92	0.50	161.82	0.058	0.24	4.135397	NO
115.8	TBBLAPST15S2	0.6	1.92	119.808	1198.08	11174.9	557.71	0.50	181.26	0.046	0.34	7.407513	NO
116.4	TBBLAPST15S3	0.6	1.92	119.808	1198.08	12372.98	617.50	0.50	200.69	0.039	0.28	7.128932	NO
135.3	TBBLAPST16S1	18.9	2.16	134.784	1347.84	13720.82	684.77	0.50	222.55	0.042	0.43	10.19807	NO
136	TBBLAPST16S2	0.7	2.16	134.784	1347.84	15068.66	752.04	0.50	244.41	0.037	0.34	9.15654	NO

Seis 4

Total Depth (ft)	Sample	Depth (ft)	Specific Gravity	Total Unit Weight (pcf)	σ_v Layer (psf)	σ_v Depth (psf)	τ_r (psf)	r_d	τ_{cyc} (psf)	CSR	CRR	Factor of Safety	Liquefy
36.5	TBBLAPST11S3	36.5	1.69	105.456	3849.144	3849.144	63.91	0.92	38.22	0.024	0.3	12.33644	NO
55.3	TBBLAPST12S1	18.8	1.76	109.824	549.12	4398.264	73.03	0.74	35.13	0.037	0.2	5.395234	NO
76.7	TBBLAPST13S4	21.4	2.08	129.792	1297.92	5696.184	94.58	0.60	36.88	0.041	0.28	6.908881	NO
96.5	TBBLAPST14S3	19.8	2.47	154.128	1541.28	7237.464	120.17	0.53	41.40	0.034	0.29	8.517549	NO
97	TBBLAPST14S4	0.5	2.47	154.128	1541.28	8778.744	145.76	0.52	49.27	0.018	0.26	14.38628	NO
115.2	TBBLAPST15S1	18.2	1.92	119.808	1198.08	9976.824	165.65	0.50	53.84	0.019	0.24	12.43052	NO
115.8	TBBLAPST15S2	0.6	1.92	119.808	1198.08	11174.9	185.54	0.50	60.30	0.015	0.34	22.26611	NO
116.4	TBBLAPST15S3	0.6	1.92	119.808	1198.08	12372.98	205.43	0.50	66.77	0.013	0.28	21.42873	NO
135.3	TBBLAPST16S1	18.9	2.16	134.784	1347.84	13720.82	227.81	0.50	74.04	0.014	0.43	30.65421	NO
136	TBBLAPST16S2	0.7	2.16	134.784	1347.84	15068.66	250.19	0.50	81.31	0.012	0.34	27.52348	NO

Seis 5

Total Depth (ft)	Sample	Depth (ft)	Specific Gravity	Total Unit Weight (pcf)	σ_v Layer (psf)	σ_v Depth (psf)	τ_r (psf)	r_d	τ_{cyc} (psf)	CSR	CRR	Factor of Safety	Liquefy
36.5	TBBLAPST11S3	36.5	1.69	105.456	3849.144	3849.144	28.19	0.92	16.86	0.011	0.3	27.96259	NO
55.3	TBBLAPST12S1	18.8	1.76	109.824	549.12	4398.264	32.22	0.74	15.50	0.016	0.2	12.2292	NO
76.7	TBBLAPST13S4	21.4	2.08	129.792	1297.92	5696.184	41.72	0.60	16.27	0.018	0.28	15.66013	NO
96.5	TBBLAPST14S3	19.8	2.47	154.128	1541.28	7237.464	53.01	0.53	18.26	0.015	0.29	19.30644	NO
97	TBBLAPST14S4	0.5	2.47	154.128	1541.28	8778.744	64.30	0.52	21.73	0.008	0.26	32.6089	NO
115.2	TBBLAPST15S1	18.2	1.92	119.808	1198.08	9976.824	73.08	0.50	23.75	0.009	0.24	28.17584	NO
115.8	TBBLAPST15S2	0.6	1.92	119.808	1198.08	11174.9	81.86	0.50	26.60	0.007	0.34	50.46985	NO
116.4	TBBLAPST15S3	0.6	1.92	119.808	1198.08	12372.98	90.63	0.50	29.46	0.006	0.28	48.57179	NO
135.3	TBBLAPST16S1	18.9	2.16	134.784	1347.84	13720.82	100.50	0.50	32.66	0.006	0.43	69.48287	NO
136	TBBLAPST16S2	0.7	2.16	134.784	1347.84	15068.66	110.38	0.50	35.87	0.005	0.34	62.38656	NO

Figure 49: *Liquefaction potential analysis for the April 11, 2016 blast*

3.5 Discussion

The data above shows potential initiation of liquefaction for the June 22, 2015, blast and the July 28, 2015, blast for our hypothetical dam scenario. The results show that the liquefaction potential is evident under the Seis 1 and 2 locations on the dam and that locations beyond these points show no liquefaction potential. This suggests that the attenuation of the particle velocity farther along the dam represents a load reduction such that liquefaction thresholds are no longer reached or exceeded in any instrumented point of the impoundment. Thus, monitoring of each blast is recommended to be conducted in at least two locations, both close to the abutment near the blasting site, one in original ground (Location 1) and the other on the embankment (Location 2). Next figure illustrates the recommended locations.

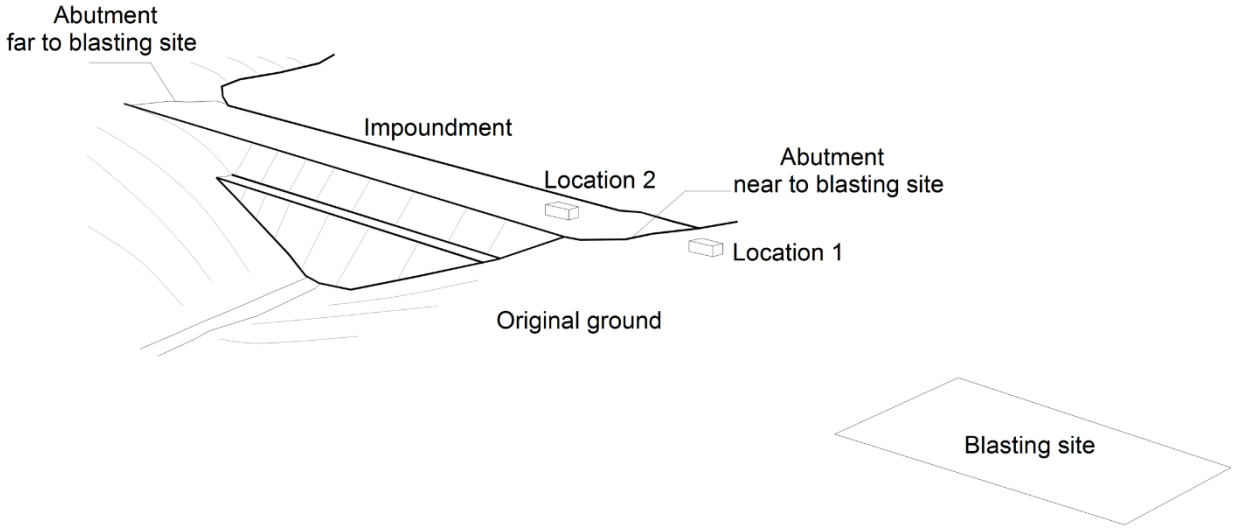

Recommended locations for vibrations monitoring

For the instrumentation on the impoundment (Location 2), and for some specific cases, the collection of the information at this location may be difficult and additional factors such as equipment and construction activities should be considered to avoid false triggered events and seismograph equipment damage.

Based on the data at Seis 1 and Seis 2, potential lignification exists at vibration levels between 1.0 and 2.0 in/s provided the material in these areas is saturated. This aligns with the current recommended Bureau of Reclamation vibration limits of 1.0 in/s for saturated loose sand or silt foundation soils or 2.0 in/s for unsaturated medium dense sand or silt foundation soils. These vibration limit guidelines from the Bureau of Reclamation are recommended for coal mine refuse impoundments when blasting is near-by. The level of pore pressure required for initiation of liquefaction is related to the amplitude, frequency, and

duration of the seismic event to induce cyclic loading. (Kramer, 1996) The cyclic stress approach used above uses peak acceleration to calculate the load and liquefaction is caused by excess pore pressure generated by a threshold number of cycles of loading. The duration of the event must be long enough and the amplitude (magnitude) large enough to create the needed number of cycles. (Kramer, 1996) Consequently, in the above approach, the duration of the event is not reflected in the analysis. Blasting duration tends to be much shorter, and amplitude tends to be much smaller than earthquake duration and amplitude respectively even though blasting generated particle acceleration sometimes meets or exceeds that of earthquakes. The effect of the short blasting duration on cyclic loading needs further study.

Similarly, the above-simplified approach relies on initial density of the soil and stress conditions but research has shown influence by several other factors. (Kramer, 1996). For example, liquefaction resistance is influenced by different soil structures, different methods of specimen preparation, the history of prior seismic strain on the material, showing increased resistance with increased overconsolidation, revealing a susceptibility to strain hardening. (Kramer, 1996)

Therefore, approaches to the analysis of the effects of blasting that ignore duration, frequency, and magnitude and only center on peak particle velocity or acceleration and do not include the various factors that affect liquefaction resistance may produce a false result showing potential for liquefaction. More research is needed in actual field conditions of blasting near an impoundment to identify the true effect of blasting on these structures.

3.6 Conclusions and Recommendations

The main propose of the computational evaluation objective was to develop a computer model using advanced numerical modeling techniques, finite elements or finite difference analysis to study the performance of impoundments under static and dynamic conditions. This necessary, nondestructive tool would allow analysis of the consequences of exposing simulated impoundments beyond the dynamic limit imposed by common mining production blasting. However, correlation and calibration efforts have proven very difficult, and the model has not responded to several attempts to calibrate the load. If this load is not properly applied and calibrated, the resultant pore pressures generated by the model if any, would not be reliable and therefore could not be used in this analysis. Therefore, copies of

the code used to create and calibrate the model are provided in Appendix 2 so that another researcher can continue to work with FLAC3D and find a better solution.

Access to the study site was restricted due to a bankruptcy and later due to some misunderstandings between the new owners of the site and the University of Kentucky. Thus, as a result, very little data was able to be collected for the project. Access was allowed for three days but the data collected was inconclusive. The only available data from the site was the results from the array of six WVDEP seismographs placed along the edge of the crest of the pushout. The analysis involved calculating values of CSR using the data obtained from the WVDEP seismographs with the resulting CSR compared to the CRR from the Salehian dissertation to provide an analysis whether the blasting effects will have a potential to cause liquefaction in coal fines. Liquefaction potential was noted for the blasts on June 22, 2015, and July 28, 2015. The analysis, which is an earthquake analysis method, does not consider the marked difference in duration, frequency, and magnitude that is characteristic of blasting as compared to an earthquake. Consequently, analysis of the seismograph records graciously collected and provided by the WVDEP absent data on acceleration and pore pressure within the fine refuse in the impoundment does not allow determination of limits on blasting near impoundments. The following conclusions and recommendations are suggested:

- Continue to use the 2.0 inches per second limit published by the Bureau of Reclamation until further research is accomplished.

- Monitoring of the blast is recommended to be located at least in two locations both close to the abutment near to the blasting site, one in original ground and the other on the impoundment.

- Downstream and upstream failure should be considered in the dynamic analysis of coal impoundments subjected to blast vibrations. Upstream failure is most likely because of the saturation condition of the material at this side of the impoundment.

- Future research efforts should be geared toward determining the effect of duration and frequency on the fines in the impoundment by vibrations produced by blasting.

- Future research is needed to define the stress hardening dynamic characteristic of coal fines.

References

Ahlberg, J.E., Fowler, J., and Heller, L.W. (1972), "Earthquake Resistance of Earth and Rock Fill Dams: Analysis of Response of Rifle Gap Dam to Project Rulison Underground Nuclear Detonation," U.S. Army WES, Misc. Paper S-71-17, June.

Almes, R.G., Butail, A. (1976). "Coal refuse: its behavior related to the design and operation of coal refuse disposal facilities." Proceedings of the Seventh Ohio Valley Soils Seminar on Shales and Mine Wastes: Geotechnical Properties, Design and Construction. Lexington, KY. pp. 9.

Bretz, T.E. (1990). "Soil Liquefaction Resulting From Blast-Induced Spherical Stress Waves," Weapons Laboratory Air Force Systems Command, Report Number WL-TR-89-100, New Mexico.

Busch, R.A., Backer, R.R. and Atkins, L.A. (1974) Physical Property Data on Coal Waste Embankment Materials, Bureau of Mines Report of Investigations 7964, 142 pp.

Charlie, W.A. (1985), "Review of Present Practices Used in Predicting the Effects of Blasting on Pore Pressure," U.S. Bureau of Reclamation, Report No. GR-85-9, Denver, CO, November, pp. 9-10.

Charlie, W.A., Lewis, W.A., Doehring, D.O. (2001), "Explosive Induced Pore Pressure in a Sandfill Dam," American Society for Testing Materials, p. 395.

Chen C.Y. (1976). Investigation and Statistical Analysis of the Geotechnical Properties of Coal Mine Refuse, Ph.D. Thesis, University of Pittsburgh, 196p.

DPlot Graphing Software for Scientists and Engineers, Version 2.3.5.3, Copyright 2001-2014 by HydeSoft Computing, LLC

Dunnicliff, J., Greene, G.E., (1993), "Geotechnical Instrumentation for Monitoring Field Performance," John Wiley & Sons, New York.

GeoEnvironmental Associates, Inc. (2009-2013), "Proposed Additional Stages to Slurry Impoundment," Knoxville.

Hegazy, Y.A., A.G. Cushing and C.J. Lewis. (2004). "Physical, Mechanical, and Hydraulic Properties of Coal Refuse for Slurry Impoundment Design". Proceedings, 2nd International Site Characterization Conference, Porto, Portugal.

International Society of Explosives Engineers (ISEE) (2011), "ISEE Blasters' Handbook," ISEE, 2nd ed., 2011, Cleveland, Ohio.

Itasca Consulting Group Inc. (2009), "Fast Lagrangian Analysis of Continua in Three Dimensions (FLAC3D) User's Guide," 4th edition, Minneapolis.

Jamison H. Steidl., Sandra H. Seale. (2010). “Observations and Analysis of Ground Motion and Pore Pressure at the NEES Instrumented Geotechnical Field Sites”. Fifth International Conference on Recent Advances in Geotechnical Earthquake Engineering and Soil Dynamics. May, 2010. San Diego, California.

Kramer Steven L. (1996). “Geotechnical Earthquake Engineering”. Prentice Hall, New Jersey.

Larson-Robl, K. (2015), “Pore Pressure Measurement Instrumentation Response to Blasting,” PowerPoint Presentation, University of Kentucky, Lexington, Kentucky.

Larson-Robl, K., Silva-Castro, J., PhD., Hoffman, J.M., PhD. (2015), “Blasting Effects on Pore Pressure in Coal Impoundments (Dry Conditions-Part I),” 41st Conference on Explosives and Blasting Technique, International Society of Explosives Engineers, February 2015, New Orleans, Louisiana.

Makdisi F.I., Seed H.B., (1978). “Simplified Procedure for Estimating Dam and Embankment Earthquake-Induced Deformations” J. Geotech. Eng’g, ASCE, Vol. 104, No. GT7, July 1978, pp 849-867.

McLeod H.N., Rice S., Davies M.P. (1992). “Innovative Design Aspects for Tailing Impoundments in Seismic Areas”. International Mine waste Management

Radoslaw L., Michalowski. (2002). “Stability Charts for Uniform Slopes”. Journal of Geotechnical and Geoenvironmental Engineering, April 2002. pp 351-355

Regents of the University of California, Davis Campus (accessed 2015), “Construction Slide in Calaveras Dam,” web page https://research.engineering.ucdavis.edu/gpa/embankment-dams/.

Rouse, G.C., and Roehm, L.H. (1969), #Vibration of Navajo Dam Following a Subsurface Nuclear Blast,” U.S. Bureau of Reclamation, Report No. DD-9, Denver, CO, July.

Rouse, G.C., Roehm, L.H., and Cozart, C.W. (1970), “Vibration of Vega Dam Following Rulison Subsurface Nuclear Blast,” U.S. Bureau of Reclamation, Report No. REC-OCE-70-15, Denver, CO, April.

Salehian, A. (2013), “Predicting the Dynamic Behavior of Coal Mine Tailings Using State-of-Practice Geotechnical Field Methods,” University of Kentucky.

Saxena, S.K., Lourie, D.E., Rao, J.S. (1984). “Compaction criteria for eastern coal waste embankments.” Journal of Geotechnical Engineering. American Society of Civil Engineers. Vol. 110 (2). pp. 262-284.

U.S Department of Labor Mine Safety and Health Administration (2009). “Engineering and Design Manual. Coal Refuse Disposal Facilities”. Second Edition May 2009.

Acknowledgments

The authors acknowledge the assistance of government agencies; OSM, WVDEP, University of Kentucky. Much of the fieldwork and data reduction and analysis were performed by graduate student Paul Sainato. Special thanks go to Ken Eltschlager Office of Surface Mining – Appalachian Region by his suggestions through this research and the discussions in order to improve this report.

Appendix 1

Three aspects should be considered when preparing a model for dynamic analysis: dynamic loading and boundary conditions, wave transmission through the model, and mechanical damping. (Itasca, 2009)

A.1 Dynamic Loading and Boundary Conditions

FLAC3D models dynamic loading by using a dynamic input either on a boundary of the material or at an internal grid point. (Itasca, 2009) Dynamic input is applied in one of the following ways: an acceleration history, a velocity history, a stress (or pressure) history, or a force history. (Itasca, 2009) The history function acts as a multiplier on the specific dynamic input. (Itasca, 2009) It is assigned either as a table of values or a FISH function. (Itasca, 2009) FISH is a programming language imbedded in FLAC3D. (Itasca, 2009) A table of values has the multiplier value and the associated time value (e.g. a seismic record) as individual pairs that can be imported into FLAC3D. (Itasca, 2009) FISH functions include the multiplier value but a time value must be provided by the FISH function. (Itasca, 2009) Wave reflections are minimized by creating quiet boundaries at the borders of materials and at the interfaces between materials. (Itasca, 2009) Dynamic inputs can be applied in the *x-, y-,* or *z-* directions or in the normal and shear directions but cannot be applied along a quiet boundary. (Itasca, 2009) To apply a force at a quiet boundary, a stress boundary condition must be used. (Itasca, 2009) A velocity wave can be converted to stress as follows: (Itasca, 2009)

$$\sigma_n = 2(\rho\, C_p)v_n \qquad (6)$$

or

$$\sigma_s = 2(\rho\, C_s)v_s \qquad (7)$$

where: σ_n = applied normal stress;

σ_s = applied shear stress;

ρ = mass density;

C_p = speed of *p*-wave propagation through medium;

C_s = speed of *s*-wave propagation through medium;

v_n = input normal particle velocity; and

v_s = input shear particle velocity. (Itasca, 2009)

C_p is given by

$$C_p = \sqrt{\frac{K + {}^{4G}/_{3}}{\rho}} \qquad (8)$$

and C_s is given by

$$C_s = \sqrt{\frac{G}{\rho}} \qquad (9)$$

assuming plane-wave conditions. (Itasca, 2009) K is the drained bulk modulus and G is the shear modulus. (Itasca, 2009) The factor of 2 in equations 6 and 7 accounts for half of the input being absorbed by a quiet boundary. (Itasca, 2009)

If "raw" acceleration or velocity records are used, the model may continue to show velocities or residual displacements after the motion has finished due to the integral of the raw time record not being zero. (Itasca, 2009) If so, a baseline correction may need to be applied to ensure the final velocity and displacement are both zero but usually only applies when using complex waveforms such as waveforms from field measurements. (Itasca, 2009) An alternative to baseline correction is to apply a displacement shift at the end of the calculation by adding a fixed velocity to force the velocity and displacement to zero, an action that will not affect the mechanics of the model. (Itasca, 2009)

Geomechanical modeling assumes that surface or near-surface structures lie on a half-space in order to rely on the discretization of a finite region with appropriate conditions enforced at artificial boundaries. (Itasca, 2009) A fixed or elastic boundary will reflect outward propagating waves back into the model where a quiet boundary is needed to allow radiation of the energy of the wave. (Itasca, 2009) A viscous boundary using independent dashpots in the normal and shear directions at the boundary developed by Lysmer and Kuhlemeyer (1969) is used in FLAC3D and is almost completely effective at absorbing waves approaching the boundary at an incidence greater than 30 degrees but less effective with waves at less incidence. (Itasca, 2009) The dashpots provide viscous normal (t_n) and shear tractions (t_s) given by:

$$t_n = \rho\, C_p\, v_n \qquad (10)$$

$$t_s = \rho\, C_s\, v_s \qquad (11)$$

where: v_n and v_s are the normal and shear components of the velocity at the boundary;

ρ is the mass density; and C_p and C_s are the p- and s-wave velocities. (Itasca, 2009)

These tractions are calculated and applied at every timestep. (Itasca, 2009) Quiet boundaries are used when the input is internal but free field boundaries should be used when a dynamic input is applied externally to the boundary. (Itasca, 2009)

In FLAC3D, free-field motion is enforced by coupling the boundary with a free-field grid by viscous dashpots to simulate a quiet boundary while the unbalanced forces from the free-field grid are applied to the main-grid boundary using the following equations. (Itasca, 2009)

$$F_x = -\rho C_p\left(v_x^m - v_x^{ff}\right)A + F_x^{ff} \qquad (12)$$

$$F_y = -\rho C_s\left(v_y^m - v_y^{ff}\right)A + F_y^{ff} \qquad (13)$$

$$F_x = -\rho C_s\left(v_z^m - v_z^{ff}\right)A + F_z^{ff} \qquad (14)$$

where:

ρ = density of material along vertical model boundary;

C_p = p-wave speed at the side boundary;

C_s = s-wave speed at the side boundary;

A = area of influence of free-field gridpoint;

v_x^m = x-velocity of gridpoint in main grid at side boundary;

v_y^m = y-velocity of gridpoint in main grid at side boundary;

v_z^m = z-velocity of gridpoint in main grid at side boundary;

v_x^{ff} = x-velocity of gridpoint in side free field;

v_y^{ff} = y-velocity of gridpoint in side free field;

v_z^{ff} = z-velocity of gridpoint in side free field;

F_x^{ff} = free-field gridpoint force with contributions from the σ_{xx}^{ff} stresses of the free-field zones around the gridpoint;

F_y^{ff} = free-field gridpoint force with contributions from the σ_{xy}^{ff} stresses of the free-field zones around the gridpoint; and

F_z^{ff} = free-field gridpoint force with contributions from the σ_{xz}^{ff} stresses of the free-field zones around the gridpoint. (Itasca, 2009)

Thus, plane waves suffer no distortion at the boundary. (Itasca, 2009)

A.2 Wave Transmission Through the Model

Numerical distortion of the propagating wave can occur because both the frequency and wave speed characteristics of the wave will affect the numerical accuracy of the transmission. (Itasca, 2009) Kuhlemeyer and Lysmer (1973) show that, for accuracy the spatial element size, Δl, must be smaller than approximately one-tenth to one-eighth of the

wavelength associated with the highest frequency component of the input wave as shown in the following equation. (Itasca, 2009)

$$\Delta l = \frac{\lambda}{10} \qquad (15)$$

Where λ is the wavelength associated with the highest frequency component that contains

appreciable energy. (Itasca, 2009) For dynamic input with a high peak velocity and short rise time, such as blasting, this requirement may require a fine mesh and small timestep which could increase the time of processing and memory usage beyond reasonable limits. (Itasca, 2009) It may be possible to adjust the input by recognizing that most of the power is contained in lower-frequency components and removing the higher-frequency components and allowing a coarser mesh to be used. (Itasca, 2009) This filtering can be performed using a Fast Fourier Transform technique. (Itasca, 2009) For example, the figure below shows an unfiltered velocity record.

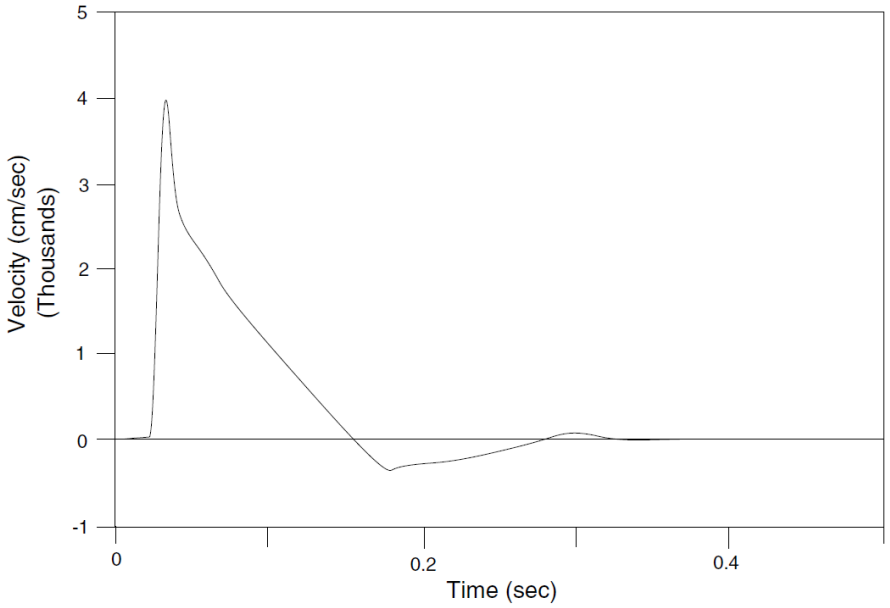

Figure 39 *Unfiltered velocity history (from Itasca, 2009)*

The highest frequency of this input exceeds 50 Hz but, as shown by the power spectral density plot of Fourier amplitude versus frequency in the figure below, most of the power (approximately 99%) is made up of components of frequency 15 Hz or lower. (Itasca, 2009)

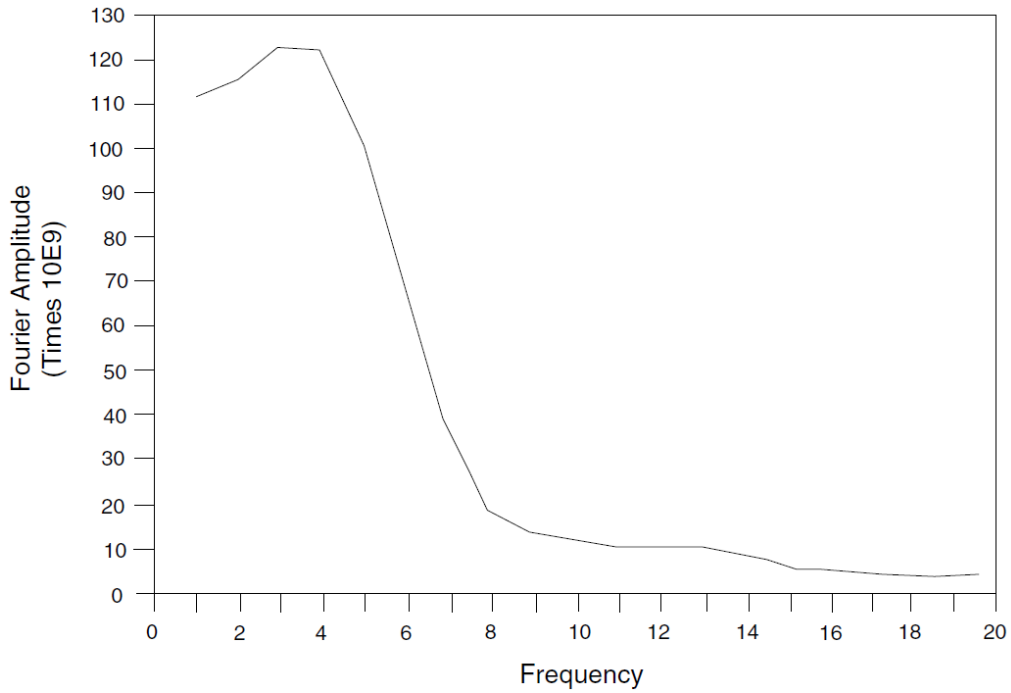

Figure A2 *Unfiltered Fourier power spectral density plot (from Itasca, 2009)*

Filtering this velocity history with a 15 Hz low-pass filter gives less than one percent power loss while the peak velocity is reduced 38 percent and the rise time is shifted from 0.035 to 0.09 second. (Itasca, 2009) The filtered velocity history and the filtered Fourier amplitudes are shown in the figures below.

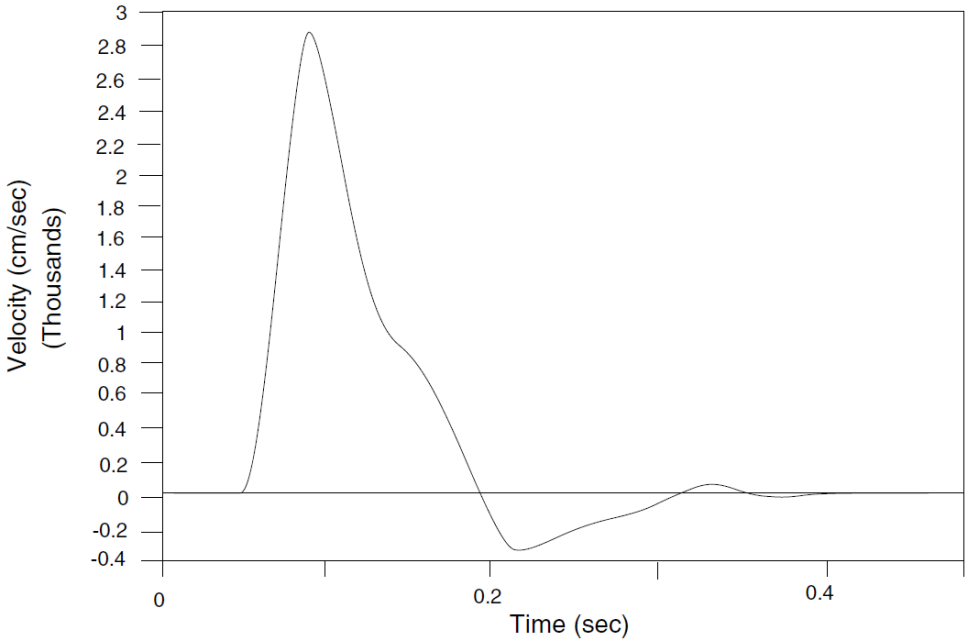

Figure 40 *Velocity history filtered at 15 Hz (from Itasca, 2009)*

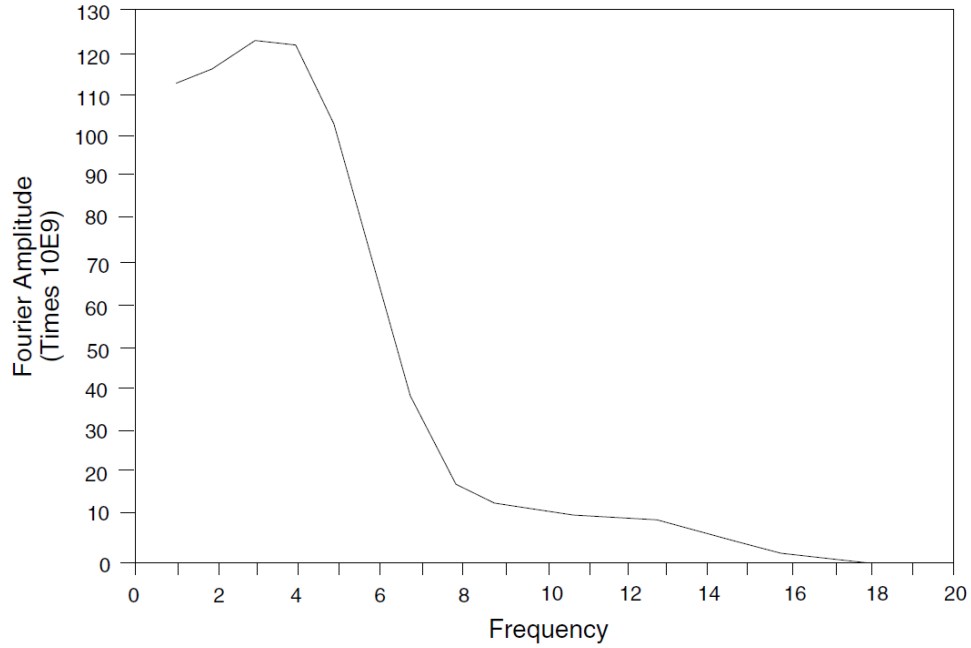

Figure 41 *Fourier power spectral density plot filtered at 15 Hz (from Itasca, 2009)*

To evaluate the influence of the filter, analysis should be performed at different levels of filtering. (Itasca, 2009) Data must be filtered before application to FLAC3D or "ringing" (super-imposed oscillations) that are not actual will occur. (Itasca, 2009) There are upper limits in any discretized medium that must be respected or the results are meaningless. (Itasca, 2009).

A.3 Mechanical Damping

Natural dynamic systems contain some degree of damping or else they would continue to vibrate infinitely due to a dynamic input. (Itasca, 2009) Damping is due to internal friction in the material. (Itasca, 2009) For dynamic loading, the damping in soil and rock is largely hysteretic or independent of frequency but this is hard to represent in numerical modeling because not all components are damped equally at the same time due to superimposed waves and hysteretic processes lead to path-dependence. (Itasca, 2009) FLAC3D allows a choice between Rayleigh damping and hysteretic damping processes for modeling dynamic problems. (Itasca, 2009)

Rayleigh damping allows frequency-independent damping over a restricted range of frequencies to give an average response and is commonly associated with plastic models that are linear-equivalent but does not work as well with materials with differing properties. (Itasca, 2009) Hysteretic damping uses strain-dependent modulus and damping functions incorporated into the simulation and gives more realistic responses allowing for different damping levels for materials with different properties. (Itasca, 2009)

Hysteretic damping used in conjunction with one of the non-linear models in FLAC3D (such as the Finn model used here) gives a more realistic yielding response. (Itasca, 2009).

Assuming an ideal soil in which stress depends only on strain and not the number of cycles or time, an incremental constitutive relation can be derived as described by $\bar{\tau}/\gamma = M_s$ where $\bar{\tau}$ is the normalized shear stress, γ is the shear strain, and M_s is the normalized secant modulus. (Itasca, 2009)

$$\bar{\tau} = M_s \gamma \qquad (16)$$

$$M_t = \frac{d\bar{\tau}}{d\gamma} = M_s + \gamma \frac{dM_s}{d\gamma} \qquad (17)$$

where M_t is the normalized tangent modulus. (Itasca, 2009) The incremental shear modulus in a nonlinear simulation is then given by $G_o M_t$. (Itasca, 2009) The shear strain is decomposed into components and strain reversals are detected by changes in signs of the dot product of the current increment and the previous mean path as shown by the following equations. (Itasca, 2009)

$$\gamma_1 = \gamma_1 + 2\Delta e_{12} \qquad (18)$$

$$\gamma_2 = \gamma_2 + 2\Delta e_{23} \qquad (19)$$

$$\gamma_3 = \gamma_3 + 2\Delta e_{31} \qquad (20)$$

$$\gamma_4 = \gamma_4 + \frac{2(\Delta e_{11} - \Delta e_{22})}{\sqrt{6}} \qquad (21)$$

$$\gamma_5 = \gamma_5 + \frac{2(\Delta e_{22} - \Delta e_{33})}{\sqrt{6}} \qquad (22)$$

$$\gamma_6 = \gamma_6 + \frac{2(\Delta e_{33} - \Delta e_{11})}{\sqrt{6}} \qquad (23)$$

$$v_i = \gamma_i^{\circ} - \gamma_i^{\circ\circ} \qquad (24)$$

$$z = \sqrt{v_i v_i} \qquad (25)$$

$$n_i^{\circ} = \frac{v_i}{z} \qquad (26)$$

$$d = (\gamma_i - \gamma_i^{\circ}) n_i^{\circ} \qquad (27)$$

A reversal is detected when $|d|$ passes through a maximum, and the previous-reversal strain values are updated as given by the following equations. (Itasca, 2009)

$$\gamma_i^{\circ\circ} = \gamma_i^{\circ} \qquad (28)$$

$$\gamma_i^{\circ} = \gamma_i \qquad (29)$$

Between reversals, the shear modulus is multiplied by M_t, using $\gamma = |\alpha|$ in equation 17. (Itasca, 2009)

A.4 Liquefaction Modeling

Liquefaction is the loss of shear strength of soil under monotonic or cyclic loading, arising from a tendency for loose soil to compact under shear loading. (Itasca, 2009) Effective stress does not necessarily have to be zero for soil to liquefy. (Itasca, 2009)

Pore pressures have been known to build up in some sands during cyclic loading and this process could lead to liquefaction when the effective stress decreases. (Itasca, 2009) Although excess pore pressures are associated with liquefaction, the cause of liquefaction is the reduction of contact forces between grains of soil in the material which cause reduction in effective stress. (Itasca, 2009) Alternatively, it is the irrecoverable reduction of porosity during cyclic compaction that generates pore pressure and, consequently, a decrease in effective stress. (Itasca, 2009)

Dilation plays a key role in liquefaction. (Itasca, 2009) As soil becomes denser due to repeated shear cycles, soil grain rearrangement may be inhibited, forcing particles to move up against adjacent particles causing dilation, an increase in effective stress, a decrease in pore pressure and consequently limiting the densification process. (Itasca, 2009)

Liquefaction is not modeled directly in FLAC3D. (Itasca, 2009) Coupled dynamic-groundwater flow is calculated and, by default, pore fluid responds to changes in pore volume caused by dynamic mechanical loading with the average pore pressure remaining constant in the analysis. (Itasca, 2009)

Pore pressure buildup is a secondary effect, the primary effect is the irrecoverable volume contraction that occurs when the confining stress is held constant. (Itasca, 2009) Given there is no volume change but only grain rearrangement with the confining stress held constant, the volume of the void spaces decreases, pore pressure increases due to the

transfer of the confining force from grains to fluid, and effective stress decreases. (Itasca, 2009)

A.5 Finn Model

This mechanism, grain rearrangement while confining stress is held constant, well described by Martin et al. (1975), gives that the relation between irrecoverable volume-strain and cyclic shear-strain amplitude is independent of confining stress. (Itasca, 2009) Martin et al. supply the following equation that relates the increment of volume decrease, E_{vd}, to the cyclic shear-strain amplitude, γ, where γ is presumed to be the "engineering" shear strain: (Itasca, 2009)

$$E_{vd} = C_1(\gamma - C_2 E_{vd}) + \frac{C_3 E_{vd}^2}{\gamma + C_4 E_{vd}} \qquad (30)$$

where C_1, C_2, C_3 and C_4 are constants. (Itasca, 2009)

The increment in volume strain decreases as the irrecoverable volume strain (E_{vd}) is accumulated. (Itasca, 2009) E_{vd} should be zero if γ is zero implying that the constants relate as follows: $C_1\ C_2\ C_4 = C_3$. (Itasca, 2009)

A.6 Finn Model – Byrne Formulation

An alternative and simpler formula is proposed by Byrne (1991): (Itasca, 2009)

$$\frac{\Delta\epsilon_{vd}}{\gamma} = C_1 \exp\left(-C_2 \left(\frac{\Delta\epsilon_{vd}}{\gamma}\right)\right) \qquad (31)$$

where C_1 and C_2 are constants but not the same as above. (Itasca, 2009) In many cases, $C_2 = \frac{0.4}{C_1}$. (Itasca, 2009) In addition, a third parameter, C_3, sets the threshold shear strain (i.e., a limiting shear-strain amplitude below which volumetric strain is not produced). (Itasca, 2009)

The shear-induced volumetric strain produced by equation 31 (keeping the amplitude of the cyclic shear strain constant) versus number of cycles is shown in the figure below.

(Itasca, 2009) As shown in the figure, an increase in volumetric strain occurs with the level of cyclic shear strain and for a given strain amplitude, γ, the rate of accumulation decreases with the number of cycles as indicated by the reduced slope of the line as number of cycles increase. (Itasca, 2009)

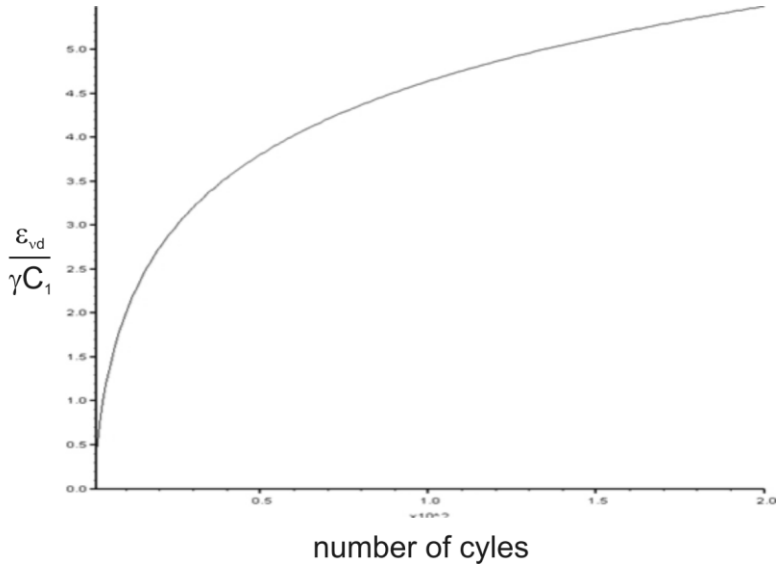

Figure 42 *Finn/Byrne – constant, cyclic shear-strain amplitude (from Itasca, 2009)*

The incremental volumetric behavior is predicted by the following equation (Itasca, 2009)

$$\Delta\sigma_m + \alpha\Delta p = K(\Delta\epsilon + \Delta\epsilon_{vd}) \qquad (32)$$

where $\sigma_m = \sigma_{ii}/3$ is the mean stress, p is pore pressure, α is Biot coefficient (= 1 for soil), K is the drained bulk modulus of the soil and ϵ is the volumetric strain. (Itasca, 2009) ϵ is positive in extension, while ϵ_{vd} is positive in compression. (Itasca, 2009) For undrained conditions, the change in pore pressure is proportional to the change in volumetric strain:

$$\Delta p = -\alpha M \Delta\epsilon \qquad (33)$$

where M is Biot modulus. (Itasca, 2009) After substitution of equation 33 into equation 32, and solving for $\Delta\epsilon$, we obtain: (Itasca, 2009)

$$\Delta\epsilon = \frac{\Delta\sigma_m - K\Delta\epsilon_{vd}}{K + \alpha^2 M} \qquad (34)$$

For a very stiff fluid (compared to the solid matrix) ($M >>> K$), equation 34 predicts no volume change. (Itasca, 2009) Further, using $\Delta\epsilon = 0$ in equation 32 gives: (Itasca, 2009)

$$\Delta\sigma_m + \alpha\Delta p = K\Delta\epsilon_{vd} \qquad (35)$$

Equation 35 predicts a *decrease in magnitude of effective stress with cyclic shear strain* (due to an increase of shear induced compaction which will show a rise in pore pressure under constant stress). (Itasca, 2009) Under conditions of constant stress, $\Delta\sigma_m = 0$, the increase in pore pressure is proportional to the drained bulk modulus of the soil: (Itasca, 2009)

$$\Delta p = K\Delta\epsilon_{vd} \qquad (36)$$

In free stress conditions, the pore pressure will remain unchanged ($\Delta p = 0$), and the magnitude of the total stress will decrease according to: (Itasca, 2009)

$$\Delta\sigma_m = K\Delta\epsilon_{vd} \qquad (37)$$

Note that in both situations, the drained (tangent) bulk modulus, K, plays an important role in determining the magnitude of the cyclic loading impact on effective stress, capturing the main physics of liquefaction. (Itasca, 2009)

The Finn model in FLAC3D incorporates both equation 30 and equation 31 into the standard Mohr-Coulomb plasticity model and can be modified by the user if needed. (Itasca, 2009) The model calculates the basic mechanisms leading to liquefaction. (Itasca, 2009) In addition to the usual material property parameters (friction, moduli, etc.), the model needs four constants for equation 30, or three constants for equation 31. (Itasca, 2009) For equation 30, Martin et al. (1975) describe how these may be determined from a *drained* cyclic test. (Itasca, 2009) For equation 31, Byrne (1991) notes that the constant, C_1, can be derived from relative densities, D_r, as follows: (Itasca, 2009)

$$C_1 = 7600 D_r^{-2.5} \quad (38)$$

Using an empirical relation between D_r and normalized standard penetration test values, $(N_1)_{60}$,

$$D_r = 15(N_1)_{60}^{\frac{1}{2}} \quad (39)$$

then

$$C_1 = 8.7(N_1)_{60}^{-1.25} \quad (40)$$

C_2 is then calculated from $C_2 = \frac{0.4}{C_1}$, in this case. (Itasca, 2009)

In the Finn model, there is logic to detect a strain reversal in the general case. (Itasca, 2009) In a three-dimensional analysis, there are at least six components of the strain-rate tensor which are accumulated as follows: (Itasca, 2009)

$$\epsilon_1 = \in_1 + \Delta\in_{12} \quad (41)$$

$$\epsilon_2 = \in_2 + \Delta\in_{23} \quad (42)$$

$$\epsilon_3 = \in_3 + \Delta\in_{31} \quad (43)$$

$$\in_4 = \in_4 + \frac{(\Delta\in_{11} - \Delta\in_{22})}{\sqrt{6}} \quad (44)$$

$$\in_5 = \in_5 + \frac{(\Delta\in_{22} - \Delta\in_{33})}{\sqrt{6}} \quad (45)$$

$$\in_6 = \in_6 + \frac{(\Delta\in_{33} - \Delta\in_{11})}{\sqrt{6}} \quad (46)$$

We use the following scheme to locate extreme points in strain space. (Itasca, 2009) Denoting the previous point by superscript ($\circ$), and the one before that with ($\circ\circ$), the previous unit vector, n_i°, in strain space is computed: (Itasca, 2009)

$$v_i = \epsilon_i^{\circ} - \epsilon_i^{\circ\circ} \quad (47)$$

$$z = \sqrt{v_i v_i} \quad (48)$$

$$n_i^{\circ} = \frac{v_i}{z} \quad (49)$$

where subscript *i* takes the values 1 to 6, and repeated indices imply summation. (Itasca, 2009) The projection d' of the new vector, $\epsilon_i - \epsilon_i^{\circ}$, from the old point to the new point is the dot product of the new vector with the previous unit vector, (Itasca, 2009)

$$d = (\epsilon_i - \epsilon_i^{\circ}) n_i^{\circ} \quad (50)$$

We use the rule that d' must be negative (so that the new strain segment corresponds to a *reversal* compared to the previous segment). (Itasca, 2009) We then monitor the absolute value of d' and make the following calculation when it passes through a maximum, d'_{max}, provided that a minimum number of timesteps has elapsed (to prevent the reversal logic being triggered again on transients that immediately follow a reversal). (Itasca, 2009)

$$\gamma = d_{max} \quad (51)$$

$$\epsilon_i^{\circ\circ} = \epsilon_i^{\circ} \quad (52)$$

$$\epsilon_i^{\circ} = \epsilon_i \quad (53)$$

The engineering shear strain, γ, is inserted into equation 30 to obtain $\Delta\epsilon_{vd}$. (Itasca, 2009) We then update ϵ_{vd}, as follows, and save it for use in equation 30. (Itasca, 2009)

$$\epsilon_{vd} := \epsilon_{vd} + \Delta\epsilon_{vd} \quad (54)$$

We also save one-third of $\Delta\epsilon_{vd}$ and revise the direct strain increments input to the model at the next cycle: (Itasca, 2009)

$$\Delta\epsilon_{11} := \Delta\epsilon_{11} + \frac{\Delta\epsilon_{vd}}{3} \quad (55)$$

$$\Delta\epsilon_{22} := \Delta\epsilon_{22} + \frac{\Delta\epsilon_{vd}}{3} \quad (56)$$

$$\Delta\epsilon_{33} := \Delta\epsilon_{33} + \frac{\Delta\epsilon_{vd}}{3} \quad (57)$$

Compressive strain increments are negative and $\Delta\epsilon_{vd}$ is positive; hence, the mean effective stress decreases. (Itasca, 2009)

Appendix 2

The following code files for FLAC3D are for Stage 1 which was an attempt to input and calibrate the blasting load into the model. A simple dam was designed to allow for a more simplified model that would run faster than a complete, more complex model of the impoundment.

File: GenGrid1

```
;-------------------------------------------------------------------------------
; Blasting Effects Verification - Stage I
;-------------------------------------------------------------------------------
;Create simplified homogeneous dam
new
config dyn
set dyn off
gen zone brick group Coarse1 p0(0,0,0) p1(320,0,0) p2(0,380,0) p3(100,0,50)
p4(320,380,0) p5(100,380,50) &
p6(220,0,50) p7(220,380,50) p8(320,0,0) p9(320,380,0) size 64,76,10
fix x y z
ini xv 0 yv 0 zv 0 xdisp 0 ydisp 0 zdisp 0
free x y z
;various property ranges to attempt calibration
model mech elastic range group Coarse1
;prop shea 625000 bulk 1212121.2 range group Coarse1 ; 214% of original moduli
;prop shea 291406.25 bulk 565151.52 range group Coarse1 ; original moduli
prop shea 233125 bulk 452121.21 range group Coarse1 ; 80% of original moduli
;prop shea 349687.5 bulk 678181.82 range group Coarse1 ; 120% of original moduli
;prop shea 407968.75 bulk 791212.12 range group Coarse1 ; 140% of original moduli
;prop shea 466250 bulk 904242.42 range group Coarse1 ; 160% of original moduli
;prop shea 524531.25 bulk 1017272.7 range group Coarse1 ; 180% of original moduli
;prop shea 582812.5 bulk 1130303 range group Coarse1 ; 200% of original moduli
;prop shea 174843.75 bulk 339090.91 range group Coarse1 ; 60% of original moduli
prop pois 0.28 range group Coarse1
; prop tens 2.0882e11 range group Coarse1
;ini dens 3.41 range group Coarse1 ;100% of 3.41
;ini dens 1.364 range group Coarse1 ;40% of 3.41
;ini dens 2.046 range group Coarse1 ;60% of 3.41
;ini dens 2.728 range group Coarse1 ;80% of 3.41
;ini dens 4.092 range group Coarse1 ;120% of 3.41
;ini dens 4.774 range group Coarse1 ;140% of 3.41
;ini dens 5.456 range group Coarse1 ;160% of 3.41
ini dens 3.069 range group Coarse1 ;90% of 3.41
;ini dens 3.751 range group Coarse1 ;110% of 3.41
save dam0
plot zone
return
```

File: GvavLoad1

```
;-------------------------------------------------------------------------
; Blasting Effects Verification - Stage I
;-------------------------------------------------------------------------
;Apply gravity loading
restore dam0
range name left y 380
range name right y 0
range name bottom z 0
apply nvel=0.0 range nrange left nrange bottom not
apply nvel=0.0 range nrange right nrange bottom not
fix y z range nrange bottom
set grav=0,0,-32.17 small
solve
save dam1
return
```

File: RealProp1

```
;-------------------------------------------------------------------------
; Blasting Effects Verification - Stage I
;-------------------------------------------------------------------------
;Apply real properties to dam
restore dam1
free x y z
; prop tens=0 cohes=280 range group Coarse1
;prop shea 625000 bulk 1212121.2 range group Coarse1 ; 214% of original moduli
;prop shea 291406.25 bulk 565151.52 range group Coarse1 ; original moduli
prop shea 233125 bulk 452121.21 range group Coarse1 ; 80% of original moduli
;prop shea 349687.5 bulk 678181.82 range group Coarse1 ; 120% of original moduli
;prop shea 407968.75 bulk 791212.12 range group Coarse1 ; 140% of original moduli
;prop shea 466250 bulk 904242.42 range group Coarse1 ; 160% of original moduli
;prop shea 524531.25 bulk 1017272.7 range group Coarse1 ; 180% of original moduli
;prop shea 582812.5 bulk 1130303 range group Coarse1 ; 200% of original moduli
;prop shea 174843.75 bulk 339090.91 range group Coarse1 ; 60% of original moduli
prop pois 0.28 range group Coarse1
;prop shea 291406.25 bulk 565151.515 range group Coarse1
;prop dens 3.41 range group Coarse1
;prop dens 1.364 range group Coarse1
;prop dens 2.046 range group Coarse1 ;60% of 3.41
;prop dens 2.728 range group Coarse1 ;80% of 3.41
;prop dens 4.092 range group Coarse1 ;120% of 3.41
;prop dens 4.774 range group Coarse1 ;140% of 3.41
;prop dens 5.456 range group Coarse1 ;160% of 3.41
;prop dens 3.069 range group Coarse1 ;90% of 3.41
prop dens 3.751 range group Coarse1 ;110% of 3.41
save dam2
return
```

File: FinnMaterial1

```
;-------------------------------------------------------------------------
; Blasting Effects Verification - Stage I
;-------------------------------------------------------------------------
;Apply Finn model and properties to dam
rest dam2
model mech finn range group Coarse1
prop shea 291406.25 bulk 565151.515 fric=33.1 range group Coarse1
prop dens 3.41 range group Coarse1
prop ff_c1 = 0.43429 ff_c2 = 0.92105 range group Coarse1
prop ff_switch = 1 ff_lat = 100000 range group Coarse1
solve
prop ff_lat 50
save dam2finn
```

File: Stage1-master

```
;-------------------------------------------------------------------------
; Blasting Effects Verification - Stage I
;-------------------------------------------------------------------------
;Driver file
new project
set fish autocreate off
title "Blasting Effects Verification - Stage I"
call GenGrid1
call GravLoad1
call RealProp1
call DynamicExcitation1
call Stage1Plot
return
```

File: Dynamic Excitation1

```
;-------------------------------------------------------------------------
; Blasting Effects Verification - Stage I
;-------------------------------------------------------------------------
;Apply dynamic load to dam
restore dam2
set dyn=on large
set dy dt 0.000977
set dy ti = 0
table 1 read 62215veltransfps
table 11 read 62215velradfps
;table 12 read 62215velvertfps
list table 1
list table 11
;list table 12
call INT.FIS
```

```
@integrate(1,2)
call baseline.fis
set @itab_unc=1 @itab_corr=10 @drift=-.000032 @ttime=8 @itab_cvel=5
@baseline
@integrate (5,6)
range name front plane dd 90 dip 63.435 orig (0,0,0)
range name back plane dd 90 dip -63.435 orig (320,0,0)
;
apply xvel=1.0 hist=table 5 range y 380.1 379.9 nrange left nrange front not nrange back
not
apply yvel=1.0 hist=table 11 range y 380.1 379.9 nrange left nrange front not nrange back
not
;apply zvel=1.0 hist=table 12 range y 380.1 379.9 nrange left nrange front not nrange back
not
apply zvel 0 range nrange right nrange front not nrange back not
apply zvel 0 range nrange left nrange front not nrange back not
;
apply dquiet squiet nquiet range z 0.0 ;nrange bottom
apply dquiet squiet nquiet range y 0.1 -0.1 ;nrange right
;
ini xv=0 yv=0 zv=0 xdis=0 ydis=0 zdis=0
;
def _get_zone_ad
global effstr1
global effstr2
global totstr1
global ppress1
ad1 = z_near(170,380,10)
ad2 = z_near(170,380,30)
ad3 = z_near(170,329,10)
ad4 = z_near(170,329,30)
end
@_get_zone_ad
def hist_eff_stress
array arr1(6) arr2(6) arr3(6) arr4(6)
effstr1 = z_szz(ad1) + z_pp(ad1)
effstr2 = z_szz(ad2) + z_pp(ad2)
totstr1 = z_szz(ad1)
ppress1 = z_pp(ad1)
totstr2 = z_szz(ad2)
ppress2 = z_pp(ad2)
dum1 = z_fsi(ad1,arr1)
dun2 = z_fsi(ad2,arr2)
dum3 = z_fsi(ad3,arr3)
dun4 = z_fsi(ad4,arr4)
strain1 = 2.0*arr1(6)
strain2 = 2.0*arr2(6)
```

```
strain3 = 2.0*arr3(6)
strain4 = 2.0*arr4(6)
end
;
set hist_rep 1
hist add dyt
hist add gp xvel 170,380,50
hist add gp xvel 170,329,50
hist add gp xvel 170,208,50
hist add gp xvel 170,10,50
hist add gp xvel 170,0,50
hist add gp xvel 170,380,10
hist add gp xvel 170,380,30
hist add gp xvel 170,329,10
hist add gp xvel 170,329,30
hist add gp yvel 170,380,50
hist add gp yvel 170,329,50
hist add gp yvel 170,208,50
hist add gp yvel 170,10,50
hist add gp yvel 170,380,10
hist add gp yvel 170,380,30
hist add gp yvel 170,329,10
hist add gp yvel 170,329,30
hist add gp xacc 170,329,50
hist add gp xacc 170,208,50
hist add gp xacc 170,10,50
hist add gp xacc 170,0,50
hist add gp xacc 170,380,10
hist add gp xacc 170,380,30
hist add gp xacc 170,329,10
hist add gp xacc 170,329,30
hist add zone szz 170,329,10
hist add zone szz 170,208,10
hist add zone szz 170,10,10
hist add zone szz 170,0,10
hist add gp xdisp 170,329,30
hist add gp zdisp 170,329,30
hist add zone pp 170,329,10
hist add zone pp 170,208,10
hist add zone pp 170,10,10
hist add zone pp 170,0,10
hist add fish @hist_eff_stress
hist add fish @effstr1
hist add fish @effstr2
hist add fish @ppress1
hist add fish @ppress2
hist add fish @totstr1
```

```
hist add fish @totstr2
hist add zone vsi 170,329,10
hist add zone vsi 170,208,10
hist add zone vsi 170,10,10
hist add zone vsi 170,0,10
hist add fish @strain1
hist add zone sxz 170,329,10
hist add fish @strain2
hist add zone sxz 170,208,10
hist add fish @strain3
hist add zone sxz 170,10,10
hist add fish @strain4
hist add zone sxz 170,0,10
hist add gp zvel 170,380,50
hist add gp zvel 170,329,50
hist add gp zvel 170,208,50
;
;set dy damp c 0
initial damp hyst default -3.156 1.904
initial damp rayl 0.0005 2.0 stiff
;
solve age 10.0
save dam3
```

File: INT

```
;-----------------------------------------------------------------
;Name: integrate
;Purpose: Integrate a table
;Diagram:
;Arguments: int_in/int/1/table with original data
; int_out/int/2/table with integration
;Note: This routine will integrate a table, outputting another table
;Note: containing the intergration. The resulting table will have the
;Note: same number of points as the original.
;
def integrate(int_in,int_out)
local ii = del_table(int_out)
local outp = get_table(int_out)
local inp = get_table(int_in)
local nitem = table_size(inp)
;
local vold = vtable(inp,1)
local val = 0.0
vtable(outp,1) = vector(xcomp(vold),val)
loop ii (2,nitem)
vnew = vtable(inp,ii)
val = val + 0.5*(ycomp(vold) + ycomp(vnew))*(xcomp(vnew) - xcomp(vold))
```

```
vtable(outp,ii) = vector(xcomp(vnew),val)
vold = vnew
end_loop
;
end
;
```

File: Baseline

```
;-----------------------------------------------------------------
;Name: baseline
;Input: itab_unc/int/102/uncorrected velocity table
;Input: itab_corr/int/120/low frequency sine wave correction
;Input: drift/float/0.3/residual displ. at end of record
;Input: ttime/float/40.0/total time of record
;Input: itab_cvel/int/105/baseline corrected velocity
;Note: Perform baseline correction with low frequency sine wave
def baseline
npnts = table_size(itab_unc)
;
loop ii (1,npnts)
tt = float(ii-1) * ttime / float(npnts)
vv = pi * tt / ttime
cor_d = drift * pi / (2.0*ttime)
ytable(itab_corr,ii) = -(cor_d*sin(vv))
xtable(itab_corr,ii) = tt
ytable(itab_cvel,ii) = ytable(itab_corr,ii) + ytable(itab_unc,ii)
xtable(itab_cvel,ii) = xtable(itab_unc,ii)
endloop
end
```

File: Stage1Plot

```
;-------------------------------------------------------------------------
; Script and Plot for Stage 1
;-------------------------------------------------------------------------
rest dam3
plot create view Load
plot set job off
plot table 1
plot create view PorePress
plot set job off
plot add cont gppp ramp grey reverse on wiretrans 90
plot add axes xaxis color black &
yaxis color black &
zaxis color black scale 11
plot set orientation (77,209,-5) &
center (-14.633, 10.024, 4.9015) &
eye (-153.94,-237.55,71.926) &
```

```
radius 120.9 magnification 1
plot post view PorePress filename "Stage1pp.ps"
plot create view PPhistory
plot set job off
plot add hist 33 linestyle style solid color gray width 2 &
34 linestyle style solid color black width 2 &
35 linestyle style solid color blue width 2 &
36 linestyle style solid color red width 2 &
xaxis label "time (sec)" &
yaxis label "pore pressure (lbf/sqft)"
plot post view PPhistory filename "Stage1pphistory.ps"
plot create view Xvelhistory1
plot set job off
plot add hist 2 linestyle style solid color gray width 2 &
vs 1 &
xaxis label "time (sec)" &
yaxis label "xvelocity (ft/sec)"
plot post view Xvelhistory1 filename "Stage1xvelhistory1.ps"
history dump 2 vs 1 table seis1xvel62215gdm21
table seis1xvel62215gdm21 write seis1gdm21xvel.tab truncate
plot create view Xvelhistory2
plot set job off
plot add hist 3 linestyle style solid color black width 2 &
vs 1 &
xaxis label "time (sec)" &
yaxis label "xvelocity (ft/sec)"
plot post view Xvelhistory2 filename "Stage1xvelhistory2.ps"
history dump 3 vs 1 table seis2xvel62215gdm21
table seis2xvel62215gdm21 write seis2gdm21xvel.tab truncate
plot create view Xvelhistory3
plot set job off
plot add hist 4 linestyle style solid color blue width 2 &
vs 1 &
xaxis label "time (sec)" &
yaxis label "xvelocity (ft/sec)"
plot post view Xvelhistory3 filename "Stage1xvelhistory3.ps"
history dump 4 vs 1 table seis3xvel62215gdm21
table seis3xvel62215gdm21 write seis3gdm21xvel.tab truncate
plot create view Yvelhistory1
plot set job off
plot add hist 11 linestyle style solid color gray width 2 &
vs 1 &
xaxis label "time (sec)" &
yaxis label "yvelocity (ft/sec)"
plot post view Yvelhistory1 filename "Stage1Yvelhistory1.ps"
history dump 11 vs 1 table seis1yvel62215gdm21
table seis1yvel62215gdm21 write seis1gdm21yvel.tab truncate
```

```
plot create view Yvelhistory2
plot set job off
plot add hist 12 linestyle style solid color black width 2 &
vs 1 &
xaxis label "time (sec)" &
yaxis label "yvelocity (ft/sec)"
plot post view Yvelhistory2 filename "Stage1yvelhistory2.ps"
history dump 12 vs 1 table seis2yvel62215gdm21
table seis2yvel62215gdm21 write seis2gdm21yvel.tab truncate
plot create view Yvelhistory3
plot set job off
plot add hist 13 linestyle style solid color blue width 2 &
vs 1 &
xaxis label "time (sec)" &
yaxis label "yvelocity (ft/sec)"
plot post view Yvelhistory3 filename "Stage1yvelhistory3.ps"
history dump 13 vs 1 table seis3yvel62215gdm21
table seis3yvel62215gdm21 write seis3gdm21yvel.tab truncate
plot create view Zvelhistory1
plot set job off
plot add hist 56 linestyle style solid color gray width 2 &
vs 1 &
xaxis label "time (sec)" &
yaxis label "zvelocity (ft/sec)"
plot post view Zvelhistory1 filename "Stage1zvelhistory1.ps"
history dump 56 vs 1 table seis1zvel62215gdm21
table seis1zvel62215gdm21 write seis1gdm21zvel.tab truncate
plot create view Zvelhistory2
plot set job off
plot add hist 57 linestyle style solid color black width 2 &
vs 1 &
xaxis label "time (sec)" &
yaxis label "zvelocity (ft/sec)"
plot post view Zvelhistory2 filename "Stage1zvelhistory2.ps"
history dump 57 vs 1 table seis2zvel62215gdm21
table seis2zvel62215gdm21 write seis2gdm21zvel.tab truncate
plot create view Zvelhistory3
plot set job off
plot add hist 58 linestyle style solid color blue width 2 &
vs 1 &
xaxis label "time (sec)" &
yaxis label "zvelocity (ft/sec)"
plot post view Zvelhistory3 filename "Stage1zvelhistory3.ps"
history dump 58 vs 1 table seis3zvel62215gdm21
table seis3zvel62215gdm21 write seis3gdm21zvel.tab truncate
plot create view ZZstresshistory
plot set job off
```

```
plot add hist 27 linestyle style solid color gray width 2 &
28 linestyle style solid color black width 2 &
29 linestyle style solid color blue width 2 &
30 linestyle style solid color red width 2 &
vs 1 &
xaxis label "time (sec)" &
yaxis label "zzstress (lbf/sqft)"
plot post view ZZstresshistory filename "Stage1zzstresshistory.ps"
plot create view vsihistory
plot set job off
plot add hist 44 linestyle style solid color gray width 2 &
45 linestyle style solid color black width 2 &
46 linestyle style solid color blue width 2 &
47 linestyle style solid color red width 2 &
vs 1 &
xaxis label "time (sec)" &
yaxis label "volumestrain (lbf/sqft)"
plot post view vsihistory filename "Stage1vsihistory.ps"
plot create view xzstresshistory
plot set job off
plot add hist 49 linestyle style solid color gray width 2 &
51 linestyle style solid color black width 2 &
53 linestyle style solid color blue width 2 &
55 linestyle style solid color red width 2 &
vs 1 &
xaxis label "time (sec)" &
yaxis label "xzstress (lbf/sqft)"
plot post view XZstresshistory filename "Stage1xzstresshistory.ps"
plot create view xvelxdisphistory
plot set job off
plot add hist 10 linestyle style solid color red width 2 &
31 linestyle style solid color blue width 2 &
xaxis label "step" &
yaxis label "displacement (ft)"
plot post view xvelxdisphistory filename "Stage1xvelxdisphistory.ps"
```

The following code files for FLAC3D are for a complete, more complex model of the impoundment. The code is the beginning of the larger model and is reduced in size compared to original efforts so that the model will run faster (reduced to 380 feet wide than the actual 1269 feet width that is representative of the Moccasin Hollow Impoundment). The plan was to add the water level and code the piezometric level in the dam before adding the loading from the Stage1 model.

File: GenGrid

```
; Blasting Effects Verification - Stage I
;-------------------------------------------------------------------------------
;Create simplified homogeneous dam
new
config dyn
set dyn off
fix x y z
ini xv 0 yv 0 zv 0 xdisp 0 ydisp 0 zdisp 0
free x y z
gen zone brick group Coarse1 p0(0,0,0) p1(320,0,0) p2(0,380,0) p3(100,0,50)
p4(320,380,0) p5(100,380,50) &
p6(220,0,50) p7(220,380,50) p8(320,0,0) p9(320,380,0) size 64,76,10
model mech elastic range group Coarse1
;prop shea 625000 bulk 1212121.2 range group Coarse1 ; 214% of original moduli
;prop shea 291406.25 bulk 565151.52 range group Coarse1 ; original moduli
prop shea 233125 bulk 452121.21 range group Coarse1 ; 80% of original moduli
;prop shea 349687.5 bulk 678181.82 range group Coarse1 ; 120% of original moduli
;prop shea 407968.75 bulk 791212.12 range group Coarse1 ; 140% of original moduli
;prop shea 466250 bulk 904242.42 range group Coarse1 ; 160% of original moduli
;prop shea 524531.25 bulk 1017272.7 range group Coarse1 ; 180% of original moduli
;prop shea 582812.5 bulk 1130303 range group Coarse1 ; 200% of original moduli
;prop shea 174843.75 bulk 339090.91 range group Coarse1 ; 60% of original moduli
prop pois 0.28 range group Coarse1
; prop tens 2.0882e11 cohes=280 range group Coarse1
;ini dens 3.41 range group Coarse1 ;100% of 3.41
;ini dens 1.364 range group Coarse1 ;40% of 3.41
;ini dens 2.046 range group Coarse1 ;60% of 3.41
;ini dens 2.728 range group Coarse1 ;80% of 3.41
;ini dens 4.092 range group Coarse1 ;120% of 3.41
;ini dens 4.774 range group Coarse1 ;140% of 3.41
;ini dens 5.456 range group Coarse1 ;160% of 3.41
;ini dens 6.138 range group Coarse1 ;180% of 3.41
ini dens 3.751 range group Coarse1 ;110% of 3.41
gen zone brick group Coarse2 p0(120,0,50) p1(440,0,50) p2(120,380,50) p3(220,0,100)
p4(440,380,50 p5(220,380,100) &
p6(340,0,100) p7(340,380,100) p8(440,0,50) p9(440,380,50) size 64,76,10
model mech elastic range group Coarse2
;prop shea 625000 bulk 1212121.2 range group Coarse2 ; 214% of original moduli
```

```
;prop shea 291406.25 bulk 565151.52 range group Coarse2 ; original moduli
prop shea 233125 bulk 452121.21 range group Coarse2 ; 80% of original moduli
;prop shea 349687.5 bulk 678181.82 range group Coarse2 ; 120% of original moduli
;prop shea 407968.75 bulk 791212.12 range group Coarse2 ; 140% of original moduli
;prop shea 466250 bulk 904242.42 range group Coarse2 ; 160% of original moduli
;prop shea 524531.25 bulk 1017272.7 range group Coarse2 ; 180% of original moduli
;prop shea 582812.5 bulk 1130303 range group Coarse2 ; 200% of original moduli
;prop shea 174843.75 bulk 339090.91 range group Coarse2 ; 60% of original moduli
prop pois 0.28 range group Coarse2
; prop tens 2.0882e11 cohes=280 range group Coarse2
;ini dens 3.41 range group Coarse2 ;100% of 3.41
;ini dens 1.364 range group Coarse2 ;40% of 3.41
;ini dens 2.046 range group Coarse2 ;60% of 3.41
;ini dens 2.728 range group Coarse2 ;80% of 3.41
;ini dens 4.092 range group Coarse2 ;120% of 3.41
;ini dens 4.774 range group Coarse2 ;140% of 3.41
;ini dens 5.456 range group Coarse2 ;160% of 3.41
;ini dens 6.138 range group Coarse2 ;180% of 3.41
ini dens 3.751 range group Coarse2 ;110% of 3.41
gen zone brick group Fines1 p0(320,0,0) p1(820,0,0) p2(320,380,0) p3(220,0,50)
p4(820,380,0) p5(220,380,50) &
p6(820,0,50) p7(820,380,50) size 64,76,10
gen zone brick group Fines2 p0(440,0,50) p1(820,0,50) p2(440,380,50) p3(418,0,61)
p4(820,380,50) p5(418,380,61) &
p6(820,0,61) p7(820,380,61) size 64,76,2
attach face
save dam0
plot zone
return
```

File: GravLoad

```
;-------------------------------------------------------------------------
; Blasting Effects Model
;-------------------------------------------------------------------------
;Apply Gravity Loading
restore dam0
range name left y 380
range name right y 0
range name bottom z 0
apply nvel=0.0 range nrange left nrange bottom not
apply nvel=0.0 range nrange right nrange bottom not
fix y z
set grav=0,0,-32.17 small
solve
save dam1
return
```